2019

Precision Measurements of Blazar Spectra with VERITAS

Rita M. Wells
Iowa State University

Precision Measurements of Blazar Spectra with VERITAS

by

Rita Wells

A dissertation submitted to the graduate faculty

in partial fulfillment of the requirements for the degree of

DOCTOR OF PHILOSOPHY

Major: Astrophysics

Program of Study Committee:
Frank Krennrich, Major Professor
Amanda Weinstein
Curt Struck
Kirill Tuchin
Kris De Brabanter

The student author, whose presentation of the scholarship herein was approved by the program of study committee, is solely responsible for the content of this dissertation. The Graduate College will ensure this dissertation is globally accessible and will not permit alterations after a degree is conferred.

Iowa State University

Ames, Iowa

2019

TABLE OF CONTENTS

LIST OF TABLES

LIST OF FIGURES

ABSTRACT

Imaging-Atmospheric Cherenkov Telescopes (IACTs) provide insights into a number of open questions in high energy physics, astroparticle physics, and cosmology. However, due to the indirect detection methods necessary to observe TeV gamma rays, the systematic and statistical errors produce a broad energy resolution of about 15–20% during analysis. Therefore, investigating and characterizing systematics of IACTs is necessary for producing accurate measurements. This thesis presents an analysis technique developed to characterize VERITAS systematics at TeV energies on blazar spectra arising from saturation of the electronics. The application of this analysis method to two epochs of data from the Crab Nebula, extending above 20 TeV, determined minimal systematic effects from saturation. Instead, the analysis showed bias arising primarily from the choice of low gain ratio, which lead to further investigation of the correct value to apply for the low gain ratio during analysis. With correct values of the low gain ratio applied, the systematic bias from saturation of the electronics is less than statistical errors out to energies greater than 20 TeV. Finally, analysis of five blazar spectra extending to multi-TeV energies is presented, with both the nominal low gain ratios and the low gain ratios as determined in this thesis. The updated low gain ratio values demonstrate improved energy reconstruction in a VERITAS analysis, leading to more precise spectral reconstruction with low systematic bias from saturation of the electronics.

CHAPTER 1. INTRODUCTION TO GAMMA-RAY ASTRONOMY

1.1 A Brief History of Gamma-Ray Astronomy

The history of high-energy particle astrophysics begins in the early twentieth century, with the discovery of high energy particles striking the atmosphere from all directions and originating outside of earth. In 1912, Victor Hess used balloon-born experiments to study radiation originating from the earth as a function of distance from the surface. He was shocked to discover that, as the altitude of his balloon increased, the flux of radiation also increased [33]! Cosmic rays, as Hess discovered, arrive at earth from all directions and reach energies of up to 10^{20} eV, or twenty orders of magnitude higher in energy than the light visible to the human eye. By studying the processes that produce these cosmic rays, we can probe fundamental questions in physics. Frustratingly to Hess and those who sought to study cosmic rays in the years after, magnetic fields through the galaxy and the wider universe scatter the directions of these particles by the time they reach earth's neighborhood, leading to the isotropic distribution of particles seen at earth. The paths of photons are not distorted by magnetic fields as they are neutral particles. Therefore, gamma rays can be used to trace the origins of cosmic rays.

Gamma-ray astronomy provides an exciting probe into a number of scientific questions, however, reaching beyond the origin of cosmic rays. At the energies focused on in this thesis, known as the very-high-energy (VHE) range, the sources of these gamma-rays reach and exceed the energies of even the best colliders on earth. The processes that produce such high energy radiation are of great interest to fundamental physics. Gamma rays allow us

to probe fundamental questions about the basic physical laws of the universe, and provide insights into our cosmological history.

In 1948, Blackett was the first to suggest that as much as 0.01% of the night sky background could originate from Cherenkov light from highly charged particles in the atmosphere [8]. These charged particles, according to Blackett, were produced by the interaction of cosmic rays in the atmosphere. Jelley and Galbraith tested this idea in 1953 with a photomultiplier tube (PMT), a 10-inch parabolic mirror, and an oscilloscope [25]. They detected pulses of light that they then correlated with showers observed in a nearby air-shower detector, thus demonstrating that air showers could be detected by the Cherenkov light they produced. In 1963, Jelley and Porter suggested the Cherenkov light from these air showers could have applications in gamma ray astronomy [41], as a method of indirect detection of astrophysical gamma ray sources.

1.1.1 Cosmic Rays

Approximately 90% of Cherenkov light produced in the atmosphere originates from cosmic rays. Cosmic rays are today known to be primarily charged nuclei, such as protons and heavier ions, which are accelerated up to energies of 10^{20} eV. The particles are most likely produced in environments such as supernova remnants, pulsar wind nebulae, and GRBs.

Figure 1.1 shows the cosmic ray spectrum for particles extending from 10^8 to 10^{20} eV (based on the cosmic ray spectrum produced in [11]).

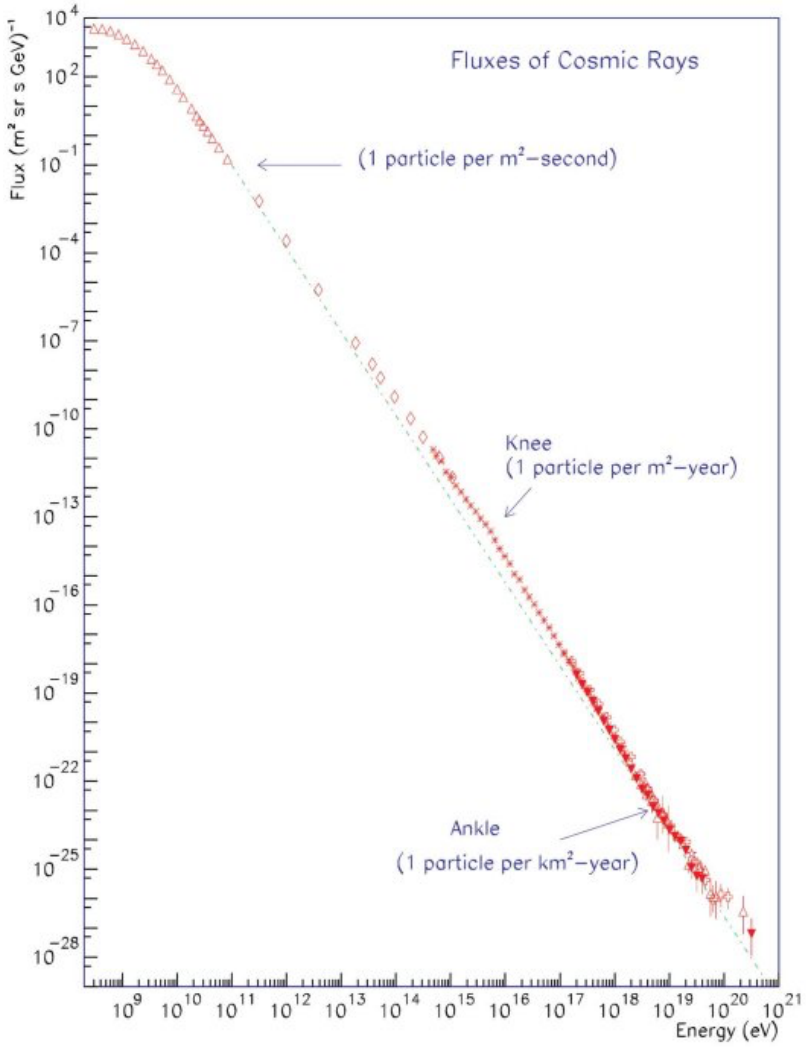

Figure 1.1 The spectrum of cosmic rays measured from Earth. Figure based on the cosmic ray spectrum produced in [11].

Several features of particular interest arise out of the cosmic ray spectrum across the entire measured energy range. A "knee" occurs at energies around 10^{15} eV, where the spectrum turns over slightly. At energies of about 10^{18} eV, an ankle occurs and the spectrum hardens. Beyond 10^{20} eV, the GZK cutoff stops production of higher energy cosmic rays.

Cosmic rays of energies up to about 10^{18} eV can be contained within the Milky Way by galactic magnetic fields. These cosmic rays may thus originate from galactic sources. Cal-

culating equipartition strength from synchrotron emission provides a Milky Way magnetic field of about 6-10 μG, or approximately 1 nT [5]. Cosmic rays of energies up to about 10^{18} eV can be contained within the Milky Way by galactic magnetic fields. These cosmic rays may thus originate from galactic sources. The highest energy cosmic rays likely originate outside the Milky Way. The gyro-radius for a proton of energy 10^{20} eV is large enough to escape the magnetic fields of a typical spiral galaxy.

Cosmic rays are of interest to VERITAS for two primary reasons. As they travel between their source and earth, the paths of cosmic rays are scrambled by galactic magnetic fields. Gamma rays, as neutral particles, are not affected by magnetic fields as they travel from the source to our detectors on earth. Therefore, gamma rays make excellent tracers of the sources of cosmic rays. Due to the high flux of cosmic rays relative to gamma rays, however, cosmic-ray induced air-showers are also the primary source of background for ground-based gamma ray observations. The analyses presented in this thesis are primarily concerned with rejecting cosmic ray background events, rather than determining astrophysical sources of cosmic rays.

1.1.2 Gamma Rays

Gamma rays cover the energy range above approximately 100 keV. Gamma rays are difficult to measure directly, due to their extreme energies. They interact easily with materials, and therefore are best measured through scintillators and calorimeters to track the showers resulting from gamma rays interacting with material. Below approximately 10^2 GeV, gamma rays can be detected by space-based telescopes such as the Fermi Gamma-ray Space Telescope.

Above about 10^2 GeV, two effects limit the usefulness of space-based gamma-ray telescopes. First, the size of the showers in the detector grow too large to be mostly contained in a space-based telescope. Second, the flux of astrophysical gamma rays declines exponentially with energy. The flux of gamma rays from the Crab Nebula, one of the brightest

known VHE sources, at 1 TeV is only about 7 photons per square meter per year [55, 36]. This makes VHE gamma rays difficult to measure with a space-based telescope such as Fermi, which has a collection area on the order of 1 m^3.

Therefore, a different technique was developed for the imaging of showers resulting from gamma rays with energies approaching or exceeding TeV energies. Gamma rays of TeV order energy which strike the atmosphere produce secondary particles which emit Cherenkov radiation. The pool of Cherenkov light at sea level resulting from such air showers can be up to several hundred meters in diameter. The Cherenkov light peaks in the blue to UV and can be imaged by a telescope with a fast and sensitive camera (see Chapter 2 for more details). The technique used to image this Cherenkov light, known as the Imaging Atmospheric-Cherenkov Technique (IACT) was pioneered by Trevor Weekes and the Whipple Collaboration, along with the field of VHE gamma-ray astronomy [55]. Trever Weekes drove the formation of the Whipple 10-m telescope in southern Arizona, which served as the proof of concept for the IACT telescope arrays that followed in the years after its conception and the formal creation of the Whipple Collaboration in 1982.

The first astrophysical TeV gamma rays were discovered by Whipple in 1989, through observations of the Crab pulsar wind nebula (PWN) [55]. Due to the brightness and stability of gamma rays from the Crab PWN at VHE energies, this source has since become the standard candle against which many other sources of gamma-ray emission are compared. Source fluxes are commonly given in Crab Units, which describes the integrated flux above 200 GeV for a source with a similar spectral shape as the Crab at VHE energies [2].

From the first detection of the Crab Nebula, VHE gamma-ray astronomy exploded as a field. As of the writing of this thesis, there are over 200 known VHE sources. These sources spread include a wide range of astrophysical objects both within and outside of the Milky Way. These sources can be broadly classified as either galactic or extragalactic sources. A brief overview of the different sources that make up VHE emitters in the universe is given in the following sections.

1.2 Galactic Sources

Galactic sources, such as the Crab Nebula, include such VHE emitters as pulsar wind nebulae, pulsars, supernova remnants, and VHE binaries also known as microquasars. The primary galactic source of interest to this thesis is the Crab Nebula. It is discussed further in Chapter 4.

1.3 Extra-galactic Sources

The bulk of TeV emitting extragalactic sources are comprised of blazars.

1.3.1 Active Galactic Nuclei

All galaxies are believed to contain a supermassive black hole at the center. An active galactic nucleus (AGN) occurs when this supermassive black hole at the center of a galaxy is accreting matter, often seen in spiral disk galaxies. As stars, gas, and dust approach the center of the galaxy, the intense gravitational field of the supermassive black hole causes the material to orbit so fast that even the stars are torn apart, and a bright disk known as an accretion disk forms around the edges of black hole outside of the Schwarzschild radius. The accretion disk loses a great deal of heat and energy to friction as the material within it runs together, and this energy loss causes material to fall into the black hole. However, if there is enough material with enough energy, the material accreting around the edges of the black hole creates jets of extremely high-energy emission that can extend many parsecs out into space. These jets extend perpendicular to the plane of the galaxy, and characterize all AGN.

1.3.1.1 Anatomy and Classification

- **Quasars:** A quasar is a class of AGN in which the jet is directed at an angle less than 90° but greater than 0° to the observer. This orientation allows the observer to view emission lines from the material creating the jets.

- **Blazars:** A blazar is a class of AGN which is oriented such that the jet emission from the region around the supermassive black hole at the center of a galaxy is directed towards Earth. Observatories on earth therefore get the full effect of the Doppler beamed radiation, which makes blazars some of the brightest sources in the universe. Theoretical models explain how blazars can produce gamma rays of energies up to tens of TeV. Observations at these energies are difficult, but some show evidence for blazar emission at such high energies. Two sub-categories of blazars exist: BL Lacs, and flat spectrum radio quasars (FSRQs). FSRQs have strong emission lines. BL Lacs show weak or no emission lines, which makes their redshift difficult to measure.
- **Radio Galaxies:** Radio galaxies make up the remainder of extragalactic VHE sources. While common, there are only a small number of radio galaxies currently detected at VHE energies. They are strongly misaligned from Earth, and thus show little Doppler beaming. Therefore, they are very weak gamma-ray sources.

1.3.1.2 Blazars

The emission spectrum of a blazar consists of two separate νF_ν peaks, one at radio, UV, or x-ray wavelengths, and a second peak at a higher frequency in the x-ray or gamma-ray regime. These peaks can be seen in Figure 1.2, taken from [1]. The first peak is well known to arise from synchrotron radiation from ultra-relativistic electrons originating near the supermassive black hole [18]. The accretion disk around the black hole produces high magnetic fields. Electrons stripped from their parent particles are accelerated in these magnetic fields, and produce synchrotron radiation as they lose energy.

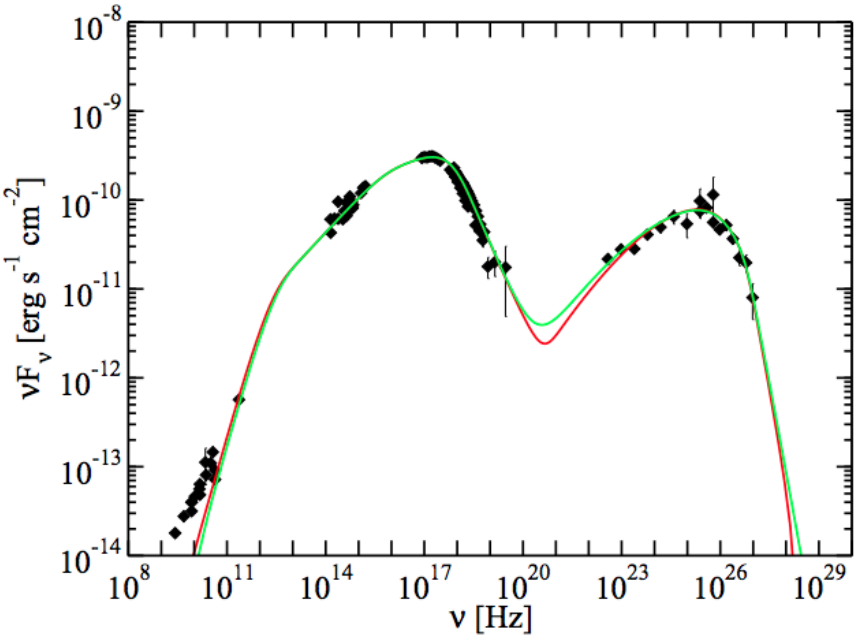

Figure 1.2 The spectral energy distribution (SED) for blazar Mrk 421, with the lower energy synchrotron peak shown in x-ray energies, and the SSC peak in gamma-ray energies. Figure taken from [1].

Current models predict that the HE and VHE gamma-ray emission, forming the second peak in νF_ν, comes primarily from a process known as synchrotron-self-Compton (SSC) emission. The same population of electrons that produces the synchrotron radiation upscatters soft photons via the inverse Compton process, which can lead to the production of photons reaching hundreds of GeV to TeV energies [9]. The self-Compton part of the SSC model refers to the fact that the soft photons are drawn from the same synchrotron radiation field produced by the electrons responsible for upscattering the electrons as well. Some models include soft photons drawn from ambient fields near the jet but not associated with the source itself. This is referred to as the external-Compton (EC) mechanism.

To a simple approximation, many blazar spectra can be described as a power law within a limited energy range at VHE energies, with energy dependent index, Γ, given in Equation 1.1.

$$\frac{\mathrm{d}N}{\mathrm{d}E} = N_0 \left(\frac{E}{E_0} \right)^{-\Gamma} \tag{1.1}$$

where E_0 is a normalization energy, typically chosen as 1 TeV, and the flux $\frac{\mathrm{d}N}{\mathrm{d}E}$ is given in terms of TeV^{-1} m^{-2} s^{-1}. For a blazar spectrum in the hundreds of GeV to TeV energy range, the negative sign on the index, Γ, references the fact that the flux decreases with energy.

Gamma-ray spectra are often characterized in terms of "softness" or "hardness" based upon the spectral index. The more negative the index, the softer the spectrum. Conversely, a spectrum "hardens" as the index approaches zero.

1.4 Blazars as a Probe of the Extragalactic Background Light

The extragalactic background light (EBL) is diffuse cosmological radiation consisting of all light emitted since the epoch of recombination. Major sources of EBL photons include galaxies, stars, and supernovae. As such, it provides a method of tracking star and galaxy formation throughout the history of our universe, making it a fundamental cosmological quantity [18]. There are two primary peaks in the EBL spectral energy distribution (SED). At shorter wavelengths, stretching from the optical to near UV, is unprocessed starlight. The hump at longer wavelengths is from primarily starlight that has been reprocessed down into the IR by dust.The biggest contributor is supernovae, which means that understanding the shape of the EBL can provide insights into supernova rates. There are also features that come from PAHs.

1.4.1 Theoretical Models and EBL Density

The total integrated EBL intensity is a measure of the bolometric luminosity of the universe [17]. Accurate models must account for: NIR emission from galaxies, MIR and FIR emission from dust in galaxies, and redistribution of energy from cosmic expansion.

There are four main methods of constructing theoretical models of the EBL [16]. Forward evolution begins with initial cosmological models of the early universe and evolves them forward in time, using semi-analytical models of galaxy formation. Backwards evolution extrapolates current star and galaxy populations backwards in time. Both of these models are heavily dependent on theoretical cosmology. Two other methods involve more observational quantities, such as the third method of evolving galaxy counts across a range of redshifts via observable quantities such as star formation rates in the universe. The final method is "galaxy counting", determining evolution of galaxy populations via direct observations across a range of redshifts.

Both forward and backward evolution models are heavily dependent on the values of cosmological constants chosen for the model. Therefore, they are subject to the same uncertainties as the chosen models. Direct galaxy observations provide absolute lower limits to the density of the EBL. The true intensity of the EBL could be higher than galaxy counting estimates, both because galaxies provide only one source of contribution to the EBL, and because only galaxies bright enough to observe can be counted, though even dimmer galaxies will contribute some amount to total EBL intensity. Galaxy counting also fails to take into account any diffuse EBL background. Figure C.1 shows several models derived from theoretical cosmological principles and from direct measurements of galaxy luminosity.

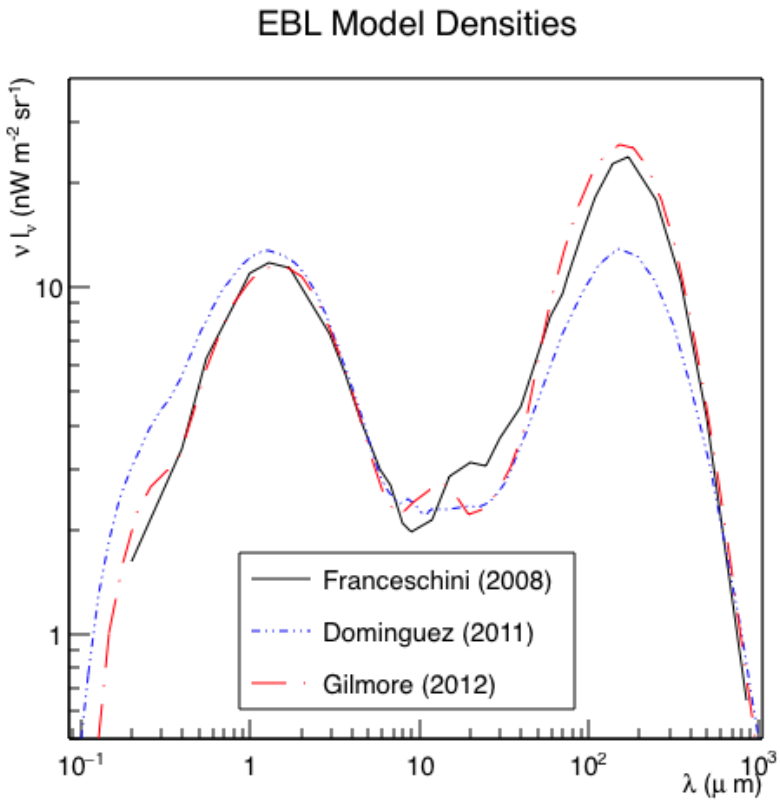

Figure 1.3 EBL SEDs for three theoretical models, [16], [22], and [27].

Further details are provided in Appendix C. Direct measurement of the EBL density from earth is made extremely difficult to high zodiacal foreground emission. Therefore, indirect measurements and theoretical models are important to accurately reconstructing cosmological history.

1.4.2 Blazars as a probe of the EBL

While galaxy counting places lower limits on the EBL, and various theoretical models can produce expected values of EBL density at a given wavelength and redshift, it is helpful to have further methods of measuring true values. Blazars are extremely useful for providing upper limits. The gamma rays emitted by distant blazars can be used as indirect probes of EBL density due to the extinction that occurs between EBL photons and gamma ray

photons above the threshold energy for pair production. A gamma ray above approximately 50 GeV meeting a soft EBL photon in the ISM can pair-produce. The resulting electron-positron pair are deflected by faint magnetic fields, thus ensuring that both photons are lost to observation. This process is shown below in Figure 1.4, with the angle between the interacting photons described by the angle θ.

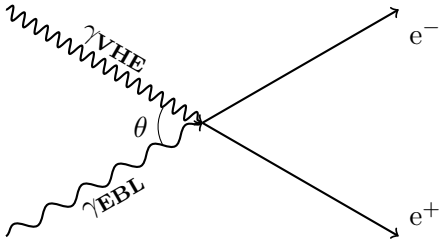

Figure 1.4 A high energy gamma ray encountering a soft EBL photon, leading to the production of an electron-positron pair. The angle between the interacting photons is given by θ.

This threshold energy is given by Equation 1.2, derived from conservation of 4-momentum for the interacting photons. Here, θ is redefined in terms of μ, where $\mu = \cos(\theta)$.

$$\epsilon_{\text{th}}(\epsilon_\gamma, \mu) = \frac{2m_e^2}{\epsilon_\gamma(1 - \cos(\theta))} \tag{1.2}$$

For a gamma ray spectrum extending to energies greater than ϵ_{th}, the flux is thus attenuated by an amount proportional to the EBL density in the IR range. In order to determine the attenuated flux from a blazar, two properties must be known: the redshift of the blazar and corresponding distance between the blazar and earth, and the intrinsic spectrum at the source. If these quantities were known exactly, then the density of the EBL between the source and the observer on earth could be directly measured. Unfortunately, the intrinsic spectrum of a single blazar cannot be determined to complete accuracy. However, theoretical limits exist for the hardness of blazar spectra when measured as a power law. A blazar with a power law index harder than 1.5 is non-physical according to [18].

If this limit in spectral hardness holds true, blazar attenuation can be used to place upper limits on EBL density. A blazar spectrum as measured on earth (the "observed spectrum") can be de-absorbed to regain the intrinsic spectrum. If the EBL density is assumed to be too high, the de-absorbed spectrum will achieve non-physical hardness. Therefore, by de-absorbing a large range of blazar spectra at a range of redshifts, the limit in which any spectrum becomes non-physical places the upper limit of the EBL intensity. Because the distribution of stars and galaxies throughout the universe is, on average, extremely uniform, the EBL can be assumed to be a mostly diffuse field with minimal fluctuations at different points in space. Therefore, the collection of blazar sources need not be perfectly uniform in either RA and Dec space or redshift in order to generalize the upper limit results.

More discussion of the methods of using blazars as an indirect probe of EBL intensity is given in Chapter 7 and Appendix C.

CHAPTER 2. GROUND-BASED GAMMA-RAY ASTRONOMY

This chapter provides a description of VERITAS (Very Energetic Radiation Imaging Telescope Array System) and the data taking process with a ground-based array. The chapter begins with a detailed overview of the physics and anatomy of air showers and their Cherenkov light emission, including the difference between gamma-ray initiated showers and our primary source of background, cosmic rays. Then a brief overview of the ground based detector technique is given. The chapter concludes with a detailed discussion of the hardware of VERITAS and the process for taking science data.

2.1 Air-Showers

VERITAS is sensitive to a primary gamma-ray energy of about 85 GeV to 30 TeV. Primary gamma rays in this energy range have enough energy to produce Cherenkov radiation. This section describes Cherenkov radiation and air-shower physics, focusing on electromagnetic cascades caused by the gamma rays in the energy range of interest to VERITAS. This is followed by a brief overview of the differences between gamma-ray showers and cosmic ray showers, which make up the majority of the background for VERITAS.

2.1.1 The Cherenkov Light Spectrum

Cherenkov radiation is the term given to light produced by a charged particle moving faster than the speed of light through a medium. This process was first discovered by P.A. Čerenkov in 1934, through light emitted by electrons moving through liquid medium [40]. In 1937, the process was explained by Frank and Tamm [23]. A charged parti-

cle passing through the atmosphere excites nearby atoms. These atoms then emit radiation when returning to the ground state. If the charged particle moves through the medium faster than the emitted light, the resulting radiation interferes constructively and produces flashes of radiation that can be detected by a ground-based array.

This radiation is emitted in a cone around the charged particle, as seen in Figure 2.1.

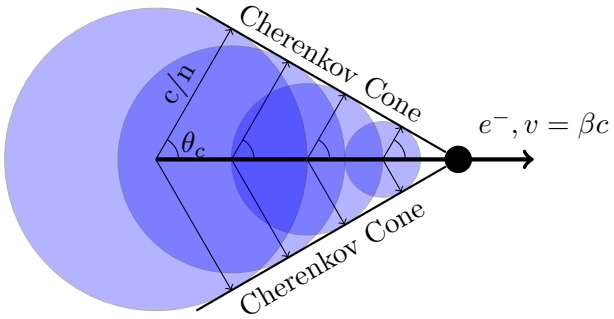

Figure 2.1 A geometric construction of a particle traveling at velocity $v > \frac{c}{n}$ and its resulting Cherenkov emission.

The half-angle of this cone is referred to as the *Cherenkov angle*. An electron or positron moving at velocity $v = \beta c$ produces a Cherenkov angle given by Equation 2.1.

$$\cos(\theta_c) = \frac{c}{vn} \tag{2.1}$$

The maximum angle occurs in the limit where v approaches the speed of light c. The maximum angle is shown in Equation 2.2.

$$\theta_{\max} = \cos^{-1}\left(\frac{1}{n}\right) \tag{2.2}$$

The minimum threshold energy for Cherenkov emission can be simply derived from basic physics principles. A charged particle must be traveling at a minimum velocity of $v = c/n$, or the speed of light divided by the refractive index of the chosen medium. The relativistic gamma-factor for such a particle is given by Equation 2.3

$$\gamma = \frac{1}{\sqrt{1 - 1/n^2}} \tag{2.3}$$

The total energy of the particle therefore is given by $E = \gamma mc^2$, where m is the particle's rest mass. The minimum energy is given in Equation 2.4.

$$E_{\min} = \frac{mc^2}{\sqrt{1 - 1/n^2}} \tag{2.4}$$

Because the density of the atmosphere changes with altitude, the refractive index varies as a function of depth into the atmosphere. Therefore the threshold energy for Cherenkov radiation also varies with atmospheric depth. The refractive index, n, depends on column depth, X, typically measured in g/cm^2. The scaling is shown in Equation 2.5.

$$n = 1 + n_0(X/X_0) \tag{2.5}$$

As the shower progresses through the atmosphere, the energy losses due to the Cherenkov emission were derived by Frank and Tamm in 1937 [23], and are shown here as the differential relation in Equation 2.6.

$$\mathrm{d}E = \frac{q^2}{c^2}\left(1 - \frac{1}{\beta^2 n \omega^2}\right)\omega \mathrm{d}\omega \mathrm{d}l \tag{2.6}$$

where q refers to the charge of the particle, β is the velocity of the particle given as v/c, and ω refers to the frequency of the emitted radiation. The distance traveled through the atmosphere is given by $\mathrm{d}l$. It is convenient, in the case of Cherenkov radiation, to discuss the energy loss in terms of wavelength rather than frequency. The conversion to wavelength is given simply by $\omega = 2\pi c/\lambda$. Therefore, Equation 2.6 can be written as a function of λ, as seen in Equation 2.7.

$$\mathrm{d}E = -q^2\left(1 - \frac{\lambda^2}{4\pi^2\beta^2 n c^2}\right)\frac{4\pi^2}{\lambda^3}\mathrm{d}\lambda \mathrm{d}l \tag{2.7}$$

It is useful here to discuss column depth, for which the conversion is given as $\mathrm{d}X = \rho \mathrm{d}l$, where ρ is the density of the atmosphere at a given depth. Using the method shown by Greider [30] to convert energy density in Equation 2.7 into differential photon density as a function of wavelength and atmospheric density, leads to Equation 2.8.

$$\mathrm{d}N_{ph} = \frac{2\pi\alpha}{\lambda^2 \rho}\left(1 - \frac{1}{\beta^2 n(\lambda)^2}\right)\mathrm{d}X \mathrm{d}\lambda \tag{2.8}$$

where α is the fine structure constant. Equation 2.8 then implies that the differential photon density depends on the inverse square of the wavelength. This explains why air-showers generated by electromagnetic cascades in earth's atmosphere peak in the wavelength range of blue light. Additionally, Jelley and Galbraith showed in 1953 that the density of Cherenkov light per unit frequency per unit length is a constant [25]. Therefore, the Earth's atmosphere is an effective calorimeter for the showers of interest to VERITAS.

2.1.2 Gamma-ray Showers

Photons of sufficiently high energy impacting with the atmosphere interact with the Coulomb fields of nuclei in the atmosphere to produce an electron/positron pair, in a process known as Coulomb pair production. The dominant method of energy loss for the electron/positron pair occurs through further interactions with atmospheric nuclei via the emission of bremsstrahlung photons. Bremsstrahlung refers to the process in which a charged particle is deflected by an outside Coulomb field and decelerates by emitting a photon. The radiation length for bremsstrahlung in air is given by $X_0 = 37.15$ g/cm^3 [24]. Bremsstrahlung produced from sufficiently energetic $e^{\pm}$ pairs will themselves further pair produce, thus building up the number of Cherenkov light emitting particles in the shower.

The process repeats until the electrons drop below the critical energy, E_c, of 84 MeV [24], resulting in an electromagnetic cascade like the example shown in Figure 2.2. The superluminal electrons and positrons in these cascades also cause the emission of the Cherenkov light detected by Imaging Atmospheric Cherenkov Detectors (IACTs) such as VERITAS.

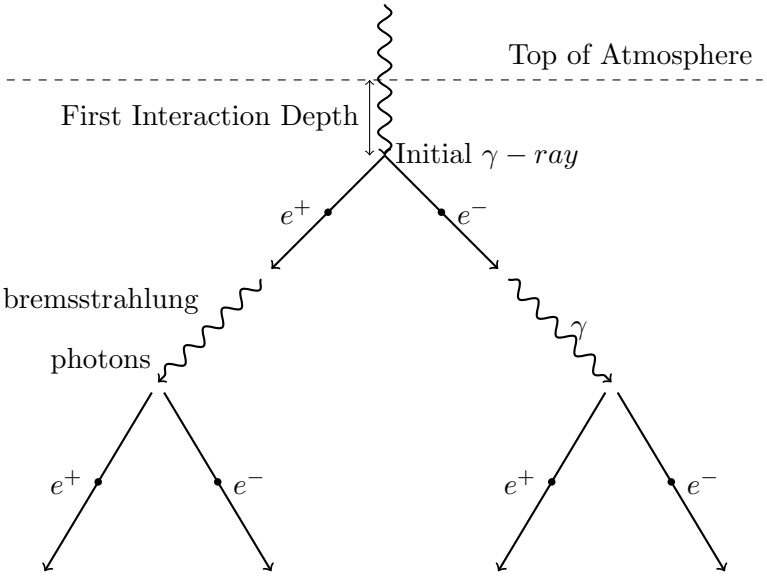

Figure 2.2 A simple diagram of an electromagnetic cascade. The radiation length is equivalent for bremsstrahlung losses and pair production from bremsstrahlung photons. Successive $e^{\pm}$ pairs produce their own Cherenkov cones until they drop below the required energy for producing Cherenkov radiation.

Applying Equation 2.8 to the electron/positron pairs produced in a gamma-ray shower gives an estimate of the photon density and energy of a gamma-ray initiated air-shower. Each electron or positron above the Cherenkov energy threshold in air at sea level produces roughly 30 photons between 350 and 500 nm for every meter traveled. Additionally, particles with a greater initial energy travel a greater distance before dropping below the energy threshold for Cherenkov radiation.

2.1.2.1 Number of Particles in a Gamma-ray Air-Shower

Greisen [31] provides the approximate total number of electrons, $N(t)$, in a shower produced by an incident photon with energy E_0, at a *shower age* s and depth in radiation lengths t:

$$N(t) \approx \frac{0.31}{\beta_0^{1/2}} e^{t(1-1.5\ln(s))} \tag{2.9}$$

where $\beta_0 = \ln(E_0/E_c)$. The age parameter, s, relates to the number of radiation lengths, t, by

$$s = 3t/(t + 2\beta_0) \tag{2.10}$$

The age parameter, s, is a measure of how "old" the shower is in terms of number of particles produced, and describes three major regions related to particle production. For $s < 1$, the shower is still producing particles that have not yet dropped below the threshold for bremsstrahlung. The particles produced at $s = 1$ have dropped below the critical energy for bremsstrahlung, and thus will no longer continue generating more particles in the air shower. At $s > 1$, the amount of light reaching a detector at a given height begins to decrease, as the wave front expands without producing any more photon-generating particles. The depth at which the maximum number of particles occur is known as the *shower maximum*. This depth follows a roughly logarithmic distribution in E_0. An approximate number of Cherenkov photons arriving at a detector can thus be determined integrating Equation 2.9 up to the shower maximum. The calculation of shower maximum is shown in greater depth in the following section.

The energy of the initial gamma ray is directly related to the flux of photons produced during the air shower. Therefore, the total photon flux can be used by a detector on the ground to estimate the initial gamma-ray energy.

2.1.2.2 Shower Height

The shower maximum is given by the depth at which the maximum number of particles has been produced. At this point, the electrons and positrons are below the energy threshold for producing further particles. The maximum can be obtained by maximizing Equation 2.9 with respect to t, as in Equation 2.11.

$$\frac{\mathrm{d}N}{\mathrm{d}t} = \frac{1}{2}(s - 1 - 3\log(s))N(t) \tag{2.11}$$

This function is maximized at $s = 1$. Plugging this into Equation 2.10 and solving for t gives an energy-dependent shower maximum of

$$t_{\max} = \ln\left(\frac{E_0}{E_c}\right) \tag{2.12}$$

The radiation length for bremsstrahlung is given in Section 2.1.2, and depth is given by $X = tX_0$. A simple isothermal model of the atmosphere provides a conversion between depth to sea level and height above sea level of $X = X_{\rm sl}e^{-h/h_0}$, where $X_{\rm sl} \approx 1030$ g/cm^2 and $h_0 \approx 8.4$ km at sea level.

A more accurate estimate of the relation between vertical depth and scale height is discussed in detail in Chapter 6, with further discussion shower maximum as a function of energy for air showers detected by VERITAS.

2.1.2.3 The Cherenkov Light Pool

The lateral distribution of particles in an electromagnetic air-shower depends upon both the Cherenkov angle and multiple Coulomb scattering from the bremsstrahlung interactions. The maximum Cherenkov angle for electrons in air can be found from Equation 2.2. The refractive index of the atmosphere depends on depth. However, for the majority of the photons which are emitted at altitudes of a few to tens of km, the Cherenkov angle is small, $< 1°$.

The radial spread, r, due to Coulomb scattering is characterized by the Moliere unit, r_1, which gives the spread of low energy particles in a shower as

$$r_1 = \frac{E_s}{E_c}X_0 \tag{2.13}$$

where $E_s \approx 21$ MeV.

Following the method of Greisen [31], an approximate solution to the lateral density of Cherenkov electrons, $\rho(N, r)$, at radius r for a shower with Moliere radius r_1 is given by Equation 2.14:

$$\rho(N, r) = \frac{0.4N(t)}{r_1^2}\left(\frac{r_1}{r + r_1}\right)^{3.25}\left(1 + \frac{r}{11.4r_1}\right) \tag{2.14}$$

Equation 2.14 is a modified case of the Nishimura-Kamata-Greisen (NKG) functions, which includes an extra term to account for the fact that at large distances from the shower axis, the particle density drops as $\frac{1}{r^3}$ [31].

Equation 2.14 produces a fairly smooth curve, with electron density dropping shallowly out to about 130 m from the shower axis, and then dropping more steeply beyond that, in the region dominated by multiple scattering. To a simple approximation, Cherenkov photon density is expected to follow a similar distribution. However, Monte Carlo simulations can be used to produce a more realistic distribution of photon density. Three distinct regions arise in the photon density distribution produced by simulations:

1. A core region where the bulk of the Cherenkov photons arrive. These photons have a small scattering angle to the shower axis.
2. A peak around 130 m where there is a focusing effect from the dependency of n_{atm} on depth into the atmosphere. The maximum Cherenkov angle increases as a function of atmospheric depth. Therefore, photons emitted deeper into the atmosphere have a wider Cherenkov angle, leading to a peak in the photon density at approximately 130 m from the shower core for showers arriving from zenith.
3. A tail out to a few hundred meters from the multiple Coulomb scattering.

This indicates that the Cherenkov angle produces a noticeable effect on top of Coulomb scattering in the lateral profile of an air-shower. Hillas describes the peak around 130 m as the Cherenkov ring [34], a ring of increased photon density arising from the phase coherence between radiation along a particle track. Considering the Cherenkov angle from Equation 2.2, as the particles travel deeper into the atmosphere, n increases, which leads to a corresponding increase in θ. For a shower that started at 20 km above sea level and continuing to an altitude of a few km, a Cherenkov light rim (ring) occurs at about 100 to 150 m from the shower core. The width of this Cherenkov light ring on the ground increases for showers arriving at an angle away from zenith, and is blurred by Coulomb scattering. Photons arriving in the radial region of the ring originate from the whole longitudinal devel-

opment of the shower. Therefore, those photons are useful to calculate shower maximum. See Chapter 6 for further discussion.

2.1.2.4 Time Dispersion

Photons arriving at the ground from an air shower also have a time dispersion profile. The timing profile contains important information for detection and reconstruction of the shower. Hillas describes the time distribution of photons arriving from air showers [34].

In a simple model ignoring Coulomb scattering and refraction, photons emitted at different points along the shower axis will arrive at a detector on the ground with timing relative to their emission height. Figure 2.3 shows a simple model of a particle traveling at velocity v_e, emitting photons at successive points along the trajectory that are then captured by a detector at distance r from the shower axis, based on [34, Figure 1] from Hillas. The first interaction occurs at height h_i. Electrons and positrons then emit successive photons at heights h along the shower axis, with Cherenkov angle θ_c and velocity $\frac{c}{n}$, until the emitting particles drop below the threshold energy for Cherenkov light production at height h_f. The Cherenkov photons are collected by a detector D on the ground at distance r from the shower core.

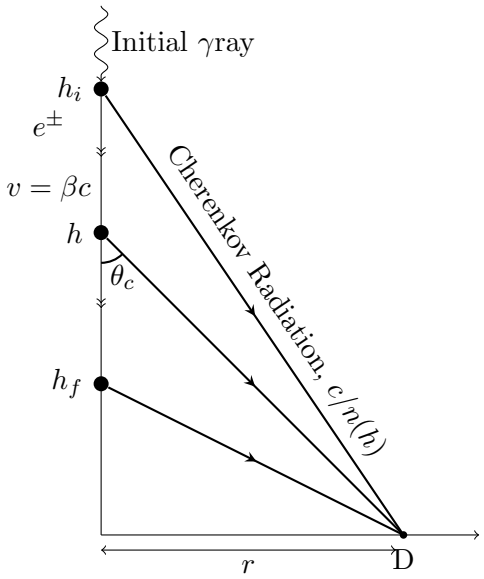

Figure 2.3 A simple geometric model of light production in a gamma-ray induced shower. Cherenkov angle, θ_c, varies between about 0.3° at 12 km and 1.2° at sea level (Figure not to scale).

Of interest to the hardware of a ground-based detector is the time required to capture the full Cherenkov shower. For the simple model of a shower arriving from zenith including refraction, the velocity of light is slowed by the atmosphere, to $v_\gamma = \frac{c}{n}$. The geometric construction for a photon with parameters as follows: emitted at height h, arriving at a detector at distance r from the shower axis, with Cherenkov angle θ_c and velocity $v = \frac{c}{n}$, emitted by a particle traveling in the limit $v_e \to c$ that emitted its first photon at height h_i; the arrival time relative to the first photon is given by Equation 2.15.

$$\Delta t = -\left(\left(\frac{h \cdot n(h)}{c \cdot \cos(\theta)} + \frac{h_i - h}{c}\right) - \frac{h_i \cdot n(h)}{c \cos(\theta_i)}\right) \tag{2.15}$$

For the detector at distance r from the shower axis, $\cos(\theta) = \frac{h}{\sqrt{h^2+r^2}}$. The overall negative sign occurs because, due to the emitting electron moving faster than the Cherenkov light, photons emitted **earlier** in the shower will reach the ground at a **later** time than photons emitted further along the particle's trajectory.

For photons of about 400 nm (the approximate peak of the Cherenkov spectrum described in Section 2.1.1) the dependency of n on slant depth, ignoring temperature dependence, is given by Hillas, reproduced here in Equation 2.16:

$$n = 1.0 + 0.000296(X/X_{\mathrm{sl}}) \tag{2.16}$$

Applying the toy model of slant depth to height in km from Section 2.1.2.2, this gives n in terms of height in km.

$$n = 1.0 + 0.000296e^{-h/8.4} \tag{2.17}$$

As a simple example, consider an air-shower with an initial energy of a few hundred GeV, with a fairly typical first interaction height of 20 km and continuing until a height of 1.3 km above sea level, corresponding approximately to the altitude of VERITAS. By plugging Equation 2.17 into Equation 2.15 and integrating photon arrival times from $h_i = 1.3$ km to $h_f = 20$ km for a detector directly in line with the shower axis, thus setting $\cos(\theta) = 0$, the time between detection of the first and last photons is shown in Equation 2.18.

$$\Delta t = \frac{1}{c}\int_{1.3}^{20} 0.000296e^{-h/8.4}\mathrm{d}h = 6.33 \text{ ns} \tag{2.18}$$

For a detector at a distance $r > 0$ m, the value of Δt must be numerically evaluated, as the integral no longer has a closed form solution. Nevertheless, Equation 2.18 provides a good approximation of the spread in photon arrival times. In a more realistic scenario, both Coulomb scattering and the changing index of refraction as the shower traverses through the atmosphere create features in the photon arrival times. Luckily, these are small effects.

2.1.3 Cosmic-ray Showers

The cosmic ray flux in the VERITAS energy range is dominated by protons. The cosmic ray spectrum is shown in Section 1.1.1. Hadronic showers resulting from protons thus form the bulk of background events for VERITAS. Fewer than 1% of air showers in the VERITAS energy range are initiated by photons. This section provides a brief discussion of the difference between cosmic-ray showers and gamma-ray showers.

When a cosmic ray enters the atmosphere, it generates a hadronic air-shower cascade that is broader and more highly scattered than the electromagnetic cascade induced by a photon of an equivalent total energy, as shown in Figure 2.4.

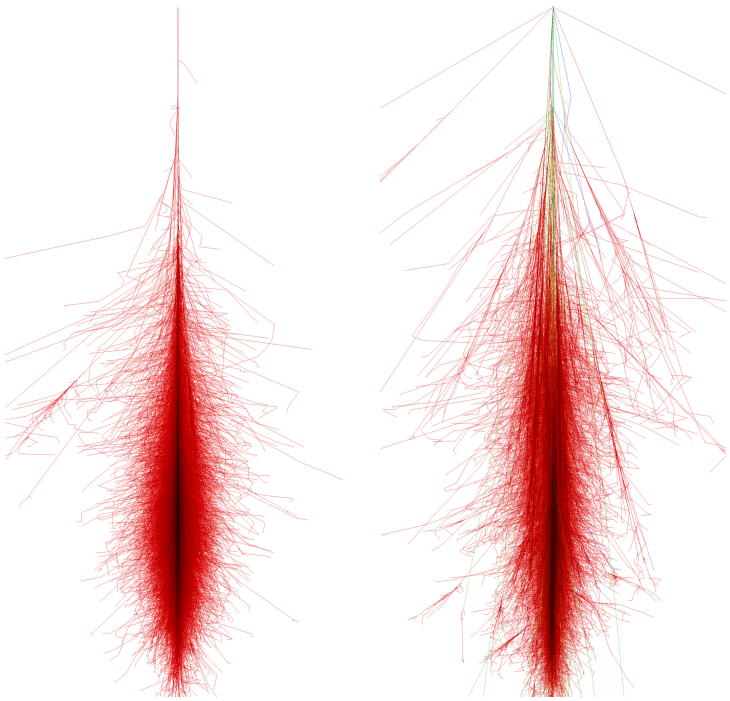

(a) Gamma-ray Air Shower (b) Proton Air Shower

Figure 2.4 Comparison of a 1 TeV gamma-ray shower (a) and a 1 TeV proton shower (b). Images were produced by Johannes Knapp and Fabian Schmidt using the Cosmic Ray Simulations for Kascade (CORSIKA) simulation package [32].

Proton-proton interactions produce $\pi^{\pm}$ and π^{0} particles with a large transverse momentum. The π^{0} decay into two photons with a characteristic energy equal to the mass of a π^{0}, while the $\pi^{\pm}$ decay to muons which in turn decay to electrons and positrons that are capable of producing their own smaller electromagnetic showers and Cherenkov radiation. The large transverse momentum of the initial pions gives rise to much of the broadening of the cosmic-ray induced shower. This difference in shower profile is the primary method

by which hadronic background is removed from VERITAS data during analysis. A more detailed discussion of background subtraction is provided in Chapter 3.

2.2 Imaging Atmospheric Cherenkov Telescopes

Due to the nature of Cherenkov radiation, an IACT uses the atmosphere as part of the detector. The Crab Nebula, a bright, steady source of gamma-ray emission, has a flux at 1 TeV of about 7 photons per square meter per year [55, 36]. Therefore, a ground-based array that can cover 10^5 m^2 has a great advantage over a space-based detector such as the Fermi gamma-ray space telescope, which uses scintillators with a collection area of less than 1 square meter above 100 GeV. By using the Earth's atmosphere as the first stage of the detector, an array of IACTs such as CTA will be able to achieve an effective collection area of about 10^6 m^2 between about 100 GeV and 30 TeV. See Figure 2.5.

IACTs use fast electronics that can record images at rates of a few hundred Hz to capture the Cherenkov radiation emitted during a gamma-ray induced electromagnetic air-shower. The multi-telescope array configuration allows for a multi-level trigger system that triggers predominately on showers [57], cutting down much of the night sky background. The intensity of the captured photons by a detector at a given distance from the shower axis provides an estimate of the energy of the primary gamma ray. Using multiple telescopes to image the same shower additionally improves sensitivity and directional reconstruction from the array to the shower core. [56]

There are currently three IACTs in operation. HESS[1] operates in Namibia and thus has good coverage of the southern sky. MAGIC[2] and VERITAS[3] both operate in the northern hemisphere. MAGIC is located on the Canary Islands, while VERITAS is located in the United States, in Arizona. These modern IACT arrays are sufficiently sensitive to detect

[1] https://www.mpi-hd.mpg.de/hfm/HESS/
[2] https://wwwmagic.mpp.mpg.de/
[3] https://veritas.sao.arizona.edu/

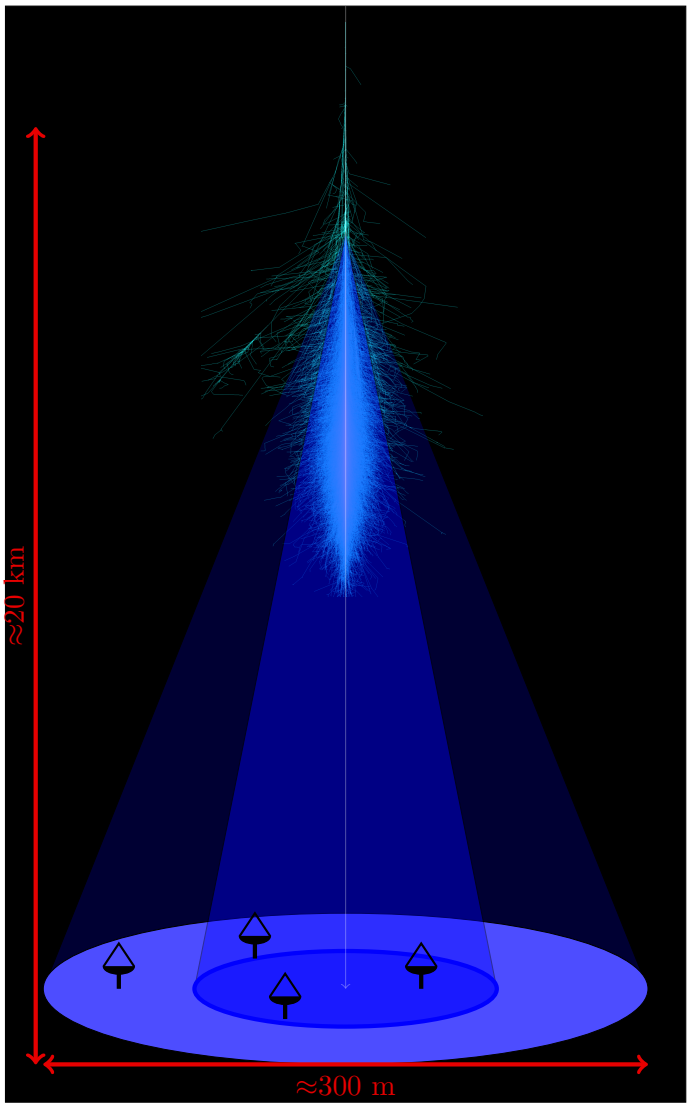

Figure 2.5 A gamma-ray induced air-shower hitting a 4-telescope IACT array.

sources with a flux of 1-3% of the Crab Nebula between about 80 GeV to 30 TeV in a few tens of hours [3].

2.3 VERITAS

The VERITAS array consists of four 12 m Imaging Atmospheric Cherenkov Telescopes (IACTs) located in southern Arizona at the Fred Lawrence Whipple Observatory (FLWO), at an elevation of 1270 m. The first two telescopes were operational from March 2006, with the full array of four telescopes coming online in April 2007. The T1 telescope was relocated in September 2009. The majority of this thesis focuses on the period after the relocation of the T1 telescope. The array after the T1 move makes a rough square with side length of approximately 100 m. Figure 2.6 shows the current locations of the VERITAS telescopes. The original location of T1 is marked in white text.

This section describes the telescope configuration, hardware, and data acquisition, followed by a detailed overview of the VEGAS analysis package, the primary analysis package used for analysis in this thesis.

Figure 2.6 Image of VERITAS, located at the Fred Lawrence Whipple Observatory (FLWO) in southern Arizona (31 40N, 110 57W, 1.3km a.s.l.).

2.3.1 VERITAS Detector

An alt-azimuth mount supports the steel-frame optical support structure (OSS) which supports the camera box at the focal length of the segmented mirror. All the cabling is run from the back of the camera box down through the center of the pedestal to a trailer located at the north side of each telescope. The trailers contain the high voltage sources for the camera, monitoring tools, and the first stages of data acquisition hardware further described in Section 2.3.1.2.

2.3.1.1 Mirror and Camera Design

The 12 m diameter mirror of each telescope consists of 345 hexagonal segments, following the segmented Davies-Cotton design [15]. Each mirror was treated to adjust the peak mirror reflectivity to coincide with the peak of the air shower Cherenkov spectrum. An aluminum layer was evaporated onto each mirror, and then an electric current was run through the aluminum to oxidize it. The reflectivity degrades over time due to environmental factors, however the reflectivity of clean mirrors reaches and exceeds 85% between 250 to 450 nm [26]. For normal operations over the course of VERITAS lifetime, mirror reflectivity degrades by about 3-6% at 320 nm per year. However, regular washing of the mirrors and periodic recoating with aluminum and anodization ensures that reflectivity remains close to 90% at the peak wavelength of 320 nm [53]. The mechanical pointing accuracy of the VERITAS system is approximately 0.01° [37].

The individual mirror facets also manually aligned periodically so as to minimize the point spread function (PSF), which describes the blurring of light arriving at the mirrors from a point source at a distance of infinity. The PSF determines the minimum resolution achievable by VERITAS. For observations of a source at the position of the telescope pointing or a small offset, the PSF is such that the majority of VERITAS sources can be treated as point sources in the camera. The PSF degrades for observations of a source at a large offset from the center of the camera.

The mirrors focus Cherenkov light onto a camera consisting of 499 photomultiplier tubes (PMTs), shown in Figure 3.2. The cameras have an 80% containment radius of 0.05 degrees for light originating from a point source. The field of view is 3.5 degrees [48]. The PMT signals are fed into both a constant fraction discriminator (CFD) and a flash analog-to-digital converter (FADC). The CFD determines whether the pulse height of the signal exceeds a set threshold. The threshold is set to select pulses that are above random background noise. One photoelectron corresponds to about 5 dc.

The original PMTs used in the cameras were Photonis XP 2970/02 ten-dynode photomultipliers. The peak quantum efficiency reached about 20-25% in the wavelength range from 270 to 550 nm. Light concentrators are attached at the front of the camera via a plate installed directly over the PMTs. The plate consists of molded plastic cones coated in evaporated aluminum with a protective layer, in a hybrid design based on Winston light concentrators [58] [42].

These reduce dead space between PMTs to 25% and shield the PMTs from ambient light, as well as capturing approximately 38% more light compared to the cameras with no light cones [42]. An image of a VERITAS camera with the light cone plate attached is shown in Figure 2.7

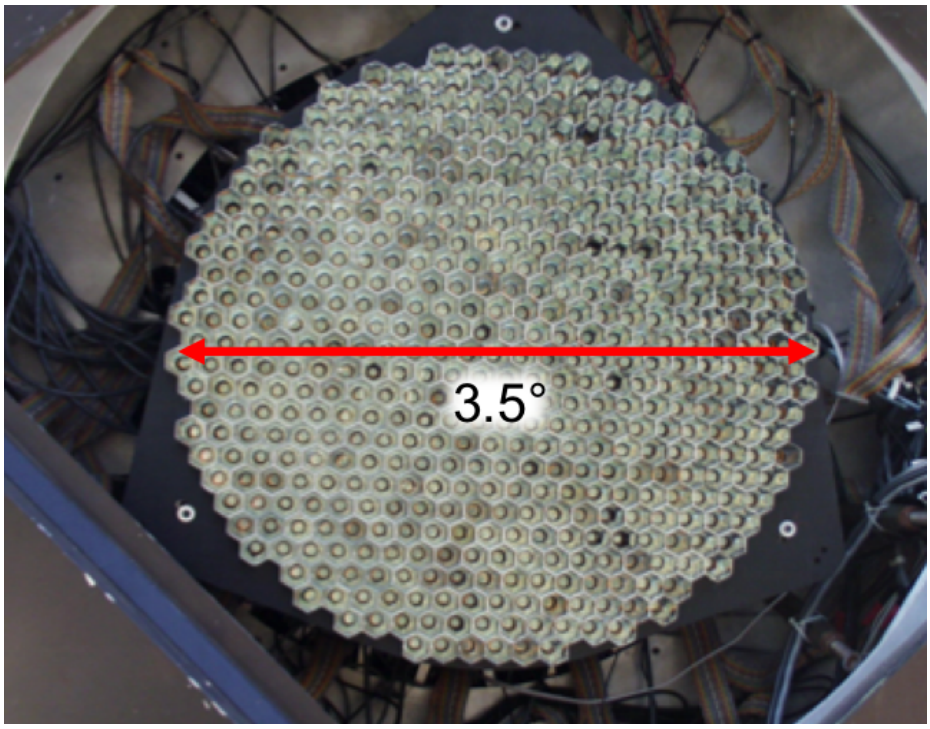

Figure 2.7 A VERITAS camera with 499 PMTs and light cones attached at the front of the camera, taken from Holder (2015) [38].

2.3.1.2 Data Acquisition

The PMT signals are fed into both a constant fraction discriminator (CFD) and a flash analog-to-digital converter (FADC). The CFD determines whether the height of the signal is significant above background noise. The FADC samples the PMT signal every 2 ns and converts the analog signal into a digital pulse measured in digital counts (dc). The fast response time is necessary due to the rapid signal from a Cherenkov pulse, described in detail in Section 2.1.2.4. One Cherenkov photon corresponds to about 5 dc. VERITAS uses 8 bit unipolar FADCs, which saturate at 256 dc. In order to extend the dynamic range from 256 to 1500 dc, a pixel trace going over 250 dc throws a switch to connect the FADC to a delayed low-gain channel that lowers the gain of the PMT trace by a factor of about 6 [52].

Positive FADC signals are truncated to zero. Night sky background (NSB) produces both positive and negative fluctuations in the PMT signal. The FADC readout, triggered at regular semi-random intervals, records the NSB convolved with electronics noise. This provides the basis for determining noise, given as a pedestal value in digital counts for each readout. The pedestal level is then important for determining cuts for image cleaning. The rate of the FADC readout is slow enough to have only an insignificant effect on array down time.

An array-wide read-out of the PMT traces is triggered by a coincident signal in at least two telescopes, with typical trigger rates of several hundred Hz [48]. An example of a PMT trace from simulations generated with CORSIKA-grISUdet is shown in Figure 2.8.

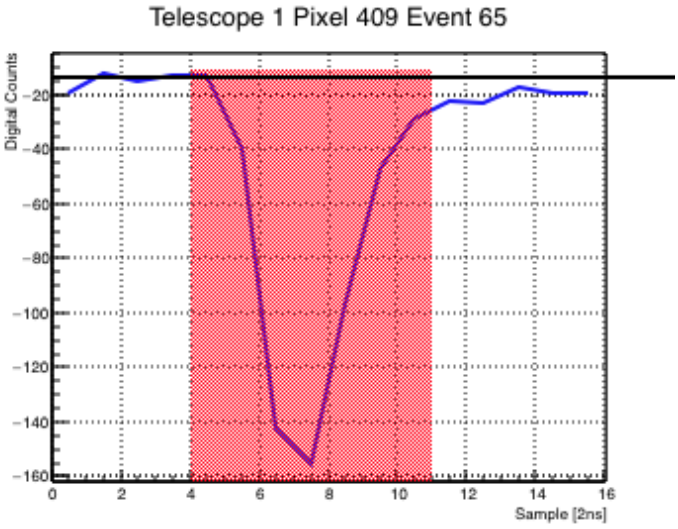

Figure 2.8 A pixel trace from data taken on the Crab Nebula in the V6 epoch. The black line shows the injected pedestal, while the red shaded region shows the 7-sample readout window over which the pulse is integrated to find the total charge in digital counts.

In order to trigger a gamma-ray event, there are three trigger levels. The level 1 (L1) trigger considers whether or not a PMT signal rises above the CFD threshold. The L1

corresponds to a PMT trigger. L1 is highly susceptible to NSB, and even sufficiently bright stars can cause L1 triggers. The second trigger level, L2, corresponds to a telescope trigger. Three nearest neighbor PMTs passing an L1 trigger within a coincidence time window of 5 ns are sufficient to trigger the L2. The L2 trigger is still susceptible to false positive from events such as bright stars that illuminate three or more pixels, cars passing by the basecamp, or white-light flashlights.

The final trigger level, L3, corresponds to an array trigger. Each L2 trigger is sent to a central control building. Delays due to differences in the distance traveled from each telescope to the control building and from propagation time of the shower across the array are corrected for at the control building. After accounting for these delays, the array trigger is satisfied when at least two telescopes pass an L2 trigger within a 50 ns window. An L3 trigger causes a 48 ns window around the detected signal to be read from the FADCs and stored for all pixels from all telescopes, regardless of which pixels and telescopes passed the L2 trigger. The array dead-time with this trigger system is 10% [57].

2.3.2 Instrument Epochs

The VERITAS array is separated into three different epochs of time, corresponding to changes to the array configuration. The epochs are defined as follows:

- **V4 (old array):** April 2007 - August 2009. All four telescopes online, with T1 in its original position between T2 and T4.
- **V5 (new array):** September 2009 - August 2012. T1 relocated to its current position between T2 and T3.
- **V6 (upgrade array):** September 2012 - Present. PMTs and level 2 trigger system were upgraded in all cameras.

T1 was the original prototype[4]. It's placement after all telescopes were brought online in 2007 was unchanged, which put it only 35 m away from T4. This lowered the sensitivity of the instrument, providing very little difference between three and four telescope operation. Therefore, in 2009 T1 was moved about 200 m east to its current location. T1 is labeled in its current position in Figure 2.6, with the original position during V4 marked in white text. The T1 move increased the sensitivity of the array by about 30% above 300 GeV [49].

In 2012, all Photonis XP 2970/02 PMTs were replaced with Hamamatsu R10560 PMTs. The upgraded PMTs in the V6 epoch improve the peak quantum efficiency and a have faster response time to photoelectrons. This provides an improvement to the photon yield of about 35% over the PMTs used in V4 and V5 [50]. Furthermore, the camera trigger systems (L2) were replaced by modern Field Programmable Gate Array (FPGA) electronics systems that were capable of triggering on a shorter coincidence time of 5 ns. This allowed VERITAS to trigger at a lower threshold and provided additional array capabilities for future expansion.

2.3.3 Data Taking

Data is taken on all nights outside of the monsoon season when the moon is less than about 65% illuminated, skies are clear to patchy with no rain or lightening in the vicinity, humidity less than 85%, and winds 30 mph gusts. Observers on sight are responsible for keeping an eye on the weather and logging weather, hardware or software problems, as well as events such as cars or people entering and exiting the basecamp during each night that the array in in operation. The array ceases data acquisition and shuts down each year for an approximately 2 month period during the summer, the time corresponding to the monsoon season in Arizona. During this time, large scale maintenance and instrument upgrades are performed.

Observations are typically taken between 25 and 85 degrees of elevation, in a mode known as *wobble mode*. This means that the telescope pointing is offset from the source

[4]Originally, VERITAS was planned to be located at Kitt Peak. Therefore, T1 was meant to be the only telescope located at the basecamp.

position by some angle. The typical wobble offsets for VERITAS is 0.5 degrees. Data is taken in 15 to 30 minute runs, depending on the epoch and source. In wobble mode, a single offset is used for the duration of the run, with the wobble direction cycling between the four cardinal directions for each new run on the same source. By offsetting the camera pointing from the source and cycling the pointing direction, the source and background can be taken from the same angular distance across the camera, thus accounting for the drop in acceptance from the center to the edge of the camera. A typical acceptance curve is shown in Figure 2.9. This method of background estimation follows the reflected region analysis as described by Berge (2007) [12].

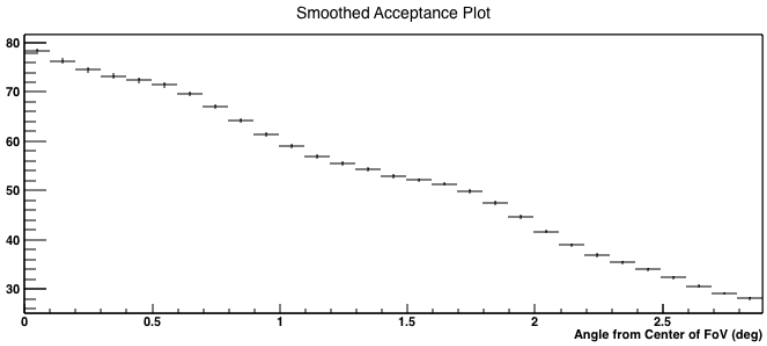

Figure 2.9 Acceptance rate within the VERITAS cameras as a function of distance from camera center. Plot was generated with data from the Crab Nebula, taken during winter months in the V5 epoch.

Typical PMT currents on a clear night with no moon are around 4-5 μA. Moonlight observations occur when the moon reaches around 30% illumination, typically during the rising or setting moon, and PMT currents rise above 10 μA. During moonlight observations, the CFD threshold is adjusted to decrease dead time due to increased NSB from moonlight. When the currents rise above 15 μA, the voltage to the PMTs can be reduced to continue observations. The telescopes can still operate up to around 65% moon illumination with high voltage reduced to 81% of nominal HV, and by pointing the telescopes at sources close to 90 degrees from the moon. The CFD threshold is decreased in this mode due to the

decreased PMT gain. Currents are monitored by current monitor boards located in the camera behind the PMTs, and displayed to observers via current monitoring software in the main building. During about a week around the full moon, no observations are taken as the currents are too high regardless of telescope pointing, even with reduced HV.

A calibration known as a *flasher run* is taken every night with an LED flasher containing seven LEDs. The flasher is attached to the quad arms of the camera and provides very stable and flat pulses of light that illuminate the entire camera equally. In addition, the L3 trigger is externally triggered in coincidence with the flasher pulses. The typical flasher rate is 300 Hz. This allows the PMTs to be monitored and calibrated every night, and provides necessary information to flatfield the PMTs so that the voltage applied to each PMT produces a roughly equivalent gain across the entire camera. The same flasher run can be used for both moonlight and dark time observations. Runs with reduced high voltage require a separate flasher run.

During daytime hours, the telescopes are stored uncovered facing north. The mirror is large enough to vaporize steel if pointed towards the sun. Therefore, great caution must be taken during any calibrations or maintenance that requires moving the telescopes during day time.

2.3.4 Data Quality Monitoring

Every member of the collaboration serves on a rotating basis as daily quality monitor (DQM). The DQM notes anomalies in a set of standard plots the morning after each night of observing. Anomalies from known sources such as weather are noted with the relevant flags, while problems of unknown origin are logged and investigated by an on-site support staff.

Weather conditions can dramatically affect the quality of data; it is given a grade on a scale of A-F by the observers, as well as monitored by FIR cameras during the night and graded again by the DQM. A weather corresponds to perfectly clear weather with no clouds

or haze. B weather indicates a few small clouds or haze, primarily due to large amounts of dust in the atmosphere. C weather indicates high, patchy clouds. D weather indicates large, low clouds with a few clear patches, while F weather means it is too overcast to observe.

CHAPTER 3. VERITAS DATA ANALYSIS

VERITAS data files are stored in the VERITAS Bank Format (VBF) and analyzed with software packages coded in ROOT, a object oriented data analysis framework developed by Rene Brun and Fons Rademakers at CERN[1]. Each VBF file contains a packet of information on each recorded event from a run. Runtimes on scientific sources typically cover 20–30 minutes of runtime, for up to hundreds of thousands of recorded events. The event packets hold a record of information from each participating pixel, including the full FADC trace for all image pixels in each telescope and the status of the CFD trigger. Additionally, each packet contains an event timestamp, event index, L2 trigger status of each telescope, and type of event (to distinguish between calibrations, simulations, or data). The VBF file also contains a header which denotes information such as source name, run start and end times, telescope pointing and offset from source, and a list of telescopes participating in the run.

3.1 Simulations

Because IACTs such as VERITAS allow one to reconstruct the direction and energy of an initial gamma ray from an image of the air shower it produces, comparisons to simulations are an important aspect of data analysis. For a standard analysis, air showers are simulated with CORSIKA [32]. The air shower information is then passed to the detector simulation package, grISUdet[2], developed by Grinnell College, Iowa State University, and the University of Utah. GrISUdet places VERITAS telescopes at the appropriate locations and maps the detector response from air-shower photons reflecting from the mirror facets

[1] http://root.cern.ch/

[2] www.physics.utah.edu/gammaray/GrISU/

to the camera, to the pixel response and production of full FADC traces for each pixel. A grISUdet pixel trace in high gain is shown in Figure 3.1. VERITAS electronics have two gain settings; these settings are discussed in more detail in Chapter 4. The output from grISUdet is a VBF file containing event and pixel information for each air-shower passed by CORSIKA. The output of grISUdet is equivalent to a VBF file produced during real data observations, and additionally includes a number of true parameters from simulations such as true energy and direction of the initial gamma ray and air shower. Because simulation files are produced without night sky background, pedestals and noise are added during analysis, with noise levels chosen by the analist in *grISU noise units*. The conversion from grISU noise units to pedestal variance (pedvar) in digital counts is shown in Table 3.1. Camera images produced by simulations are then used to separate cosmic ray images from gamma rays, determine gamma/hadron cuts, generate *lookup tables* for energy reconstruction, and generate *effective areas* for spectral unfolding.

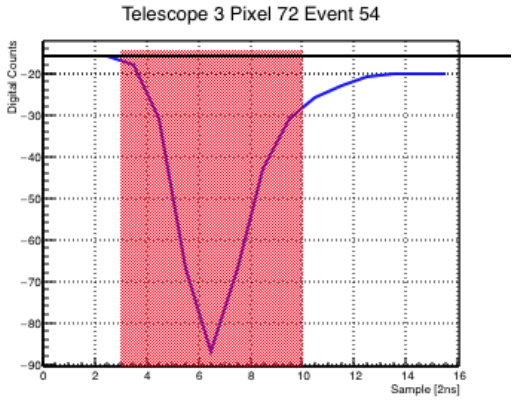

Figure 3.1 A high gain pixel trace from CORSIKA-grISUdet simulations for the V6 epoch. The simulations were run at a 20° zenith angle and winter atmosphere. The black line shows the injected pedestal.

The Cherenkov light pool varies as a function of several parameters including energy, source zenith angle, atmospheric conditions, and azimuth. The resulting camera image depends on the hardware and electronics that make up the telescope and data acquisition

system as discussed in Section 2.3. Knowing the true energy of the simulations allows for the construction of lookup tables of photon density as a function of shower core distance from the detector for a given energy bin. Standard VERITAS simulations are generated with a power law spectrum, $\frac{\mathrm{d}N}{\mathrm{d}E} = \left(\frac{E}{E_0}\right)^{-\Gamma}$ for initial energies between 30 GeV and 200 TeV and a power law index of $\Gamma = 2.0$. Lookup tables are further binned by the following parameters:

- Zenith angle — CORSIKA showers are simulated for VERITAS at zenith angles of 0, 20, 30, 35, 40, 45, 50, 55, 60, and 65 degrees.
- Azimuth — showers are simulated at all azimuths, and binned into eight bins between 0 and 360°.
- GrISU noise level — Added in grISU units of 100, 150, 200, 250, 300, 350, 400, 490, 605, 730, and 870.
- Wobble offset — The majority of simulations were performed at 0.5 degree offset, the typical wobble offset for VERITAS data-taking. However, simulations exist out to offsets of 2.0 degree offsets.
- Atmosphere — Binned into a "summer" and a "winter" season. Summer covers roughly May through October, while winter covers November through April. No data is taken July–August, due to the monsoons that hit Arizona during those months.

Table 3.1 Pedestal variance vs. grISU noise level for simulations run in October 2012 with a 7 sample readout window.

grISU noise	100	150	200	250	300	350	400	490	605	730	870
V4 pedvar (dc)	3.62	4.45	5.13	5.71	6.21	6.66	7.10	7.83	8.66	9.49	10.34
V5 pedvar (dc)	4.29	5.28	6.08	6.76	7.37	7.92	8.44	9.32	10.33	11.32	12.33
V6 pedvar (dc)	4.24	5.21	6.00	6.68	7.27	7.82	8.33	9.20	10.19	11.17	12.17

In addition to lookup tables for energy reconstruction, in order to generate a spectrum it is important to know what fraction of events are captured by the detector at a given

energy. Effective area files are constructed from simulations with the same binning as lookup tables, constructed as the fraction of events that trigger the telescope and pass gamma/hadron separation cuts at a given energy, multiplied by the area over which air showers are detected. Showers are thrown with a zenith dependent radius of 750 to 1000 m, which is well beyond the limit of the detector.

3.2 Overview of VEGAS Analysis Chain

VERITAS uses two primary analysis packages to reconstruct spectra from data: Event Display, a package developed by J. Holder, G. Meier, and others at DESY; and the VERITAS Gamma-ray Analysis Suite (VEGAS), developed by a number of VERITAS scientists since 2005. Independent analyses from the two packages allows for independent cross-checks of results, providing an excellent method for catching analysis errors early on.

All analysis carried out for this thesis uses VEGAS. This chapter therefore provides an in-depth overview of data processing and analysis as carried out by VEGAS. An outline of the analysis chain steps used in VEGAS is shown in Figure 3.2.

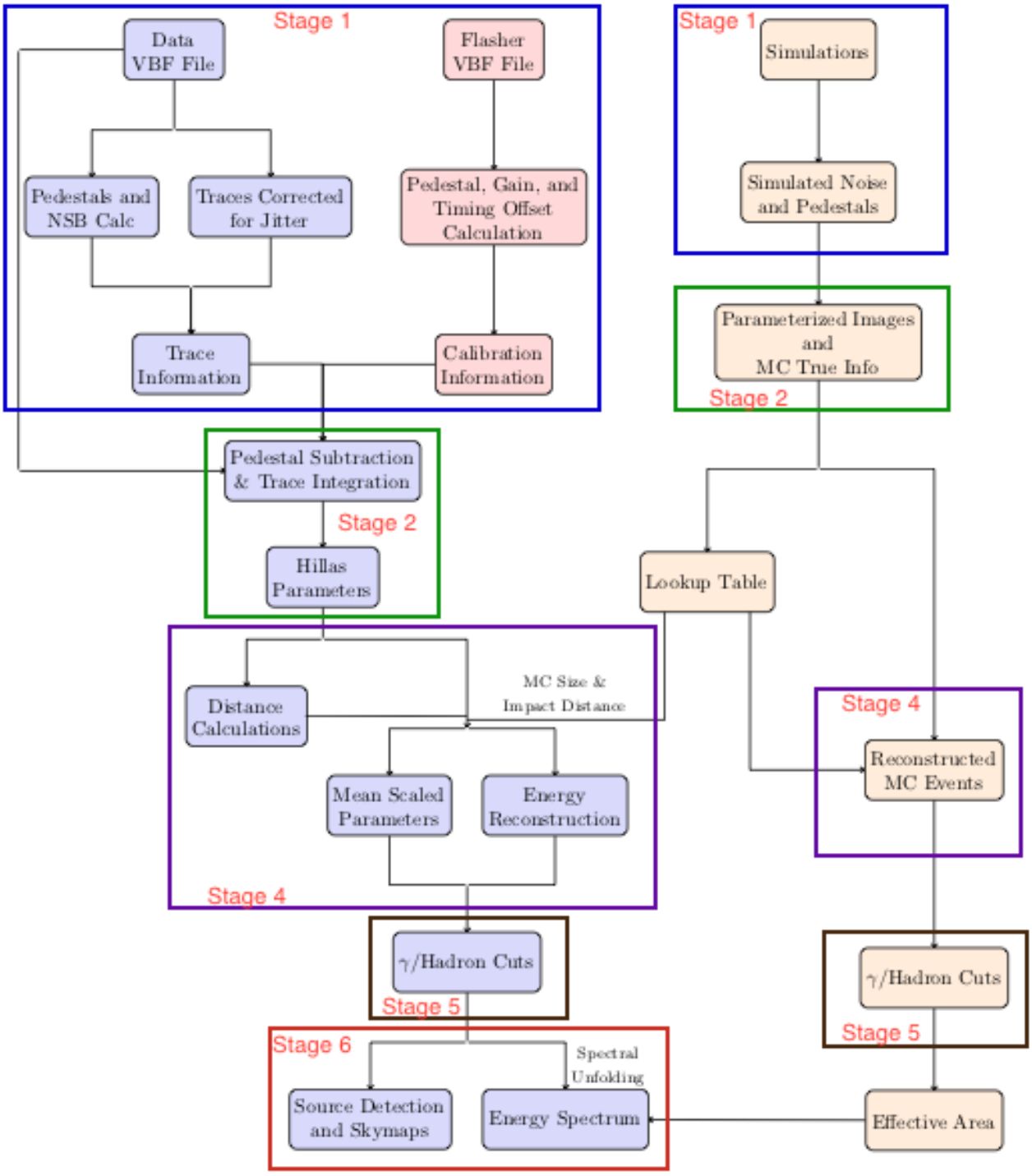

Figure 3.2 Schematic of the analysis chain carried out by VEGAS, the primary VERITAS analysis suite used throughout this thesis. Each stage of the VEGAS analysis is outlined in the colored squares.

VEGAS passes VBF files through several analysis stages to clean and parameterize images, remove background, and reconstruct the energy and direction of the initial gamma ray. Originally, data was passed through six analysis stages by VEGAS; however, current versions combine stages 2 and 3. Therefore, the analysis stages described in the following sections skip straight from stage 2 to stage 4. Figure 3.2 shows the steps taken in each stage, outlined in blue for stage 1, green for stage 2, purple for stage 4, dark brown for stage 5, and red for stage 6.

3.3 Event Reconstruction

The first and second stages of VEGAS clean and parameterize images resulting from air-showers and recorded in the VBF file. Each image in each telescope is assigned Hillas parameters that describe key elements of the recorded image [35]. The output from stage 2 is stored in a root file, and the VBF file is no longer used from this point forward.

Stage 4 calculates event level parameters and shower core, applies telescope level cuts, and calculates an energy for each telescope from a lookup table based on size and impact distance, before a weighted average energy is calculated for the array. Stage 5 applies event level cuts. Spectral unfolding occurs in stage 6.

3.3.1 Pedestals and Hillas Parameterization

The first stage of VEGAS analysis analyzes determines the pedestal values in each pixel from the flasher runs, and collects information such as tracking values from the database, if necessary. This stage runs on both flasher and data VBF files, which allows stage 2 to line up relative pixel timing and gain values for the full camera in each telescope. This ensures that relative pixel timing and gain values are calibrated every night. Stage 2 then uses the cleaned and calibrated trace information from stage 1 to calculate Hillas parameters for each image from each participating telescope in every event.

The first step requires determining which pixels constitute an image. Image pixels are determined by calculating the relative significance of the PMT signal to the background. A significance of 5σ or greater classifies the pixel as an image pixel. The image border is determined by pixels of significance of greater than 2.5σ. Any pixel whose trace falls below 2.5σ relative to the NSB level is classed as a noise pixel and removed from image consideration. Only image pixels and border pixels adjacent to image pixels are used to determine the Hillas parameters.

The participating pixels in each telescope that triggered on an event are characterized as elliptical images, following the method outlined by Hillas, primarily through the following parameters:

- **Width:** The semi-minor axis of the ellipse, corresponding to the quadratic spread from the centroid along the semi-minor axis of the ellipse.
- **Length:** The semi-major axis of the ellipse, corresponding to the quadratic spread from the centroid along the semi-major axis of the ellipse.
- **Distance:** The distance of the image centroid from the camera center, measured in degrees.
- **Size:** Sum of the total integrated digital counts in each image and border pixel.
- **NTubes:** The number of PMTs that make up the image.

An example of a Hillas parameterized image is shown in Figure 3.3.

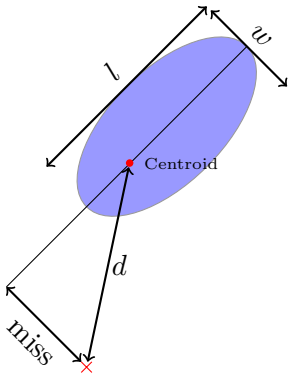

Figure 3.3 A Hillas parameterized camera image. Total size is given by the charge contained in the blue ellipse. The center of the field of view is marked by the red $\times$. Distance is labeled as d, length as l, width as w.

The output of stage 2 contains additional pixel information for diagnostics, as well as event information such as zenith angle and azimuth.

Finally, stage 4 calculates a number of event-level parameters from all the participating telescope images. Of particular importance to gamma/hadron separation discussed in Section 3.3.3 are the mean scaled length (MSL) and mean scaled width (MSW), calculated according to the method outlined by Daniel (2007) [13]:

$$MSP = \frac{1}{n}\sum_{i=1}^{n}\frac{p_i}{\langle p_i \rangle} \tag{3.1}$$

where p is the Hillas parameter in question, either length or width, and n is the total number of telescopes participating in the event reconstruction. The average value of the parameter comes from Monte Carlo simulations. Therefore, the MSW and MSL for gamma-ray images should peak around 1.

3.3.2 Direction, Distance, and Energy Reconstruction

The first level of event reconstruction are a set of telescope level cuts over several of the Hillas parameters that ensure the remaining events are useful for reconstruction, applied in

stage 4. A table of telescope level cuts at the three different levels used by VERITAS for the three instrument epochs is shown in Table 3.2.

Table 3.2 Telescope level cuts applied in stage 4. Additionally, images that were captured only by T1 and T4 are removed for the V4 epoch — the two telescopes were too close together to provide meaningfully distinct information as an array before the T1 move.

	V4	V5	V6
Soft	Distance $< 1.43°$ Size > 200 dc NTubes > 5	Distance $< 1.43°$ Size > 200 dc NTubes > 5	Distance $< 1.43°$ Size > 400 dc NTubes > 5
Medium	Distance $< 1.43°$ Size > 400 dc NTubes > 5	Distance $< 1.43°$ Size > 400 dc NTubes > 5	Distance $< 1.43°$ Size > 700 dc NTubes > 5
Hard	Distance $< 1.43°$ Size > 1000 dc NTubes > 5	Distance $< 1.43°$ Size > 1000 dc NTubes > 5	Distance $< 1.43°$ Size > 1200 dc NTubes > 5

The cuts on a minimum size and number of image pixels eliminate NSB and low energy background. Additionally, larger images are easier to parameterize. Therefore, the size and NTubes cuts ensure only images for which second moments of area can be reconstructed are allowed to participate in the event reconstruction. This sets the low energy threshold for the detector. Below about 100 GeV, images are too dim to accurately reconstruct their resulting images in a VERITAS camera. Soft cuts use a lower cut on image size in order to capture more low energy events. This has the drawback of also accepting more background, and allowing greater error in the direction and distance reconstructions, due to higher uncertainty in the shape of dimmer images.

The cut on distance minimizes loss of light from images leaking off the edge of the camera. As an image approaches the camera edge, the size of the camera cannot capture the entire image. Therefore, an upper bound is placed on the distance of the centroid to the edge of the camera to mitigate this. This cut removes both very distant events and events with high energy. Above a few 10's of TeV, events become degenerate due to the inability

of VERITAS to capture the full shower. Therefore, images above this threshold are difficult to accurately reconstruct.

Once only useful images remain, the direction and energy of remaining events can be reconstructed. Even with a single telescope, such as was the case with the Whipple 10 m telescope, the image shape can be used to obtain information about direction and distance of events. However, direction and distance reconstructed from only a single telescope leads to larger statistical errors than can be obtained with multiple telescopes [43] [47]. An array of multiple telescopes provides a great benefit to the reconstruction of gamma-ray events through the ability to more precisely reconstruct direction, distance of the shower axis from the detector, and initial energy.

The direction of the shower is essential information to ensure that events making up a spectrum arrive from the source location. To determine the direction the shower arrived from, an average direction is calculated from the participating telescope images. First, the direction of the image in the camera is reconstructed in degrees in the camera coordinates for each parameterized camera image. Next, a weighted average over all the participating telescope images is calculated by minimizing the square of the directions. This information in camera coordinates can then be converted into both azimuth and elevation coordinates relative to the array, as well as RA and Dec coordinates, based on the tracking position of the telescope in azimuth and elevation.

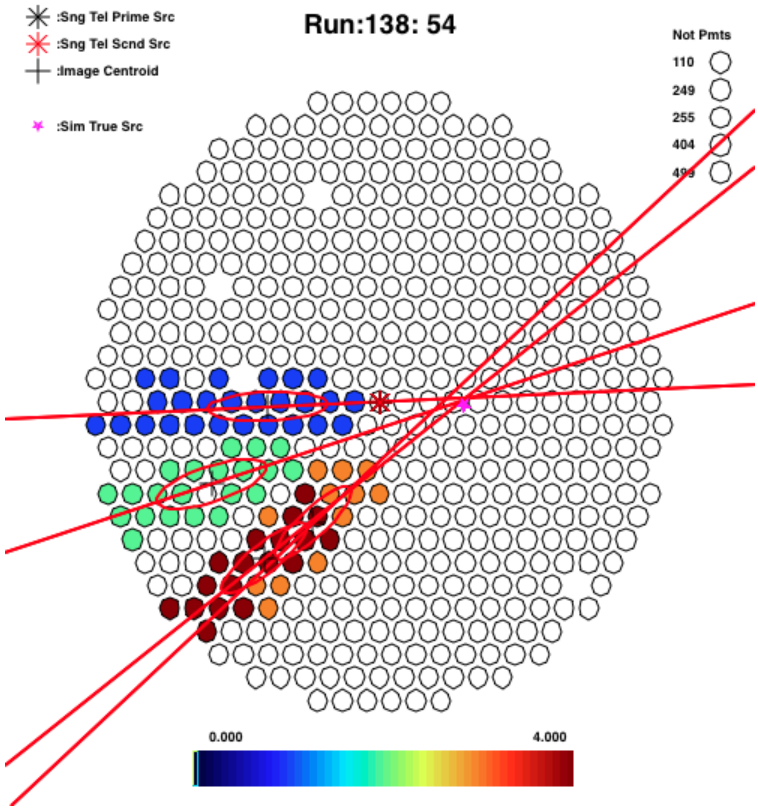

Figure 3.4 The direction reconstruction as visualized with vaDisplay, the event viewer for VEGAS, for an air shower induced by an 800 GeV gamma ray. The four Hillas images are shown in the red ellipses overlaying the colored pixels, with the lines passing through the major axes intersecting at the camera coordinates corresponding to the origin of the shower. The location of the true shower direction in the camera is shown by the pink star.

This direction reconstruction carries important information about how likely it is that a given reconstructed event arrived from the source, or from background within the field of view. The weighted average of direction for each event is also stored as a single value, Θ^2, denoting the direction of each incident gamma ray as a function of squared angular distance from the source position. Figure 3.4 shows a reconstructed direction for a shower from CORSIKA-grISUdet simulations.

In addition to the direction reconstruction, the initial energy of the incident gamma ray is an essential quantity if a spectrum is desired. As discussed in Section 2.1, the lateral light distribution of a Cherenkov shower varies with both distance from the shower axis and initial gamma-ray energy. Therefore, reconstructing initial energy in VEGAS requires both the total size of the image and the distance of a given shower core in the mirror plane from the telescope that imaged it. This second quantity is described by the *impact distance*. The distance of the shower core from the center of the array is described by *core distance*. Core distance, impact distance, and energy reconstruction are among the event-level parameters calculated in stage 4.

With two telescopes, the core location is provided directly by the intersection of the lines extending through the major axis of the two images in the mirror plane. The mirror plane is given by a rotation from the ground plane based on the telescope tracking position. A small variation in the reconstructed angle of these lines can still produce large offsets in the reconstructed distance. Both images of small size and more circular images from events falling near the telescope have a large margin for error in the decision of the major axis. Therefore, the greater the number of telescopes in the image, the greater the accuracy of the reconstructed core distance.

The calculation of core distance in VEGAS uses the telescope positions and direction towards the shower core to calculate a weighted average of the intersection of lines drawn through the major axis of the images from each participating telescope in the direction of the shower core, calculated in the mirror plane. The standard analysis uses $\log_{10}(\text{size})$ as the weight. This means that brighter images have a higher impact on the reconstructed core location.

Once the core distance is known, the impact distance for a telescope is a simple geometric calculation of the distance from the telescope to the core location. An example of the core distance reconstruction is shown in Figure 3.5.

Even for two telescopes, VEGAS does an excellent job at reconstructing impact distance and core location. Shown in Figure 3.6 is the core distance bias, $(C_{\text{rec}} - C_{\text{true}})/C_{\text{true}}$, as a function of true energy for simulated events at 20° zenith angle. The core is well reconstructed with only a few percent bias on the mean and about 10-20% resolution.

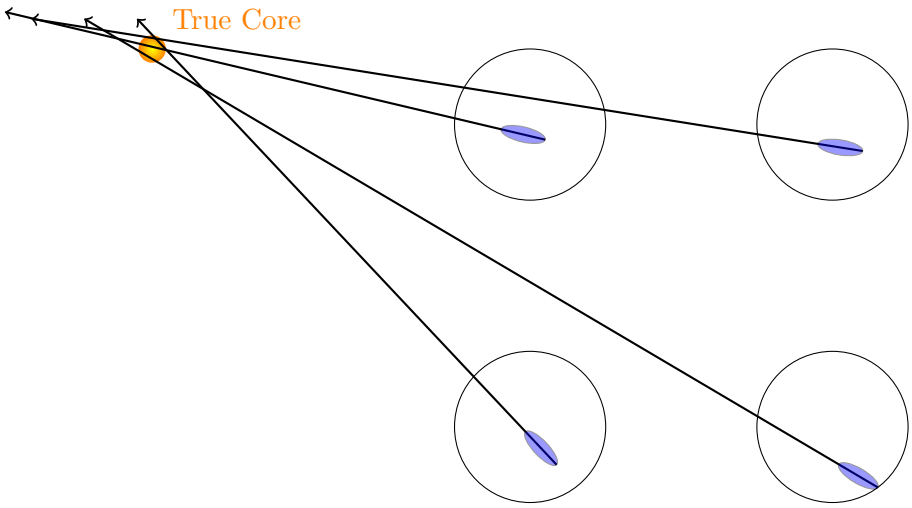

Figure 3.5 The reconstructed core distance from four telescopes, with the true core labeled in orange. While any two telescope intersections have some associated error, the average of the intersections provides a fairly accurately reconstructed core.

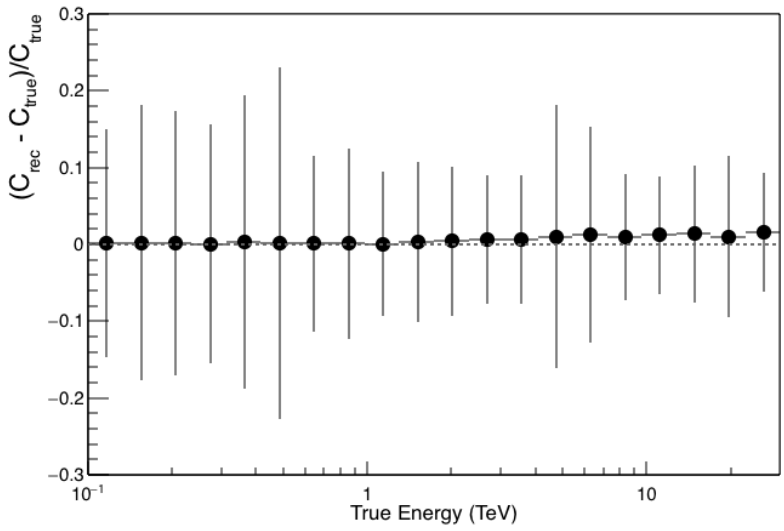

Figure 3.6 The bias in the core location reconstruction for gamma-ray events arriving from 20° zenith angle in the V5 epoch.

A reconstructed energy is calculated after the distance reconstruction based on lookup tables derived from simulations, binned in impact distance and size. The PMTs in both the V5 and the V6 epochs were designed with a gain of about 2×10^5. For data taken in V5 and V6, the ratio of digital counts measured per photoelectron (pe) generated at the cathode in high gain mode corresponds to approximately 5.6 dc per pe [52]. The low gain channels have a gain approximately 6 times lower than the high gain channels, or < 1 dc per pe. This ratio is measured each year during standard seasonal calibrations.

In stage 2, the total image size is calculated based on a high to low gain ratio passed by the user, for a total size corresponding to an image entirely measured in high gain and with a dynamic range of 1500 dc. Comparing the size and impact distance of an image to the photon density plots in Section 2.1.2.3 then provides a measurement of the initial gamma-ray energy. This is done in stage 4, using lookup tables of image size and impact distance calculated from the simulations described in Section 3.1. The reconstructed energy of each participating telescope is then weighted by the size, giving higher importance to brighter

images. Finally, a reconstructed energy for the event is calculated from a weighted average of the individually reconstructed energies from each participating image. The resolution on the reconstructed energy is driven by statistical fluctuations in various properties of the air shower and uncertainties in the detector. In both V5 and V6, the reconstructed energy has a resolution of about 15-20% [48].

3.3.3 Gamma-Hadron Separation

Because real data is dominated by cosmic-ray background, a list of cuts to separate gamma-ray showers from hadronic showers is applied in stage 5. Stage 6 then applies a further cut on Θ^2 to remove diffuse gamma-ray background from within the field of view that is unlikely to have originated from the source of interest. These event level cuts from stages 5 and 6 are shown in Table 3.3[3].

Table 3.3 Table of gamma/hadron cuts applied in stages 5 and 6.

	Stage 5		Stage 6	
Soft	$0.05 <$ MSW	< 1.1	Θ^2	< 0.03
	$0.05 <$ MSL	< 1.3	RingSize	$= 0.17°$
	Shower Height	< 7 km	RBM SearchWindowSqCut	$= 0.03$
Medium	$0.05 <$ MSW	< 1.1	Θ^2	< 0.01
	$0.05 <$ MSL	< 1.3	RingSize	$= 0.1°$
	Shower Height	< 7 km	RBM SearchWindowSqCut	$= 0.01$
Hard	$0.05 <$ MSW	< 1.1	Θ^2	< 0.01
	$0.05 <$ MSL	< 1.4	RingSize	$= 0.1°$
			RBM SearchWindowSqCut	$= 0.01$

The average width and length parameters used in the calculation of MSW and MSL in Equation 3.1 are taken from simulations of gamma-ray showers. Therefore, showers initiated by gamma rays in the atmosphere are expected to peak at about 1 in both MSW and MSL distributions. Cosmic-ray initiated showers are often much messier, and peak well beyond 1

[3]Because of the incorrect calculation of shower height in the standard VEGAS analysis package, all analyses in this thesis were done without the shower height cut in stage 5. See Chapters 2 and 6 for further discussion.

in MSW in particular. Therefore, cutting mean scaled parameters around 1 removes much of the cosmic-ray background while preserving the majority of gamma-ray events.

As described in the previous section, Θ^2 determines the squared angular distance of an incident photon from the source location. For data, the source location is smeared by the PSF of VERITAS. Therefore, the cut must be broad enough to encompass the majority of the source photons, while cutting close enough so as not to contaminate the total photon counts from the source with too much background. All the sources in this thesis are treated as point sources, which are well contained by a standard Θ^2 cut of 0.01°. *Ring Size* and *RBM search window* are described in the following section.

3.4 Spectral analysis

The following sections describe the different methods of background correction and spectral reconstruction used by VERITAS.

3.4.1 Background Estimation

Any given source position sits on top of a diffuse cosmic-ray background that contaminates the measured flux at the source. To properly estimate the desired source flux, this background must be subtracted from the source region. There are two primary methods by which a standard VERITAS analysis estimates this background. The ring background model (RBM) positions the source at the center of the camera and uses a ring of constant angular distance from the source to calculate background. The primary drawback to this method is that it positions the ON and OFF regions at different angular distances from the center of the camera. Camera acceptance drops as a function of angular distance from the center of the camera (see Figure 2.9 from Chapter 2). Therefore, the background counts must be corrected for the change in acceptance, which requires deep knowledge of the acceptance curve over a wide range of observation conditions.

Typically, the VERITAS analysis instead uses the reflected regions model described by Berge [12], hereafter referred to as the *wobble method*. The wobble method accounts neatly for the drawback of the RBM. In wobble mode, the camera tracks a location at a given offset from the source. The background can then be taken from the same ring in the camera as the data, ensuring that the acceptance for both regions is equivalent. VERITAS additionally cycles the wobble direction between the four cardinal directions, to ensure that any biases from acceptance across the camera in zenith are averaged out of the final analysis. An ON region described by a ring of radius about 0.1° is sufficient to cover point sources observed by VERITAS. The OFF regions at a given wobble position are then described by OFF rings of equal radius spaced around the camera at equal angular distance from the center of the field of view. An OFF region is excluded from analysis if it contains contaminants such as bright stars or known sources in addition to the source of interest. Figure 3.7 illustrates the two methods of background estimation.

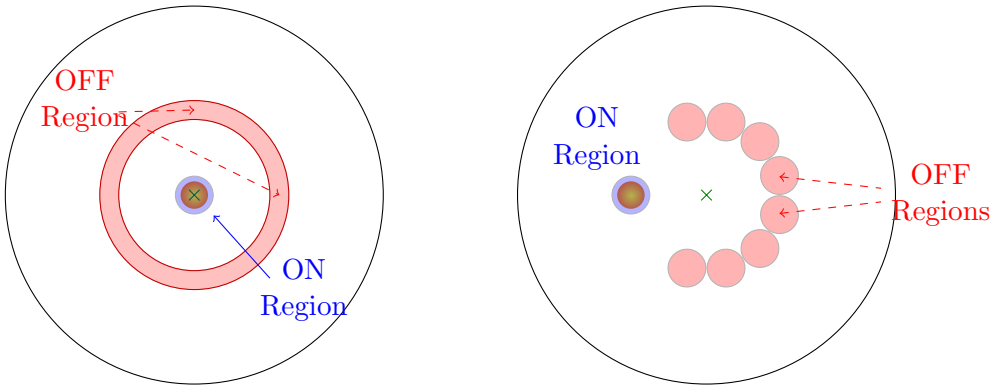

(a) RBM (b) Wobble Method

Figure 3.7 The two methods of background estimation for analysis of VERITAS data. RBM is shown in (*a*), while the wobble method is shown in (*b*). The green crosses show the telescope tracking position.

The measured OFF counts, corrected for the number of OFF regions relative to ON regions, can then be subtracted from ON counts that fall within the 0.1° ring around the

source. This leaves excess counts that are assumed to originate from the source. The statistical significance of the excess counts can also then be determined from the relative source signal to background rate, following the method outlined by Li and Ma [45]. Sources of interest to VERITAS are considered detected if they reach a significance greater than 5σ.

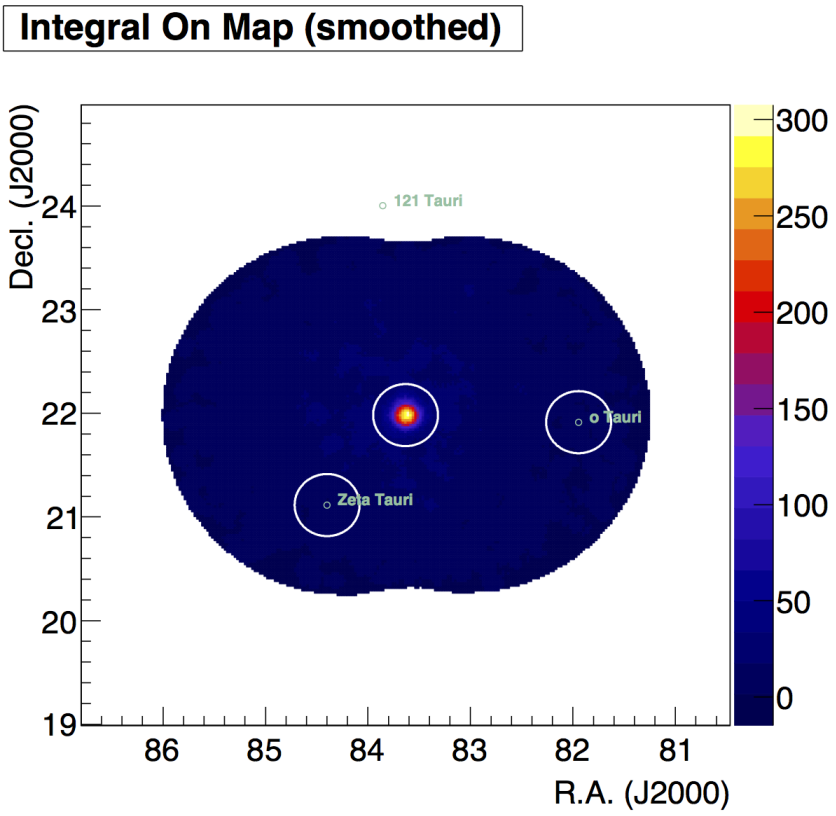

Figure 3.8 A skymap of smoothed counts from 2 20-minute observation runs on the Crab Nebula, taken during the V5 epoch near 20° zenith angle, in the winter season. The wobble offsets were at 0.5° "east" and "west," respectively. The color scale shows the number of ON counts from the region within the central white circle.

A skymap of data from the Crab Nebula is shown in Figure 3.8 for two runs near 20° zenith angle. The source is ringed by the ON region of 0.1° radius, and the OFF regions are taken from rings at the same camera offset. Each OFF ring also has radius of 0.1°.

Three bright stars are labeled inside white rings. Bright stars are taken from the database, covering a region that accounts for all wobble offset directions. The bright star outside of the blue rings covering the VERITAS observations would be captured by a north wobble offset, and is therefore still shown on the skymap. These regions are excluded from analysis.

3.4.2 Effective Areas and Spectral Unfolding

In order to reconstruct a spectrum, it is necessary to understand the fraction of events that trigger the detector as a function of initial energy. This is determined from simulations as described in Section 3.1. The effective area accounts for the energy-dependent detector response and energy resolution of the detector, in a process known as "spectral unfolding". Spectral unfolding converts raw excess counts from a given energy bin into gamma-ray flux, $\frac{dN}{dE}$, in units of $\mathrm{TeV}^{-1}\mathrm{m}^{-2}\mathrm{s}^{-1}$, by dividing the raw distribution by the effective area. Scientific information can then finally be extracted from the resulting spectrum.

The process of spectral unfolding is complicated by the fact that events in real data only have a reconstructed energy. The reconstructed energy of an event can migrate between different true energy bins of the effective area, due to errors on the reconstruction as discussed further in Section 3.5. Because of this migration of real events between different energy bins, the calculation of effective area is dependent on the spectrum of the source being studied. As discussed at the start of this chapter, all simulations produced with the CORSIKA-grISUdet simulation chain are produced over a power law spectrum of index $\Gamma = 2$. While the majority of sources studied by VERITAS can be fit with power law spectra, the index varies widely between hard spectra of index $\Gamma < 2$ to soft spectra of $\Gamma > 4$. Therefore, an analyzer inputs estimated spectral parameters for data during spectral analysis, and the effective area is re-weighted on the fly during analysis following the new spectral parameters.

The re-weighting is done via a *Migration Matrix*, M_{ij}, that tracks the number of events in each true energy bin, i, which migrate in to bin j in reconstructed energy. Then the known

distribution of simulated events in true energy bins is transformed into a distribution in reconstructed energy by smearing each bin by the fraction of mis-reconstructed events in that bin, as calculated by the migration matrix. This process allows for the effective area to be corrected for any input spectral parameters, and can be redone by the analyzer multiple times to narrow in on a more accurate reconstruction via iterating on the input spectrum based on the result of each trial.

The response of the detector varies with a number of parameters: zenith, azimuth, noise level, wobble offset, and atmosphere. Therefore, effective areas are also generated over a range of each of these parameters, with the same granularity as the lookup tables. A distribution of ON and OFF events is then created for each bin in reconstructed energy from the averaged distributions over all the detector parameters, with the OFF events weighted by α. Finally, points in a spectral histogram are obtained by subtracting the OFF distribution from the ON distribution, and applying the mean value theorem in each energy bin via the method described in [44]. The mean value theorem says that a data point in a bin of finite width (in this case, finite bins in gamma-ray energy) should be placed at the energy corresponding to the mean value of the predicted function over the range of the bin, rather than at the central value or barycentre of the bin.

A typical VERITAS effective area for a angle of 20° from the zenith (*zenith angle*) and medium analysis cuts in the V5 epoch is shown in Figure 3.9. The sharp rise around 100 GeV shows the low energy threshold of the detector, while the steep drop at several 10's of TeV shows the high energy threshold of the detector.

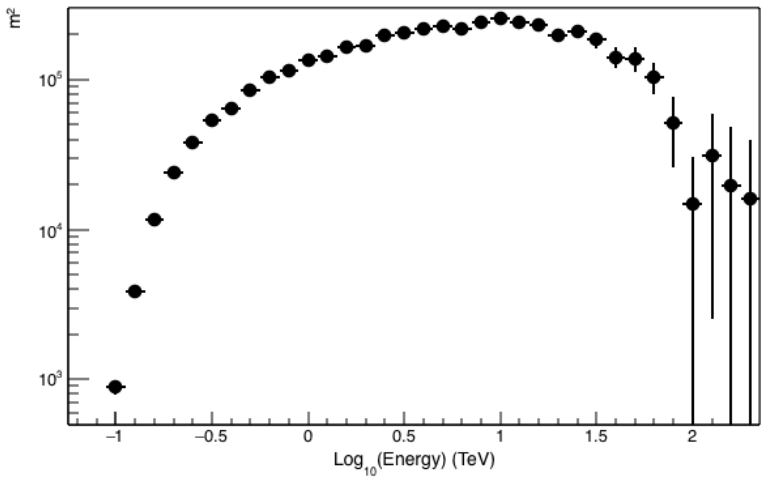

Figure 3.9 An effective area from V5 simulations at 20° zenith angle. Simulations were generated with the CORSIKA-grISUdet simulation chain.

3.5 Systematics

The energy bias for a VERITAS spectrum is impacted by systematic biases introduced by both statistical fluctuations in the showers and by detector limitations. These systematic biases affect the shape of the reconstructed spectrum. Because the spectral shape encodes important scientific information of interest to VERITAS from a given source, it is extremely important to understand the sources and impacts of systematic bias in the detector.

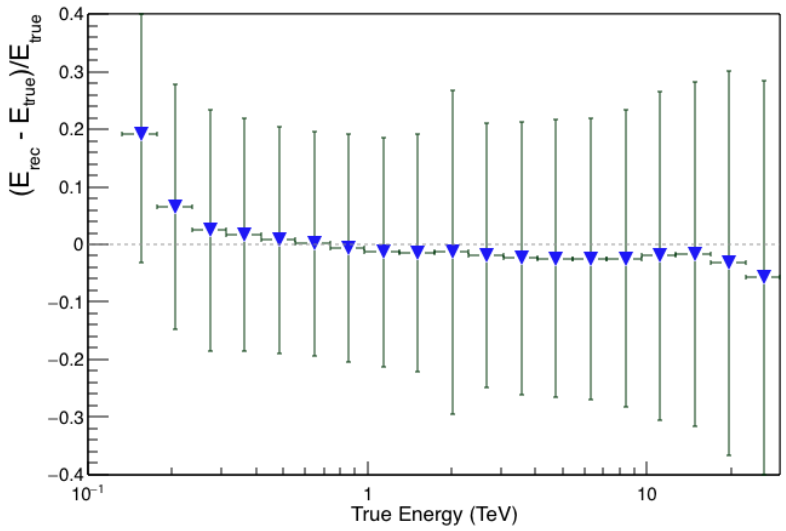

Figure 3.10 An energy bias curve for simulations at a 20° zenith angle during the V5 epoch. The green error bars represent the energy resolution in each bin.

This thesis focuses primarily on two sources of systematic bias: saturation of the electronics measuring the total charge under the pulse, and variation in height of shower maximum. This chapter concludes with a brief introduction to these biases.

3.5.1 Saturation in Low Gain

VERITAS uses 2 ns sampling, 8-bit unipolar FADCs, which saturate at 256 digital counts (dc). In order to extend the dynamic range from 256 to 1500 dc, the analog PMT signal is split and fed into two separate amplifiers with different gain factors. The low gain amplifier was designed to have a high-to-low gain ratio (referred to hereafter as simply "low gain ratio") of 6 and a delay from the high gain channel of 35 ns [52]. A pixel trace which exceeds 250 dc throws the switch that connects the FADC to this delayed low-gain channel, which produces a scaled down pulse which is read out instead of the truncated high gain pulse, as shown in Figure 3.11.

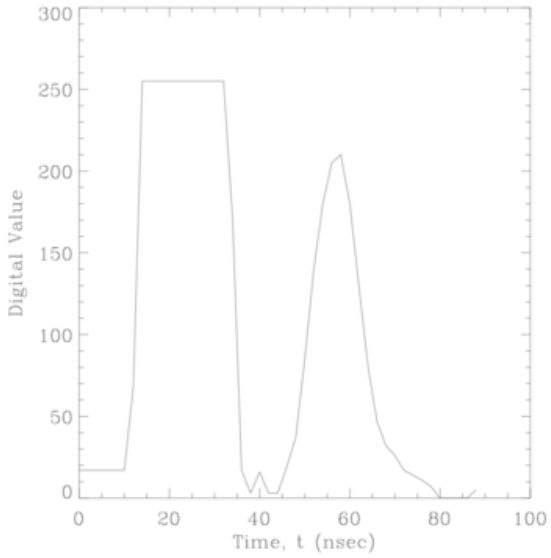

Figure 3.11 Delayed low gain pulse following the truncated high gain pulse.

Although the gain switch was built to have a ratio of 6 between the two gain values, the true ratio varies between instrument epochs. For data analyzed with the VEGAS analysis package, the default low gain ratio was set to 6 in V5 and to 5.8 in V6. However, analysis shown in Chapters 4 and 5 indicate that the true values of the low gain ratio in each epoch are lower than those applied in a standard analysis.

In addition to the value of the low gain ratio, saturation effects can lead to systematic bias in the energy reconstruction. Even with the extended dynamic range provided by the low gain switch, pixel saturation from extremely bright, high energy showers can become a significant source of bias to the energy reconstruction. The upgraded PMTs which define the V6 epoch peak more sharply, and thus both enter and saturate the low gain more quickly, than the PMT pulses from the V5 epoch.

The difference in pulse shape between the high and low gain channels also introduces yet another complication. The detector simulator, grISUdet, uses only one pulse shape. In the high gain channels, the pulse is multiplied by the high gain value. In the low gain channels, the pulse is multiplied by the high gain divided by the high/low gain ratio. In real data,

however, the electronics involved in switching from high to low gain introduce lag time that shift and broaden the pulse. Therefore, a low gain pulse in data additionally begins to leak out of the 7-sample readout window before it has begun to saturate. A comparison of a typical simulated pulse in low gain with a typical low gain pulse from data is shown in Figure 3.12.

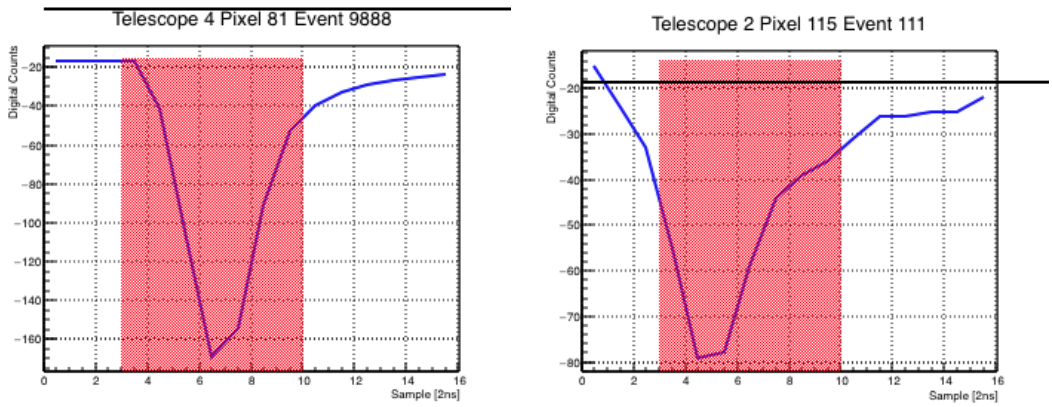

(a) CORSIKA-grISUdet Low Gain Pixel Trace (b) Low Gain Pixel Trace from Data

Figure 3.12 Comparison of a low gain pixel trace from CORSIKA-grISUdet simulations in (a) and Crab Nebula data in (b). The red shaded region shows the 7-sample readout window over which the pulse is integrated to find the total charge in digital counts.

The body of simulations run in October 2012, on which all subsequent analyses were based, used a high to low gain ratio of 5 rather than 6 for the detector simulator, regardless of epoch. Because of this, simulated low gain pulses saturate more quickly than real pulses in data, a feature exacerbated by the broadening of the low gain pulses in data. This effect also competes with the loss of light from data pulses leaking out of the readout window and the difference between the true value of the low gain ratio compared to the value used in simulations, thus muddying the expected effect of saturation. Figure 3.13 shows a cartoon example of this effect.

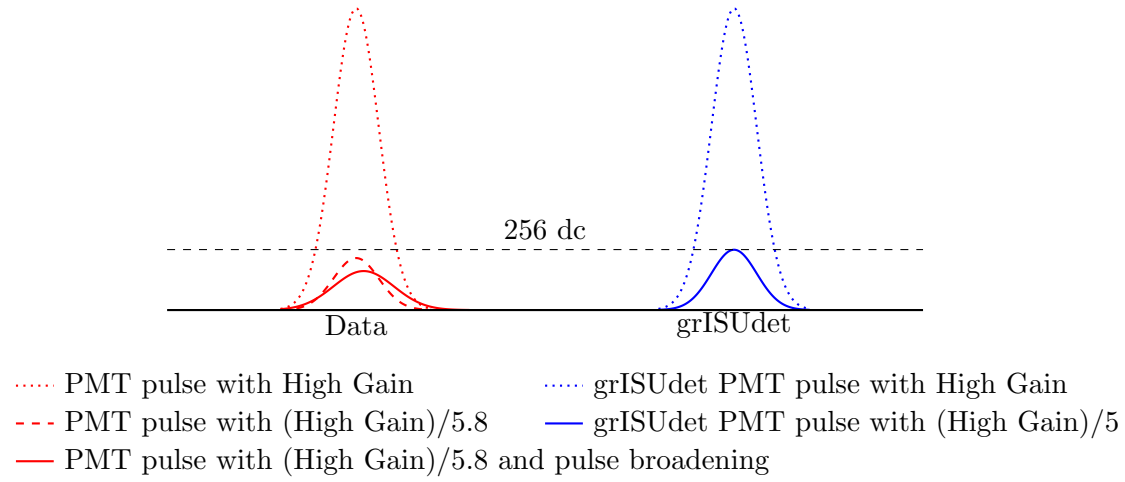

Figure 3.13 Cartoon effect of a mismatched low gain ratio in data and simulations. A nominal PMT pulse scaled by a high gain factor, G, is shown in the dotted red lines. The solid blue line shows a PMT pulse scaled by $G/5$, consistent with grISUdet simulations. The dashed red line shows a PMT pulse scaled by $G/5.8$, consistent with real data. The solid red line shows the same low gain PMT pulse with some broadening applied, for a more realistic model of a low gain trace in data. The threshold for FADC saturation is shown in the dashed gray line, at 256 dc.

An investigation of the systematic bias caused by pixel saturation in the low gain channels is discussed further in the next chapter.

3.5.2 Variations in Shower Maximum

While an average expected shower maximum can be calculated following the procedure outlined in Section 2.1.2.2, the true shower height for a given shower varies based on statistical fluctuations in the atmosphere. These fluctuations are especially relevant at the low energy threshold, where only the brightest showers trigger the detector. Showers occurring

deeper in the atmosphere produce a brighter image in the detector because the light has diffused over a shorter path, and thus more photons hit the detector.

Shower height fluctuations are largely responsible for the sudden rise in the VERITAS energy bias curve at the low energy threshold, which is discussed further in Chapter 6. This feature causes incident gamma rays with energies near the threshold energy to be reconstructed to higher energies, causing an artificial turnover in the low end of the spectrum.

CHAPTER 4. SATURATION AVOIDANCE METHOD

As detailed in Chapter 2, each VERITAS camera contains 499 photomultiplier tubes (PMTs), whose analog pulses are converted to digital traces by flash analog to digital converters (FADCs) [52]. VERITAS uses 8 bit unipolar FADCs, which saturate at 256 digital counts (dc). The dynamic range is extended from 256 to 1500 dc by applying two gain modes. A pixel trace going over 250 dc throws a switch to connect the FADC to a delayed low-gain channel that lowers the gain of the PMT trace by a factor of 6 [52]. However, even with a dynamic range of 1500 dc, pixels saturate at the high energy end of the VERITAS energy range, at energies above a few TeV. Additionally, because the low gain traces are delayed and broadened by the electronics with no corresponding widening of the readout window, low gain traces leak from the window over which they are integrated, lowering the effective size of the trace. The amount of light that leaks from the readout window of the broadest pulse in an image depends on shower energy. This broadening is not accounted for in simulations, which use the same pulse shape for high and low gain (see Figure 3.12). Both of these effects can produce a significant source of bias to the energy reconstruction.

The radial dependence of Cherenkov light density on the ground from a high energy shower offers a nice way to measure this bias (See Figure 4.1). When viewing a Cherenkov shower from the ground, taking into account the physical profile of the shower can lead to better understanding of the energy reconstruction. The intensity of light in the image remains roughly flat from the shower core out to about 150 m, at which point the light intensity drops exponentially. As the shower core moves further from the telescope, the

elliptical images become more elongated along the line from the telescope to the shower core, and the amount of light in each image pixel decreases (see Section 2.1.2.3). The overall size of the image decreases due to the drop in intensity as the impact distance increases. Therefore, by choosing only telescopes in the energy reconstruction with a large impact distance, heavily saturated images can be avoided in high energy events. This chapter provides the methods and results of an analysis to remove saturated images and obtain the energy reconstruction bias due to pixel broadening and saturation in the low gain, which in turn provides a bound on systematic bias due to low gain channels on VERITAS spectra.

The analysis was applied to both V5 and V6 epochs, corresponding to the time before and after the PMT upgrade in the cameras, respectively.

4.1 Simulations and Methods

To investigate image saturation, Monte Carlo simulations were run with CORSIKA and GrISUdet, both with and without the low-gain channels active. These simulation packages are described in Chapter 3. Turning off the low gain switch caused all pixels to saturate at a size of 250 dc. These simulations were then compared to simulations with the low gain switch active, to determine at which energy and impact distances a significant loss of light and corresponding decrease in size occurred.

Simulations were run from 30 GeV to 30 TeV for the V5 epoch and winter atmosphere, with additional mono-energetic simulations generated at 800 GeV, 1 TeV, 3 TeV, 5 TeV, and 10 TeV. The showers were simulated at a zenith angle of 20°. The amount of light reaching the detector from an air shower decreases with increasing zenith angle, due to increased travel distance through the atmosphere at large zenith angles. Therefore, a high elevation was chosen to ensure a high number of bright showers. The simulated source position was placed at an offset 0.5° from the center of the camera, consistent with typical VERITAS observations. The standard analysis package of VERITAS as described in Chapter 3 was used to reconstruct the simulated events, using standard VERITAS lookup tables

processed from simulations generated in October 2012 with VEGAS v2.5.0 in the energy reconstruction.

Turning off the low gain switch produces the worst case scenario where all light is lost once the high gain saturates. As seen in Figure 4.1, the size of mono-energetic simulations without low gain drops below the size of reconstructed showers with the low gain switch enabled above a size of about 10^4 dc for events falling within 150 m of a telescope, corresponding to the bright core region described in Chapter 2.1.2.3. Therefore, a cut was chosen based on this size and impact distance, to remove telescopes for which low gain significantly effects the overall brightness of the image from the energy reconstruction.

4.1.1 Size and Core Location

The average size of events at several energies is shown in Figure 4.1. The solid circles correspond to images simulated with the low gain switch turned on and a low gain ratio of 5, while the open circles correspond to images simulated with the low gain switch turned off. Therefore, the size at which the dotted and solid lines diverge indicates the size and impact distance region at which significant light is contained in low gain channels. From Figure 4.1, it can be seen that the low gain pixels have little affect on images with size below about 10^4 dc, corresponding to energies of 1–2 TeV. At impact distances beyond 150 m from the shower core, the low gain channels again have little impact on the overall image size up to 30 TeV.

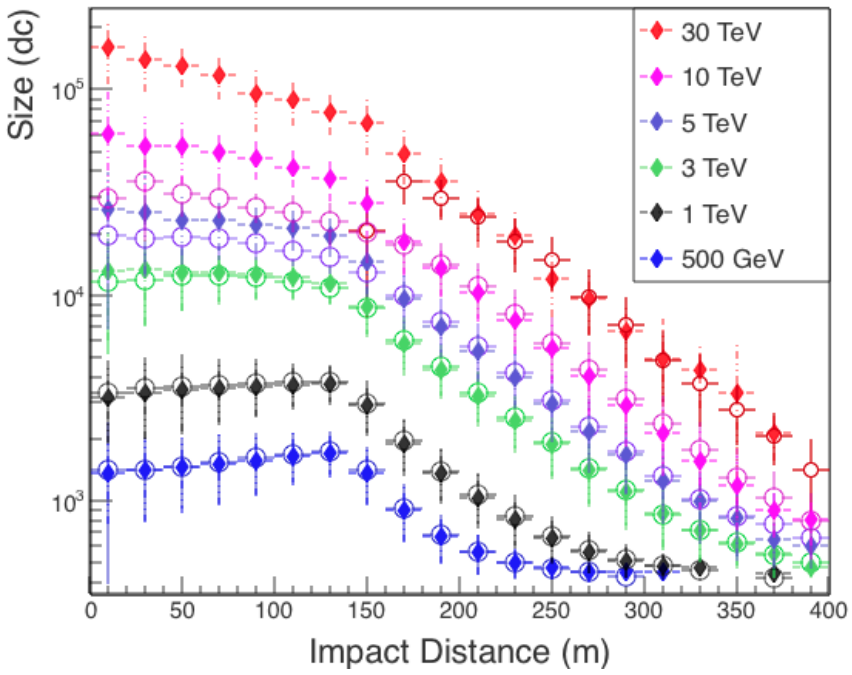

Figure 4.1 Image size as a function of impact distance impact distance for select energies above 500 GeV. Open circles show effect of removing low gain switch and allowing image pixels to saturate at 250 dc at each energy.

Removing telescopes from analysis if they fall within 150 meters of the shower core at high energies only provides useful information about the low gain bias if a significant percentage of events produce images at large core distance. The majority of gamma-ray sources produce spectra that decrease approximately as a power law in energy. Therefore, it is necessary to retain a high fraction of events at high energies in order to precisely quantify the systematic bias from low gain channels on a source spectrum. Figure 4.2 displays the impact distances of the furthest telescope participating in events at 1, 3, 5, and 10 TeV. From this plot, it can be seen that about 80% of multi-TeV events are recovered by selecting only events for which at least one telescope has an impact distance of greater than 150 m,

at energies above 1 TeV. Nearly 100% of events at sub-TeV energies have size below 10^4 dc for all telescopes, and thus are retained in the analysis.

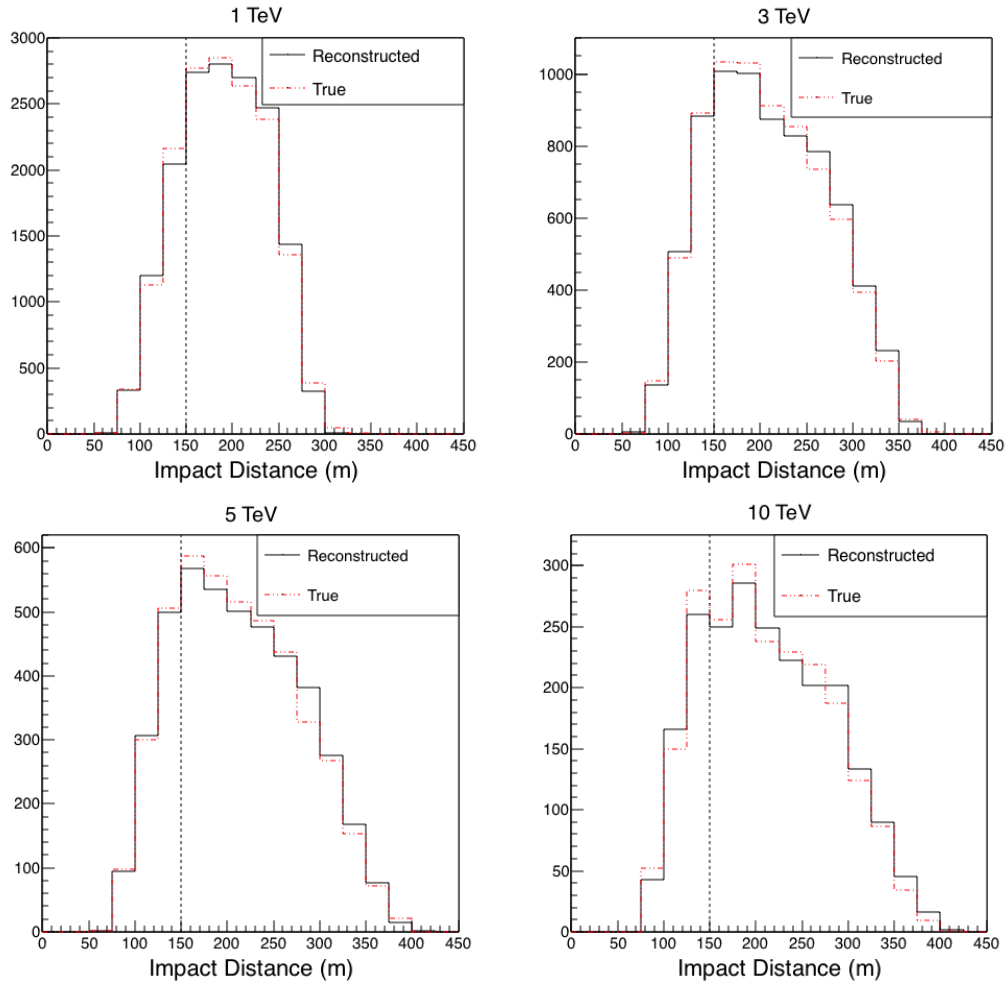

Figure 4.2 Plots showing the impact distance of the furthest telescope that participated in the event at 1, 3, 5, and 10TeV.

Direction and core reconstruction are described in Chapter 3. The following paragraphs show that the quantities are not affected by saturated images. For all energies across the VERITAS energy range, the impact distance reconstruction is excellent with a resolution of 10–15% on the core reconstruction, regardless of saturation, out to about 300–350 m. Figure A.2 shows the comparison between core reconstruction for simulated events

both with and without the low gain switch enabled. The core reconstruction is largely unaffected by saturation levels within the image. Appendix A shows the resolution of the core reconstruction for select energy bins above 1 TeV.

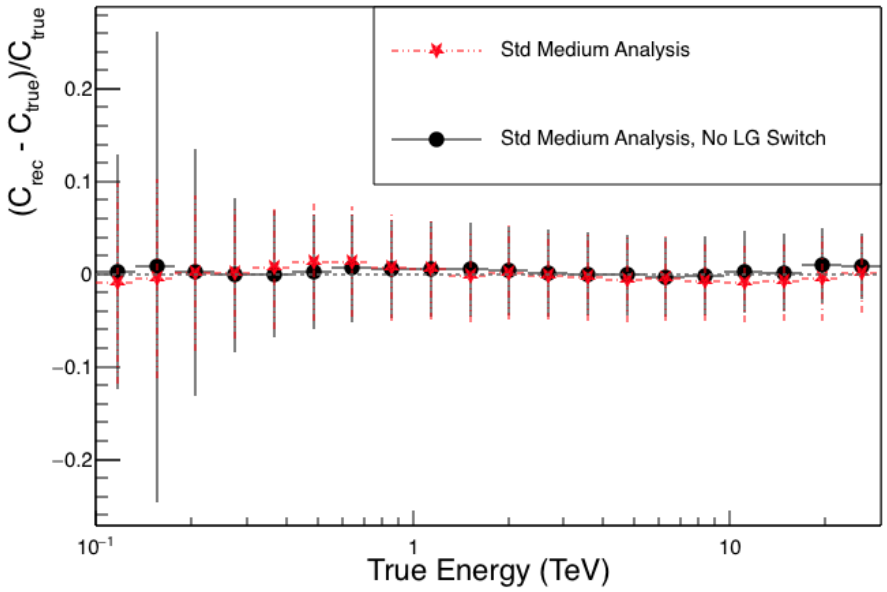

Figure 4.3 The bias in the core location reconstruction for gamma-ray events arriving from 20° zenith angle in the V5 epoch, for events with and without the low gain switch enabled.

Because the low gain channels have no significant impact on core reconstruction, all telescopes can be used to find core distance, and therefore impact distance, regardless of saturation. Impact distance reconstruction, a quantity calculated for each telescope after the core location is reconstructed, is also excellent out to about 350 m in every telescope. Figure 4.4 shows the reconstructed impact distance plotted against the true impact distance for each telescope, and fit with a linear function with a slope initialized at 1 and intercept at 0 m. Each plot was well fit by the linear function, with a slope near 1 and intercept within a few meters of 0 m.

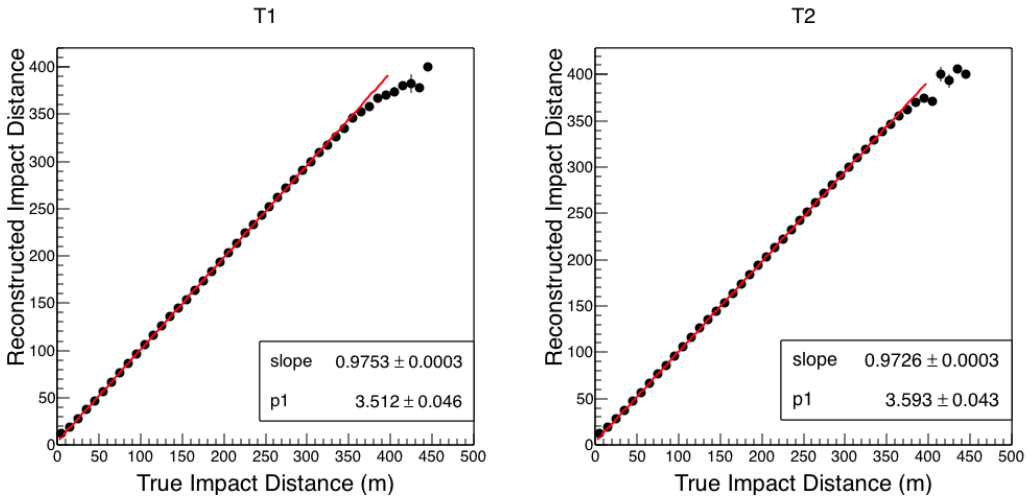

(a) T1

(b) T2

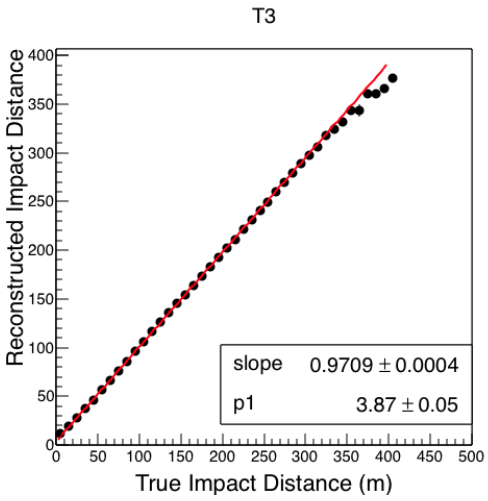

(c) T3

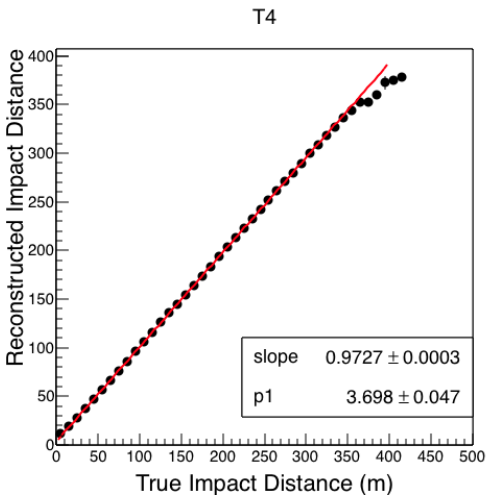

(d) T4

Figure 4.4 Reconstructed impact distance plotted against true impact distance. Showers are captured and well reconstructed out to impact distances of about 350 m for all telescopes.

Therefore, removing telescopes that fall within 150 m of the core of multi-TeV showers from the energy reconstruction leaves a wide range of impact distances over which showers are still triggered and reconstructed by the detector.

4.1.2 Effects of Saturation on Cut Parameters

The standard analysis cuts include both telescope level cuts and event level cuts (see Chapter 3 for a detailed explanation of cuts). In this section, I examine the effect of saturation on standard analysis cuts. The cuts on size and number of phototubes remove dim, low energy events from analysis. Due to the fact that these dim events do not cause saturation in the FADCs, those cuts are not considered in this section.

The distance cut removes images that leak off the edges of the camera. Because the purpose of the new cuts being implemented in this chapter is to avoid heavily saturated images by looking only at images far from the center of the light pool. Appendix A shows the image distance from the center of the camera of distant events in V5.

Event level cuts are applied to parameters averaged over all telescopes participating in the image. Figure 4.5 shows the MSW and MSL for simulations both with and without the low gain switch enabled. Because the standard analysis cut on each mean scaled parameter is applied as a box cut without regard to energy, the parameter distributions in Figure 4.5 also cover all energies. This analysis ignores the parameter referred to as "Shower Height" within the standard analysis, due to its inaccurate calculation in the standard VEGAS analysis. Shower height will be discussed in greater detail in Chapter 6. The amount of saturation in an image does not produce a significant effect on the distribution of mean scaled parameters. Therefore, these cuts are not altered, and all telescopes are retained in the calculation of these event level cut parameters, regardless of saturation level.

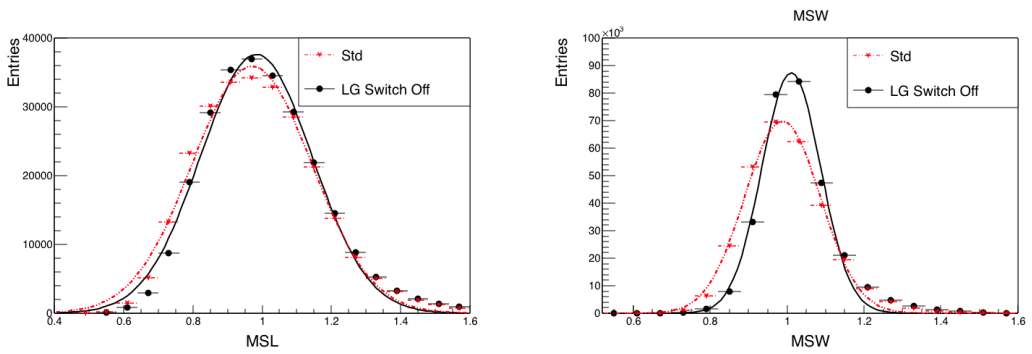

(a) MSL (b) MSW

Figure 4.5 Comparison of MSPs with and without the low gain switch turned on in V5.

Each histogram in Figure 4.5 was fit to a gaussian. The fit parameters are shown in Table 4.1. The events with the low gain switch turned off are shifted to slightly higher mean scaled widths and lengths than events with the low gain switch on.

Table 4.1 Gaussian fit parameters for simulated MSL and MSW, with and without the low gain switch in V5.

V5	Mean_{Std}	$\text{Sigma}_{\text{Std}}$	$\text{Mean}_{\text{LGOff}}$	$\text{Sigma}_{\text{LGOff}}$
MSL	0.97	0.172	0.98	0.161
MSW	0.99	0.10	1.01	0.08

The cut on θ^2 is applied in the final stage during the spectral reconstruction. In Figure 4.6(a), the distribution of events with and without the low gain switch enabled are compared for θ^2. This parameter is not significantly affected by saturation. Figure 4.6(b) shows theta squared for all images compared to all images at a core distance greater than 150 m. The distribution of theta squared does broaden very slightly for very distant showers. However, because saturation does not affect the calculation of theta squared, all images can be used in this calculation. Only events where all telescopes fall within 150 m of the shower core are cut fully from the analysis. Additionally, the broadening in θ^2 for distant

showers in very minimal. Therefore, the cut does not need to be altered for the analysis presented in this chapter.

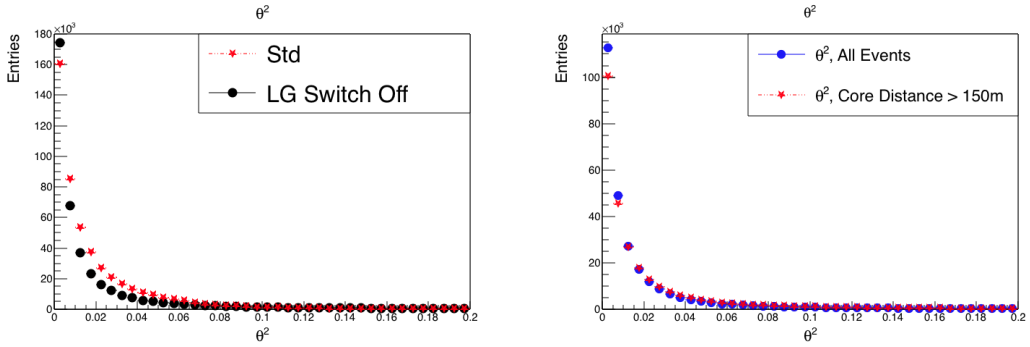

(a) θ^2 Without Low Gain

(b) θ^2 at Large Distances

Figure 4.6 Comparison of V5 θ^2 with and without the low gain switch turned on in (a), and θ^2 for events at large core distances in (b).

4.1.3 SAM Cuts

As Figure 4.1 shows, the size of the image and the distance of the telescope from the shower core can be used to remove images with a significant number of pixels in low gain from the energy reconstruction. As Section 4.1.2 shows, deactivating the low gain switch has negligible effect on existing event level standard analysis cuts. Therefore an extra quality cut based on size and impact distance is added for each telescope only during energy reconstruction, in a new energy reconstruction method called the Saturation Avoidance Method (SAM). For any telescope with a size greater than 10^4 dc, only telescopes that are more than 150 m from the shower core in the mirror plane are used in the energy reconstruction. A weighted average is performed over the reconstructed energy for each telescope that passes this quality cut to obtain the reconstructed gamma-ray energy, where the $\log_{10}$(size) is used as the weight. The decision tree for removing highly saturated telescopes from the energy reconstruction is shown in the flowchart in Figure 4.7. For the more general flowchart of

the VEGAS analysis package, see Figure 3.2 in Chapter 3. The SAM energy reconstruction is applied in stage 4 of VEGAS, during the energy reconstruction.

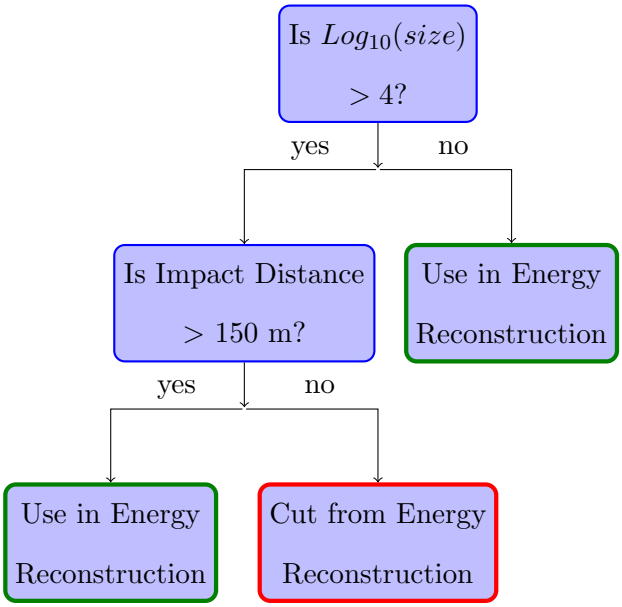

Figure 4.7 Flowchart of telescope level cuts applied to energy reconstruction with SAM.

This extra cut leaves low energy showers largely unaffected. Approximately 20% of events are removed from Multi-TeV showers due to the SAM cuts. These are all events where the showers occurs close to the center of the array, and thus all telescopes are expected to have saturated images. Remaining events that lose one or more telescopes in the energy reconstruction lose only highly saturated telescopes. Therefore, the resulting reconstructed energy is unbiased by saturation effects.

The saturated pixels have no significant effect on the core reconstruction and other quality cuts, as shown in Sections 4.1 and 4.2. Therefore, all telescopes that pass the initial telescope level quality cuts, as described in Chapter 3, are still used to calculate core location, width, length, and θ^2. Only during energy reconstruction are the saturated telescopes removed from consideration. The event-level cuts in stage 5 are not altered.

4.2 Results of SAM Cuts in Simulations

Here follows the results of the application of the SAM cuts to simulations. All parameters were rechecked after applying the SAM energy reconstruction, to ensure that no unexpected biases occurred in cut parameters.

Applying the SAM energy reconstruction to simulations retains a bias over data due to the fact that the simulated pulses are not matched to pulses from a real PMT. Therefore an analysis performed on simulations should produce a much more accurate energy reconstruction of low gain pixels than an analysis of data. For this reason, the energy bias shown in simulations is expected to be a lower bound on the energy bias in data analysis. Section 4.3 shows the results of the SAM energy reconstruction applied to data from the Crab Nebula.

4.2.1 Standard Cuts

Although some events are lost in the SAM energy reconstruction, the effect on mean scaled parameters is statistically insignificant. Table A.1 shows the mean values of the mean scaled parameters and their RMS deviation for the V5 epoch, while Table A.2 shows the same values for the V6 epoch.

Table 4.2 MSL and MSW show no significant variation from the mean and RMS values with the SAM energy reconstruction in V5.

V5	$\text{Mean}_{\text{standard}}$	$\text{RMS}_{\text{standard}}$	Mean_{SAM}	RMS_{SAM}
MSL	0.989	0.17	0.996	0.17
MSW	1.001	0.11	1.003	0.11

Table 4.3 MSL and MSW show no significant variation from the mean and RMS values with the SAM energy reconstruction in V6.

V6	$\text{Mean}_{\text{standard}}$	$\text{RMS}_{\text{standard}}$	Mean_{SAM}	RMS_{SAM}
MSL	1.02	0.17	1.01	0.17
MSW	1.01	0.086	1.00	0.085

Further details on the effect of the SAM energy reconstruction on standard analysis parameters can be found in Appendix A.

4.2.2 Energy Bias

At the multi-TeV end of the VERITAS energy range (above a few TeV), the reconstructed energy bias becomes negative, as seen in Figure 3.10. One source of bias in this regime is saturation of the low gain FADC channels. As the energy of the primary gamma ray in an air showers increases, the resulting images grow bright enough to cause a large amount of saturation in image pixels, especially near the shower core. Because the SAM cuts remove highly saturated images from energy reconstruction, the energy bias is expected to improve in simulations with SAM cuts applied over the standard energy reconstruction that includes such saturated images. The resolution may also be expected to broaden slightly. Any event where the shower core falls within 150 m of all image telescopes leaves no telescope far enough from the shower core to produce an unbiased image. These events are removed from the analysis, leading to lower statistics that broadens the energy resolution slightly.

In spite of the expectation of a better energy resolution when saturated telescopes are removed from reconstruction, initial studies on simulations for the V5 epoch indicated a worse bias at high energies for the SAM reconstruction, as seen in Figure 4.8.

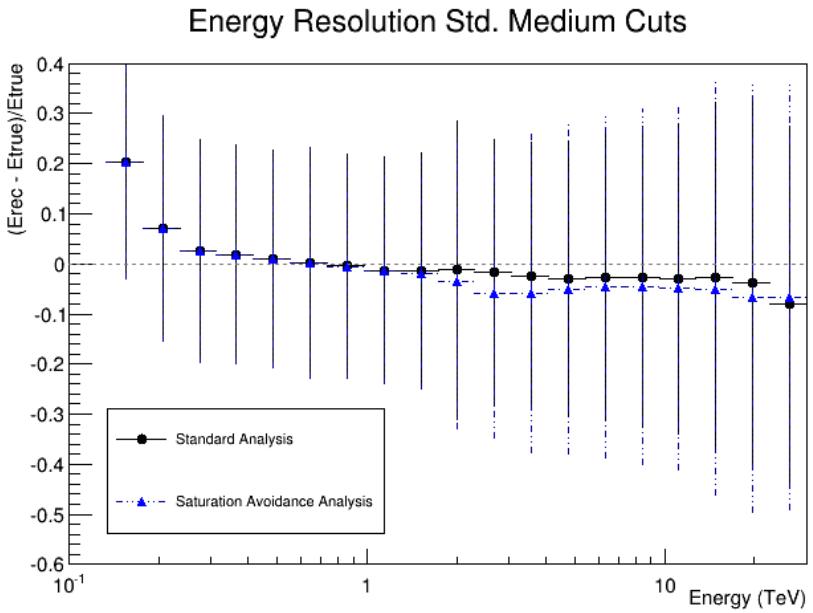

Figure 4.8 Energy bias for the SAM energy reconstruction, compared to the energy bias of the same simulations passed through a standard analysis, for V5 simulations.

The solution was found by dividing the simulations into subsets based on the number of telescopes used in the energy reconstruction. Several distinct classes of events can then be seen in Figure 4.9. The events with only one telescope used in the energy reconstruction are likely dimmer events that only trigger a few telescopes closer to the center of the array. These events have a higher shower maximum than the average shower for their energy and are thus unusually dim. This relation between energy and shower height will be discussed further in Chapter 6. Therefore, these events show a large negative bias in reconstructed energy.

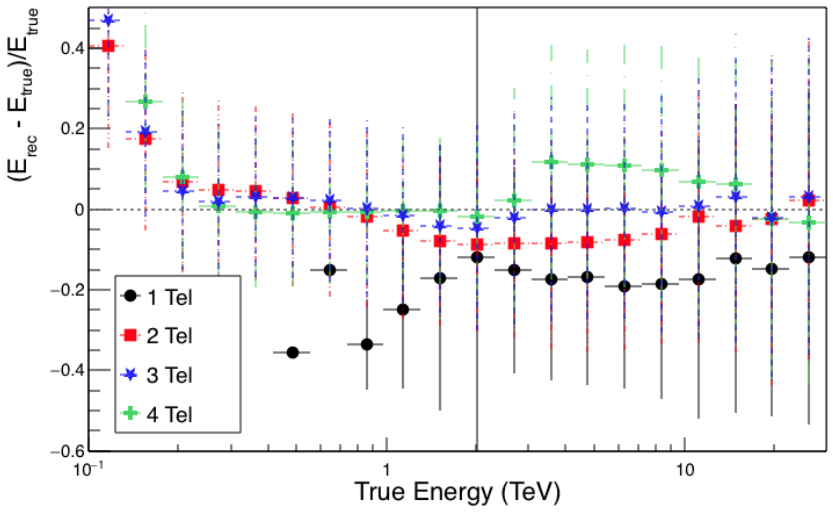

Figure 4.9 Energy bias for the SAM energy reconstruction for number of telescopes used for energy reconstruction in the SAM analysis, for V5 simulations.

Removing the events with one telescope in the energy reconstruction improves the energy resolution over the standard analysis, as shown in figure 4.10. Table 4.4 provides the percentage of events that have a given number of telescopes in the energy reconstruction. The total number of events reconstructed by the SAM analysis is about 90% of events reconstructed for the standard analysis, for the same simulation file, for simulations at 20 degree zenith angle. The additional cut to remove events in which only 1 telescope passes the SAM reconstruction causes increased event loss at the highest energies. Overall, this cut removes only 2% of total events in the SAM analysis. However, the SAM Analysis only kicks in above approximately 1 TeV. At energies above a few TeV, 20–30% of events have only 1 telescope that pass SAM Analysis cuts. Therefore, 40–50% of simulated events of events in the standard analysis do not pass SAM cuts with at least 2 telescopes above about 3.5 TeV. The loss of statistics is offset by the improved accuracy of the energy reconstruction for remaining events. Therefore, the loss in statistics and corresponding loss in energy resolution is counter-balanced by the improvement in overall bias.

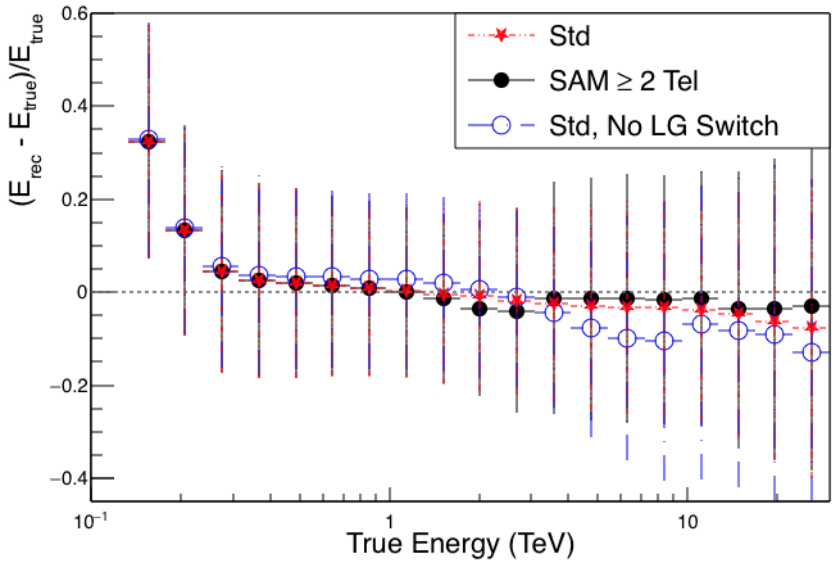

Figure 4.10 Energy bias for the SAM energy reconstruction compared to the standard analysis in V5. Simulations generated with no low gain switch shown for comparison in the open blue circles. Bias in data is expected to fall between the blue and red curves.

Table 4.4 Percent of events passing the SAM energy reconstruction in logarithmically spaced energy bins between 1–30 TeV, at 20° zenith in the V5 epoch. Energy values are given as the center of the bin.

Energy (TeV)	1.15	1.5	2	2.7	3.5	4.75	6.3	8.4	14.85	19.75	26.25
% Events SAM	99.6%	96%	80%	64%	61%	60%	59%	57%	52%	46%	40%

The energy bias was also tested with a decreased size cut of 8,000 dc. Figure 4.11 shows the effect of a size cut of 8,000 dc compared to a cut of 10,000 dc. The differences in the energy bias of the two size cuts is minimal.

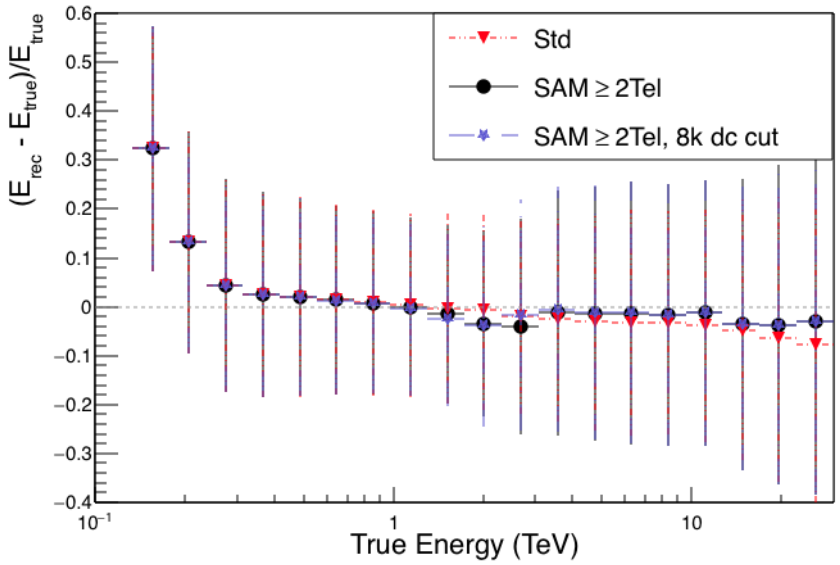

Figure 4.11 Energy bias for the SAM energy reconstruction with two different size cuts applied to V5 simulations.

Figure 4.12 shows the energy bias of events with 1, 2, 3, and 4 telescopes participating in a SAM energy reconstruction with a size cut of 8,000 dc, applied to V5 simulations.

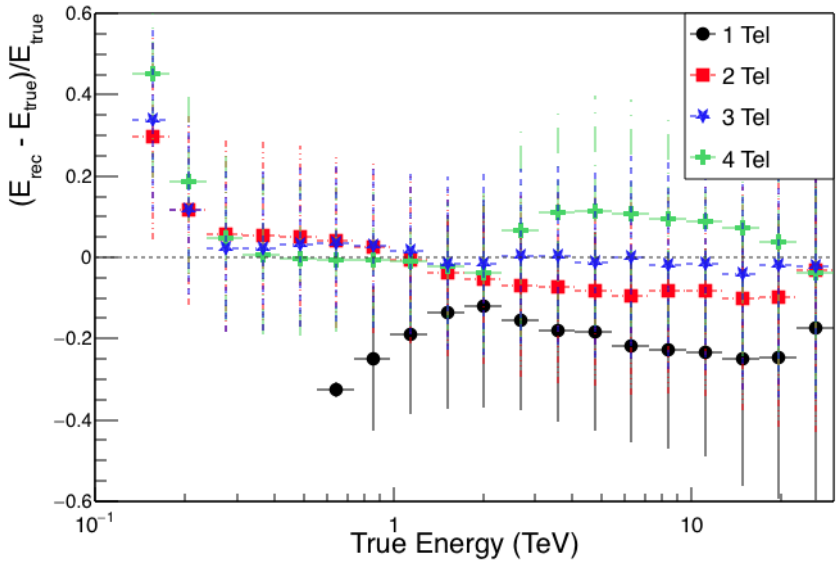

Figure 4.12 Energy bias for the SAM energy reconstruction for number of telescopes used in energy reconstruction in the SAM analysis, in V5 simulations.

A stricter size cut removes a higher percentage of events from analysis, for negligible gain in energy bias. Approximately 1.5% more events are cut with the stricter cut on size in the SAM analysis. Therefore, a size cut of 10,000 dc was retained for the nominal SAM analysis, with only events that had 2, 3, or 4 telescopes participating in the energy reconstruction retained.

Due to the faster timing of the upgraded PMTs in the V6 epoch, they are expected to peak more sharply and thus enter the low gain mode more quickly. Therefore, saturation effects due to the low gain in V6 should also occur more quickly than in V5. This holds true in simulations. While at least 80% of events are reconstructed by the SAM Analysis in V5 up to about 2 TeV, the percentage of events reconstructed by the SAM analysis compared to the standard analysis in V6 drops below 80% by 1.5 TeV, for the same SAM analysis cut of 10^4 dc for telescopes within 150 m of the shower core.

The removal of highly saturated images in the SAM energy reconstruction, as well as events where only one telescope passes the SAM cuts, shows significant improvement in the overall bias at energies above a few TeV. Figure 4.13 shows the energy bias of the standard analysis compared to the energy bias of the same simulations run with the SAM energy reconstruction, for the V6 epoch. Removing events with only a single telescope contributing to the energy reconstruction also accrues a loss of only about 2% of total events in the V6 epoch. About 90% of events are kept from a standard analysis, between 100 GeV and 30 TeV. However, because the SAM Analysis turns on above about 1 TeV, the percentage of events with only 1 telescope used in SAM Analysis energy reconstruction is about 20% of total events passing SAM Analysis cuts. Therefore, about 40% of events in the standard analysis do not pass SAM cuts with at least 2 telescopes above about 1.5 TeV. The remaining events have an excellent energy bias, however, of only a few percent bias out to 30 TeV. The percentage of events retained in the SAM energy reconstruction between 1–30 TeV is given in Table 4.5. The percentages are compared to the number of events in the standard energy reconstruction at logarithmically spaced bins in energy, obtained from V6 simulations at 20 degree zenith.

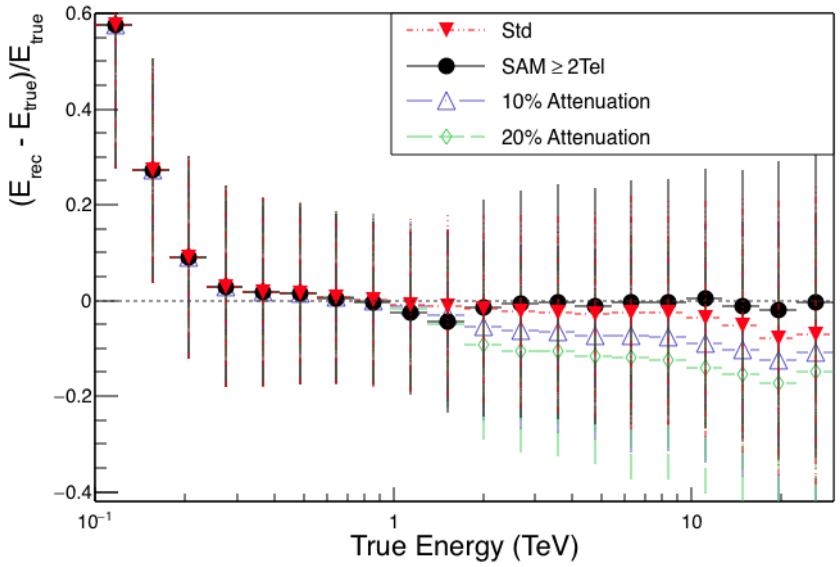

Figure 4.13 Energy bias for the SAM energy reconstruction compared to the standard analysis, with and without artificially added saturation in the V6 epoch.

Table 4.5 Percent of events passing the SAM energy reconstruction in logarithmically spaced energy bins between 1–30 TeV, at 20° zenith in the V6 epoch. Energy values are given as the center of the bin.

Energy (TeV)	1.15	1.5	2	2.7	3.5	4.75	6.3	8.4	14.85	19.75	26.25
% Events SAM	80%	62%	60%	60%	61%	61%	62%	61%	62%	63%	65%

The SAM Analysis was also tested in V6 with modifications to the size cut on images allowed in the energy reconstruction. Figure 4.14 shows the results of increasing the size cut to 15 thousand digital counts, while Figure 4.15 shows the results of imposing a stricter size cut of 8,000 digital counts.

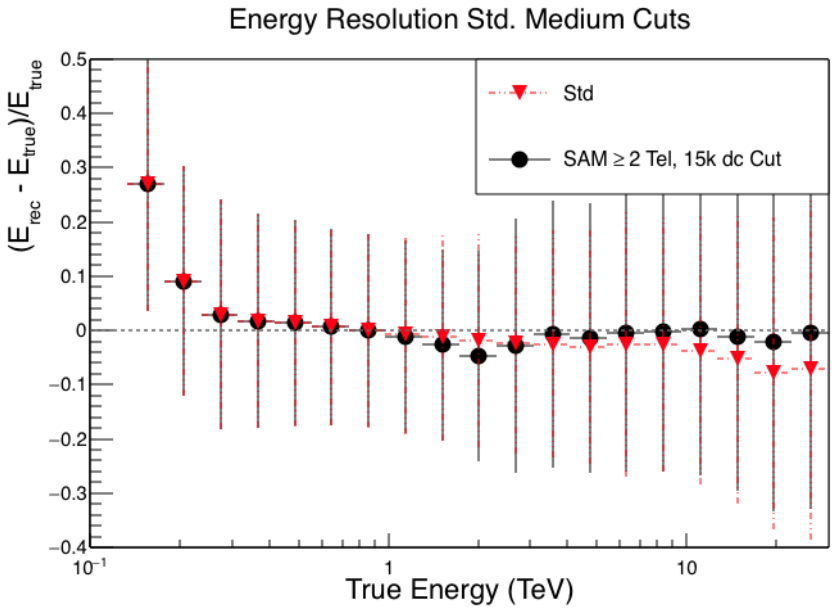

Figure 4.14 Energy bias for the SAM energy reconstruction compared to the standard analysis with and without artificially added saturation in the V6 epoch.

Increasing the size cut in the SAM analysis increases the energy threshold at which the SAM analysis turns on. The energy bias is comparable to the bias produced with the size cut set to the nominal size of 10^4 digital counts, with an increase in the bias where the analysis turns on.

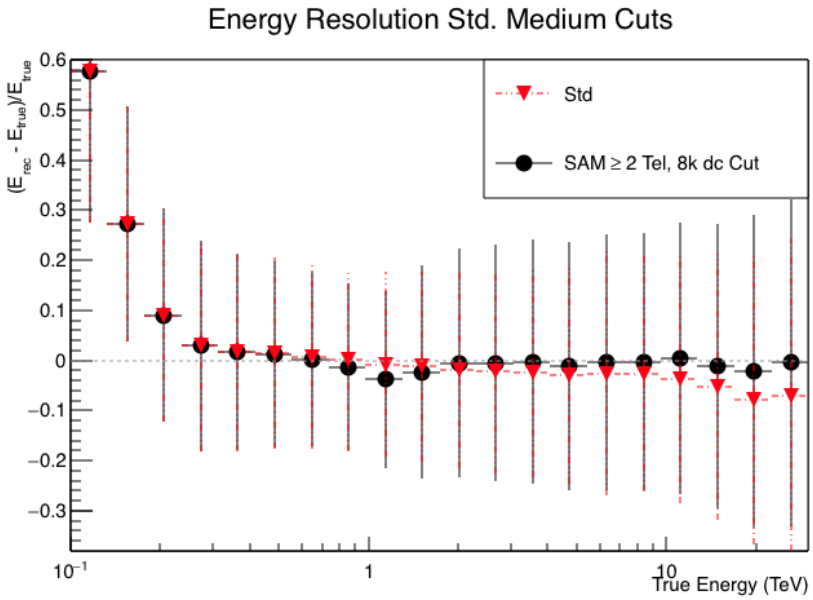

Figure 4.15 Energy bias for the SAM energy reconstruction compared to the standard analysis with and without artificially added saturation in the V6 epoch.

Use of a more strict size cut of 8 thousand digital counts brings the threshold for the SAM analysis down just below 1 TeV. The bias is comparable to that produced with the 10^4 digital counts cut in the nominal SAM analysis. The number of digital counts at which the low gain switch turns on is very consistent between V5 and V6, as shown in the final section of this chapter; the size at which the low gain begins to significantly affect image brightness is also comparable to the size determined in V5. Therefore, a size cut of 10^4 digital counts is appropriate for use in both V5 and V6.

In the next section, results are shown for the validation of the SAM analysis on data from the Crab Pulsar Wind Nebula (PWN), a bright source that has been well studied at VHE energies. The high statistics and wealth of data from other instruments for comparison makes the Crab Nebula an excellent source for validation of new analysis methods on data. In the SAM analysis in particular, validation on data is an essential cross-check to the results on Monte Carlo simulations. Due to the differences between simulated low gain

pulses and true low gain pulses, all validation up to this point done on simulations compares reconstructed parameters to ideal, known parameters. Applying the SAM reconstruction on data allows for evaluation of the impact from saturation effects of the FADC system in the standard analysis at multi-TeV energies on data from VHE sources of scientific interest.

4.3 Validation on Data From the Crab Nebula

The Crab Nebula was the first source discovered at TeV energies [55]. Emission from the Crab is well studied by IACTs, including VERITAS. It is one of the brightest sources in the gamma-ray sky, with no detected variability in the VERITAS energy range [4]. As such, it serves as a standard candle to validate the SAM energy reconstruction cuts on data. Reconstructing real data with both the standard and the SAM energy reconstruction allows for a check of the systematic effect of saturation on the reconstructed spectrum.

Because the shape and relative gain of PMT pulses in low gain channels is modeled differently in simulations than they occur in data, it is necessary to cross-check the results obtained on simulations with real data. The standard analysis reconstructs energies from saturated images, and the SAM energy reconstruction removes those images. Therefore, applying the SAM analysis on both data and simulations provides a more accurate picture of reconstructed energy bias introduced from low gain channels than a validation on simulations alone.

The Crab data validation was performed for data from both the V5 epoch of VERITAS and the V6 epoch, corresponding respectively to the time before and after the 2012 camera upgrade in which all of the PMTs were replaced with new PMTs with faster timing and a sharper peak. Effective areas were generated for each the standard and SAM analyses, for zenith angles of 0–30 degrees and wobble offset of half degree from the center of the FoV. Figure 4.16 shows the difference in V6 effective areas between a standard analysis and a SAM analysis, for simulations at zenith angles of 0°, 20°, and 30°.

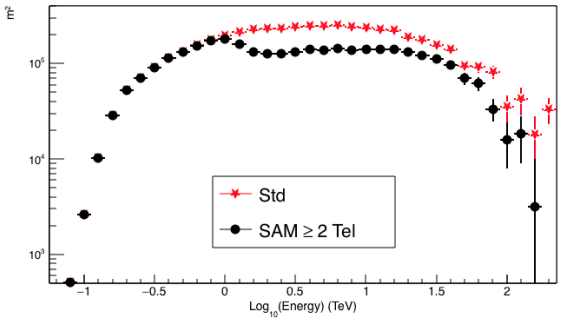

(a) 0 deg

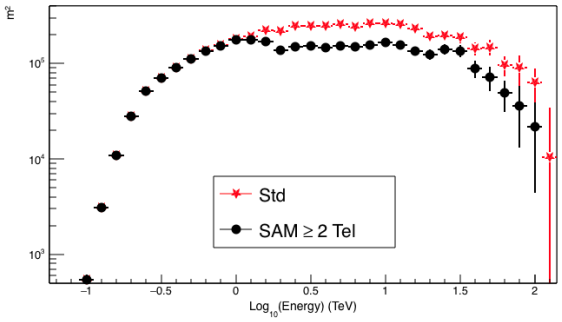

(b) 20 deg

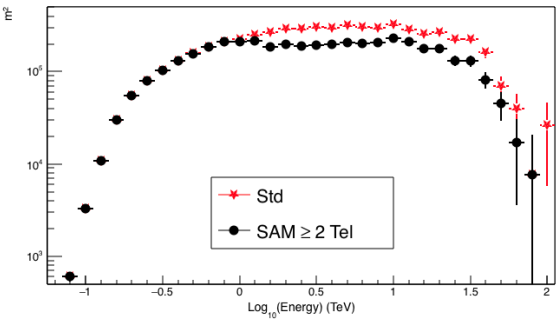

(c) 30 deg

Figure 4.16 The difference in effective area between the Standard analysis, shown in red, and the SAM energy reconstruction, shown in black, for 0, 20, and 30 degree zenith angles in the V6 epoch.

The statistics are lower in the SAM analysis than in the standard due to the additional size and impact distance cut applied in the SAM analysis. This loss of statistics shows up in the decrease in the effective area of the SAM analysis for each zenith angle.

4.3.1 V5 Crab Analysis

The V5 Crab data was analyzed with 187 20-minute data runs, corresponding to approximately 55 hours of useable data after initial quality cuts. In order to minimize competing sources of bias, only runs with A-weather, zenith angle $< 25°$, and all four telescopes par-

ticipating were allowed. Runs were additionally chosen to have ended normally and marked "good run" by the next day quality monitors.

The results of the Crab analysis comparing the standard analysis with medium cuts to the SAM analysis with medium cuts are shown in Figure 4.17. The spectra measured from each energy reconstruction was fit with a log-parabolic function of the form

$$\frac{\mathrm{d}N}{\mathrm{d}E} = N_0 \left(\frac{E}{E_0} \right)^{-\Gamma - \beta log_{10}(E/E_0)} \tag{4.1}$$

where β describes the amount of *curvature* the spectrum shows. The fit probability and fit values to the log-parabolic fit for each reconstructed spectrum are shown in Table A.3.

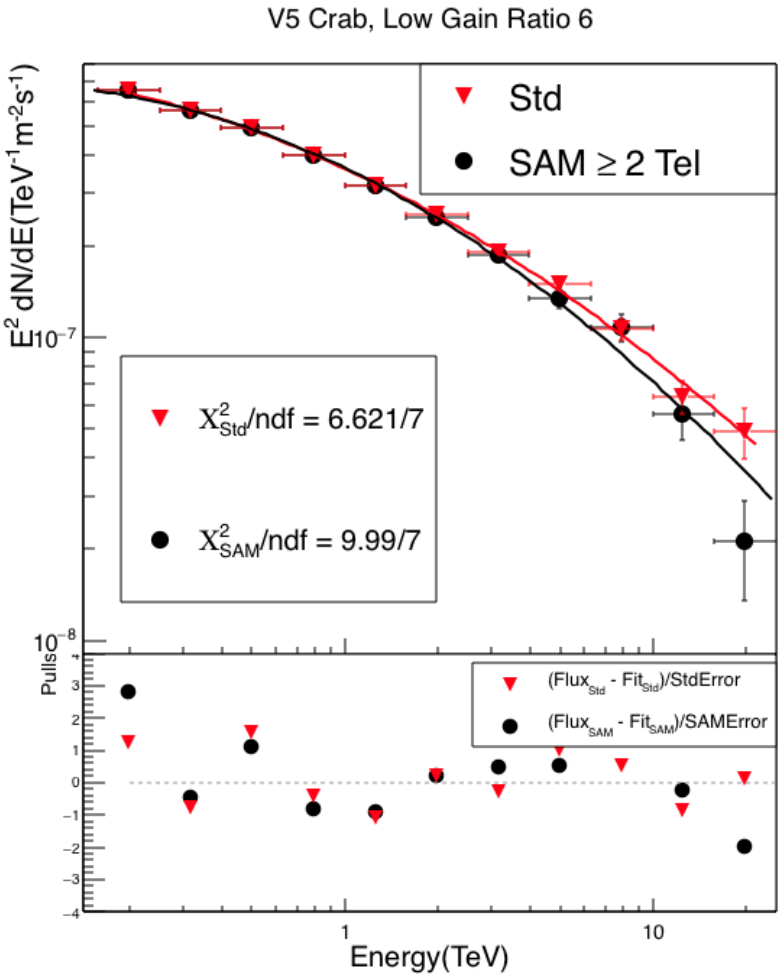

Figure 4.17 Data from the Crab Nebula, taken at high elevation during winter months in the V5 epoch. The spectra are compared for a standard analysis and a SAM energy reconstruction.

Table 4.6 Fit parameters for spectra obtained from the Crab Nebula, compared for a standard analysis and a SAM energy reconstruction, during the V5 epoch.

	Index α	Curvature β	Norm	χ^2/ndf	σ
SAM	2.49±0.01	0.0938 ± 0.01	$3.63 \cdot 10^{-7}$	9.99/7	292σ
Std	2.47±0.01	0.0700 ± 0.01	$3.62 \cdot 10^{-7}$	6.62/7	297σ

The spectra obtained from the two analysis methods produce an unexpected result. The SAM analysis removes low gain channels and softens the spectrum. Low gain channels that saturate have lost light. Therefore, using only unsaturated images produces a better measure of true shower brightness by retaining more light from the shower. A spectrum which retains more light in high energy showers will reconstruct more high energy events, which hardens the spectrum. The observed softening of the spectrum with low gain channels removed, however, implies an incorrectly applied value of the low gain ratio in V5 data. This will be discussed further in Section 5.1.

4.3.2 V6 Crab Analysis

The validation for the V6 epoch, corresponding to the time period after the PMT upgrade, contains 112 runs in a mix of 20-minute and 30-minute data runs, for a total of about 46 hours of useable data after initial quality cuts. As in V5, only runs with A-weather, zenith angle $< 25°$, and all four telescopes participating were selected. Additionally, the runs had to be marked "good run" in the next day quality monitoring.

The results of the Crab analysis are shown in Figure 4.18. The best-fit values from log-parabolic fits are summarized in Table 4.7.

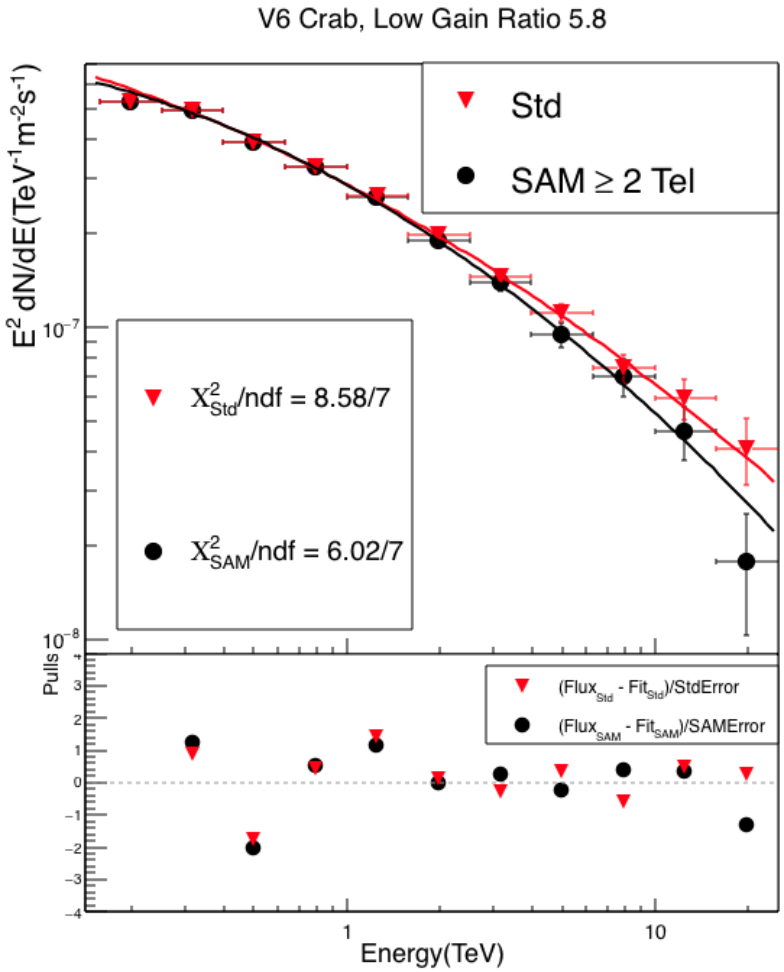

Figure 4.18 Data from the Crab Nebula, taken at high elevation during winter months in the V6 epoch. The spectra are compared for a standard analysis and a SAM energy reconstruction. Pulls are shown beneath.

Table 4.7 Fit parameters for spectra obtained from the Crab Nebula, compared for a standard analysis and a SAM energy reconstruction, during the V6 epoch.

	Index α	Curvature β	Norm	χ^2/ndf	σ
SAM	2.55 ± 0.01	0.0785 ± 0.012	$2.87 \cdot 10^{-7}$	6.02/7	263 σ
Std	2.52 ± 0.01	0.052 ± 0.011	$2.88 \cdot 10^{-7}$	8.58/7	272 σ

As in the V5 analysis, the SAM energy reconstruction produces a softer spectrum than the standard analysis. This result is unexpected for the case where the primary systematic bias from low gain arises due to saturation of the low gain pixels and light leaking out of the readout window in data, both effects which would artificially soften a multi-TeV spectrum. The softening of the V6 spectrum with a SAM analysis that removes images with a large amount of low gain pixels indicates an incorrect value of the high-to-low gain ratio is applied during analysis.

The following chapter provides a method for determining the accurate low gain ratio for VERITAS analysis, and provides a cross-check with the SAM analysis.

CHAPTER 5. THE VERITAS LOW GAIN RATIO

5.1 The VERITAS Low Gain Ratio

As discussed in Chapter 3, the high-to-low gain switch in the VERITAS FADCs were built with a high-to-low gain ratio of 6. Assuming perfect implementation of the electronics and no drift in the gain factor with time, data from both the V5 and V6 epochs should therefore produce low gain pulses with a factor of 6x less charge produced per p.e. than high gain pulses. In addition, all telescopes should produce equivalently sized pulses at the same gamma-ray energy and impact distance.

A standard VEGAS analysis applies a low gain ratio of 6 in the V5 epoch, as expected from the FADC electronics. However, early measurements of V6 pulses already indicated differences in the high-to-low gain ratio; therefore, a standard analysis of V6 data applies a low gain ratio of 5.8 to data. The results of the V6 SAM energy reconstruction indicate that even the value of 5.8 was too high. A high ratio results in VEGAS measuring too much light in low gain channels, which accounts for the softening of the V6 Crab spectrum as reconstructed with the SAM energy reconstruction when compared to the standard analysis. This explains the hardening of the V6 Crab spectrum as compared to the V5 Crab spectrum when analyzed with the standard energy reconstruction.

5.1.1 Data/Monte Carlo Comparisons of Image Brightness in V6

The low gain ratio affects the measured brightness of channels that have switched into low gain, which then also affects the total measured size of the image. However, due to fluctuations with impact distance and number of channels in low gain across a measured

distribution of all image sizes, the effect of an incorrectly applied low gain ratio is hard to measure from a distribution of size alone. Pixel level parameters provide a better method of evaluating the low gain ratio, and thus were used as the primary method of determining an accurate ratio in V6 data. The V6 data from the Crab Nebula SAM analysis validation was used to run data/MC comparisons of various measurements of image brightness, using data analyzed with different values of the low gain ratio.

The simulations used to produce the data/MC studies in this section were run with the CORSIKA-grISUdet simulation chain in 2012, with a low gain ratio of 5. For simulations, the size and Max1 values are properly measured so long as the simulated events are reconstructed with the same low gain ratio that was used to generate them. Therefore, new simulations were not generated with each different low gain ratio value that was tested in data. Additionally, because simulations recover all light in simulated low gain pulses up to the point of saturation in the low gain channels, the simulations act as an upper bound on the total size and pixel brightness values for data with a correctly measured value of the low gain ratio. Finally, the simulations were re-weighted from their initial power law spectral index of 2.0, to a power law spectral index of 2.5. This was done to better match the data from the Crab Nebula, which follows roughly a power law index of 2.5 to high energies. The distribution of events in the data was also scaled to match the total events in simulations, for an accurate comparison of the shape of each distribution.

Several key plots are shown in the following sections, with further supplementary plots available in Appendix A. From these plots, it is clear that the low gain ratio currently applied in VERITAS analyses is too high for the true ratio.

5.1.1.1 Max1

The most useful parameter for investigating the low gain ratio is a quantity called "Max1." Max1 refers to the total integrated charge in the brightest image pixel. This distribution shows a very clear feature at 1000 dc, right where pixels begin to enter low

gain. To demonstrate this feature, the data was run with an extremely high low gain ratio of 7, and an extremely low ratio of 4.5. These plots are shown below for T2, with the distinct transition highlighted in the blue circle.

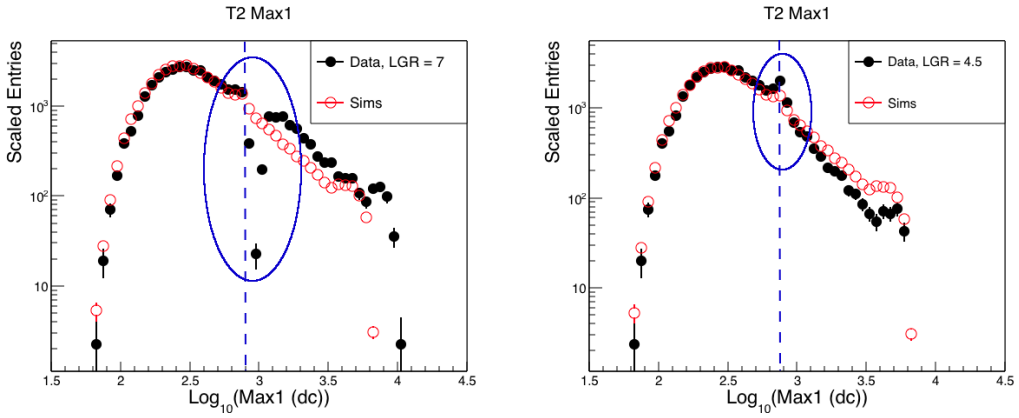

(a) Low Gain Ratio = 7

(b) Low Gain Ratio = 4.5

Figure 5.1 V6 Data/MC comparison of Max1 for data reconstructed with an extreme high low gain ratio of 7 and an extreme low ratio of 4.5.

The blue dashed line indicates the location of the low gain switch in integrated counts. The data/MC comparisons of Max1 show a clear feature arising around a value of Max1 = 700 dc, the point where integrated pixel charge saturates the high gain and flips the readout into the delayed low gain channels. In Figure 5.2, there is a clear jump in the Max1 distribution at about 700 dc for images reconstructed with a low gain ratio of 5.8. Images above 700 dc have switched into low gain, and are consistently measured above the simulated size of Max1 pixels in simulations for all four telescopes.

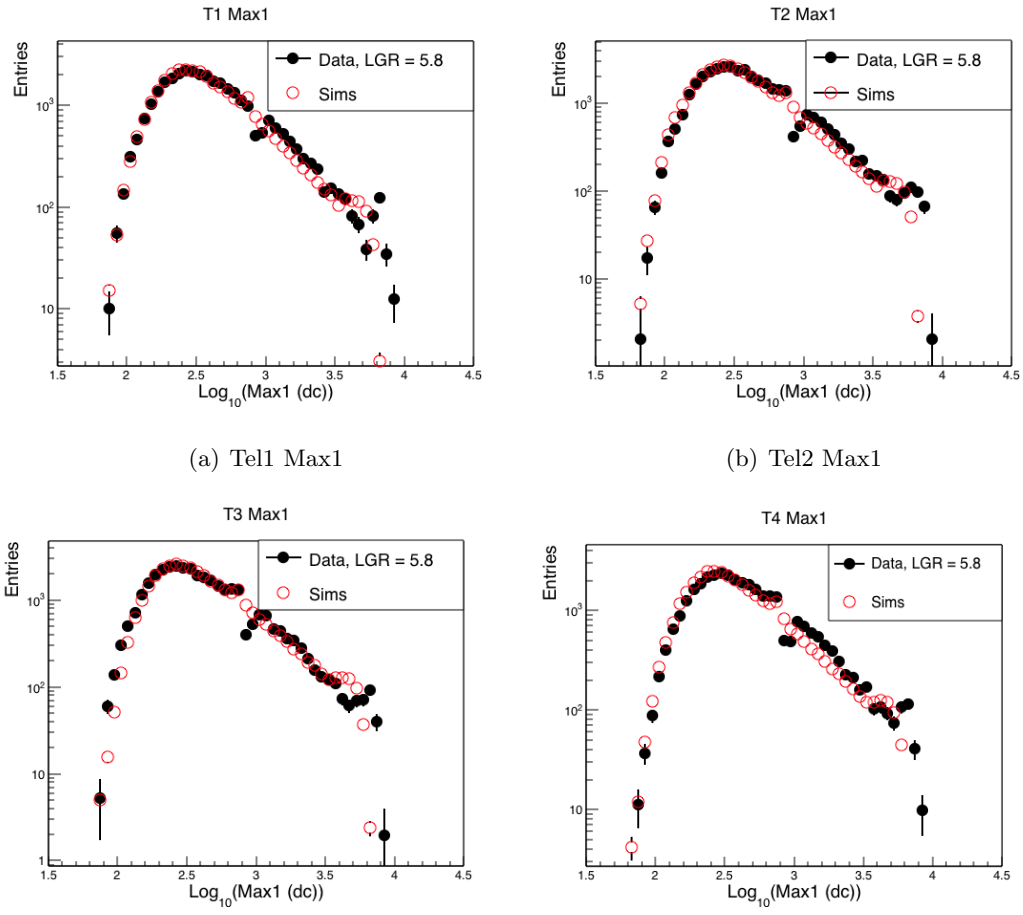

(a) Tel1 Max1

(b) Tel2 Max1

(c) Tel3 Max1

(d) Tel4 Max1

Figure 5.2 V6 Data/MC comparison of Max1 for data reconstructed with a low gain ratio of 5.8.

The jump in the Max1 distribution of data above 700 dc strongly indicates that the low gain ratio of 5.8 used in standard analyses of V6 data is too high, and therefore causing an upward bias in measured pixel size of low gain channels. Further studies were done to determine a more appropriate value of the low gain ratio. The V6 Crab Nebula data was analyzed with values of the low gain ratio equaling 5.0, 5.2, 5.3, and 5.4. All distributions are shown in Appendix A. The Max1 data/MC distributions for 5.3 are shown below as well in Figure A.9.

VEGAS applies the low gain ratio in the first two analysis stages. Therefore, in order to run data/MC comparisons with different low gain ratios, each value tested required re-analyzing the data from the raw VBF files. Due to the size and computing time requirements of running stages 1 and 2 in VEGAS, the initial testing was performed for smaller subsets of about half the V6 Crab data, rather than the full 46 hours.

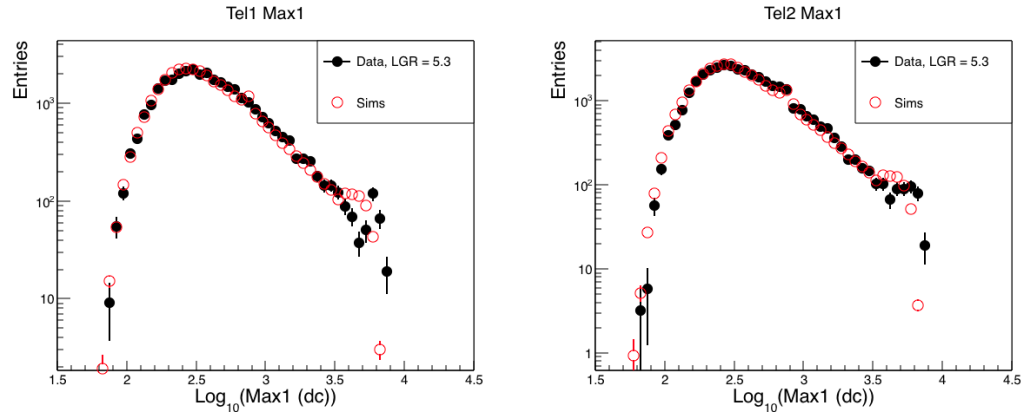

(a) Tel1 Max1

(b) Tel2 Max1

(c) Tel3 Max1

(d) Tel4 Max1

Figure 5.3 V6 Data/MC comparison of Max1 for data reconstructed with a low gain ratio of 5.3.

The Max1 distributions become much smoother for a low gain ratio of 5.3. This provides further strong evidence that the low gain ratio is driving the hardening of the V6 Crab

spectrum with the standard analysis. All telescopes except for T1 show a bump in data at about 700 dc arising from inefficiency in the switch between high and low gain. This bump is also apparent in the simulations. This occurs due to the fact that events right on the edge of switching may lose some light and fail to switch, causing an increased number of events at lower Max1, and a slight jump before the distribution continues at Max1 values above the low gain switch. The simulations also contain this inefficiency.

The Max1 distributions also vary between telescopes, with T3 data/MC comparisons indicating the highest low gain ratio between the four telescopes, and T4 indicating the lowest ratio. In addition, because the simulations were generated with a low gain ratio of 5, a difference arises between data and simulations at the highest energy tails of the Max1 distribution, where low gain channels begin to saturate. The difference is caused by both the higher ratio in data and by the differences between simulated low gain pulses and low gain pulses in data, due to the design of the electronics. Simulated low gain pulses see no broadening or non-linear saturation, because they are simply scaled down models of the high gain pulse. This leads to low gain pulses in data which saturate at higher dc values than simulated pulses in the FADCs, for the same reconstructed Max1 value. A higher saturation energy in data leads to slower saturation of the low gain (see Figure 3.13). This shows up in the Max1 distribution where the tails of the simulated Max1 distribution level off due to saturation earlier and flatter than the distribution taken from data.

Because VEGAS applies the low gain ratio equally to all telescopes, a ratio that provides the best match between data and simulations, as well as the smoothest transition between high and low gain, was chosen as the optimal low gain ratio value. This ratio was used in the re-analysis of V6 Crab data provided in the final section of this chapter. On average, a low gain ratio of 5.3 creates the best data/MC match and the smoothest curves for V6 data. Though there is variance between telescopes, an average ratio largely washes out that variation and allows for the most accurate reconstruction of energy from the image size.

5.1.1.2 Image Size

The sum of the integrated charge in all image pixels is called size. The effect of the low gain channels is difficult to measure well in data/MC comparisons of the size parameter, due to the large variations in size with other parameters such as impact distance, zenith angle, and shower height. However, for high-elevation showers, restricting the comparison to images within 150 m of the shower core provides the distribution of only the brightest images from the core region of the showers. These data/MC comparisons produce a noticeable feature in the size distribution. Size distributions for showers within 150 m of the shower core are shown in Figure 5.4, for a low gain ratio of both 5.8 and 5.3 in V6.

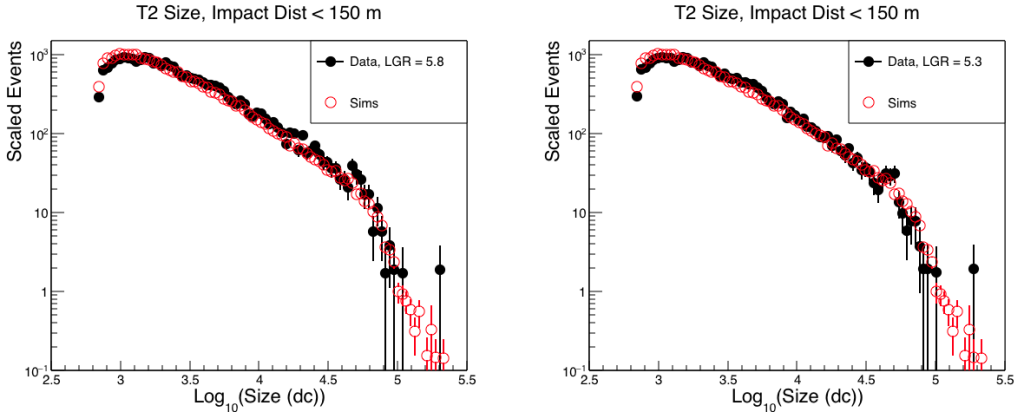

(a) Tel2 Max1, LGR = 5.8 (b) Tel2 Max1, LGR = 5.3

Figure 5.4 V6 Data/MC comparison of size for data reconstructed with a low gain ratio of 5.8 in (5.1.1.2), and a ratio of 5.3 in (5.1.1.2).

A low gain ratio of 5.8 produces a slight jump in size around 10^4 dc, corresponding to the size where the low gain comes into significant affect (see Figure 4.1). The use of 5.3 for the low gain ratio in V6 produces a smoother size distribution that transitions neatly into the low gain.

5.1.2 Data/MC Measurements of Image Brightness in V5

The data/MC studies were repeated with V5 gamma ray data and MC gamma ray simulations for the V5 detector configuration. The data shows the same features in V5 Max1 as in V6 Max1 for a mismatched low gain ratio. V5 data was initially generated with the nominal low gain ratio of 6 and with a low gain ratio of 5.3, the best fit value in V6. The data/MC distributions of Max1 in T1 and T2 are shown in Figures 5.5 and 5.6 for low gain ratios of 6 and 5.3 respectively.

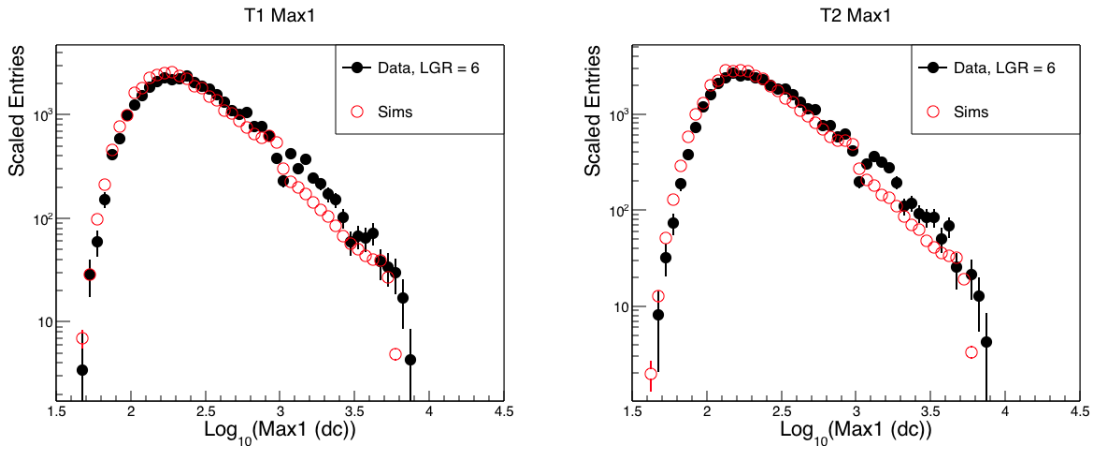

(a) Tel1 Max1

(b) Tel2 Max1

Figure 5.5 V5 Data/MC comparison of Max1 for data reconstructed with a low gain ratio of 5.3.

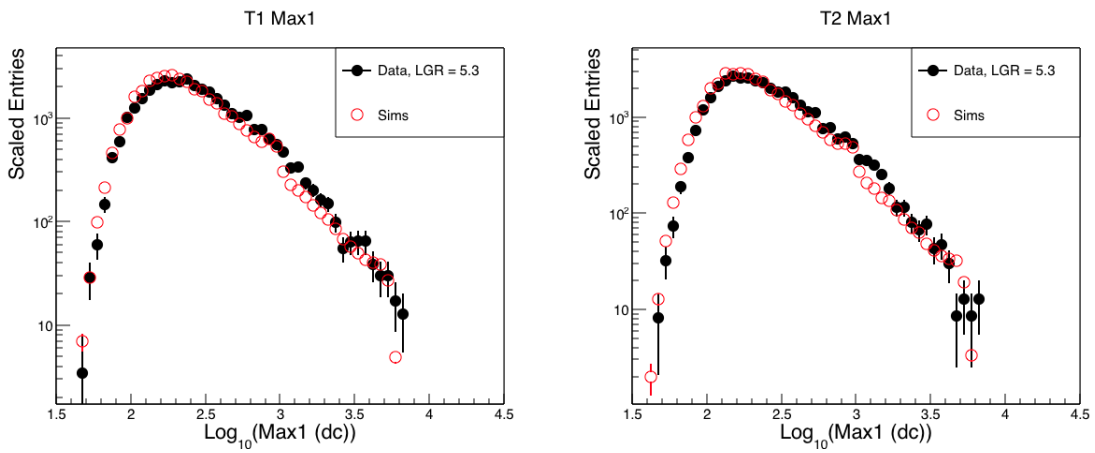

(a) Tel1 Max1

(b) Tel2 Max1

Figure 5.6 V5 Data/MC comparison of Max1 for data reconstructed with a low gain ratio of 5.3.

The low gain switch in V5 occurs at an integrated pixel size of approximately 800 dc. The nominal low gain ratio of 6 in V5 data shows a clear discontinuity at the low gain switch, after which the data jumps above the simulations. With a low gain ratio of 5.3, the data still shows a small discontinuity and rises above the simulations after the low gain switch. The V5 data was run again with lower ratios. Figure 5.7 shows the data/MC comparisons of Max1 in T1 and T2 with a low gain ratio of 5.1 applied to the data.

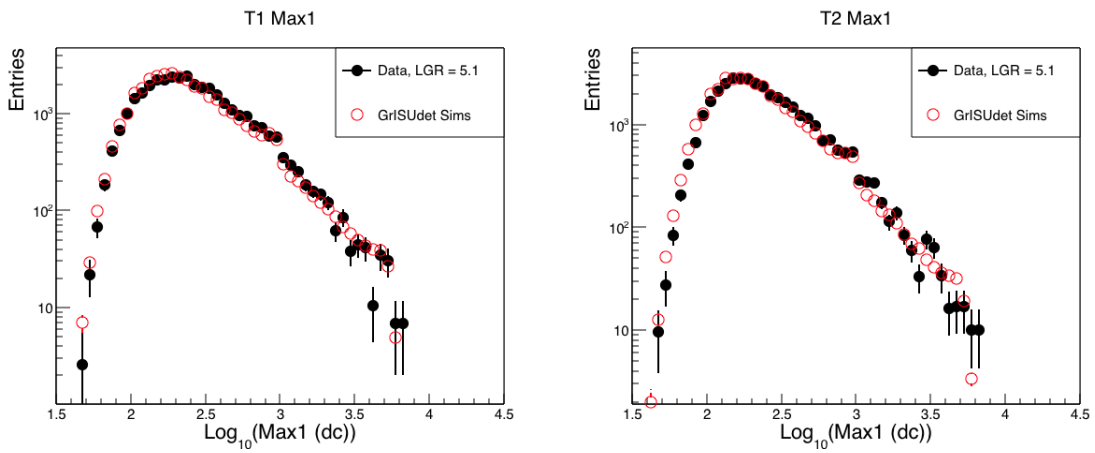

(a) Tel1 Max1

(b) Tel2 Max1

Figure 5.7 V5 Data/MC comparison of Max1 for data reconstructed with a low gain ratio of 5.3.

The use of a low gain ratio of 5.1 in V5 gamma ray data produces excellent agreement between data and MC simulations.

5.2 SAM Analysis Validation of the Low Gain Ratio

The SAM Analysis provides a useful tool for cross-checking the value of the low gain ratio. In the following sections, data from the Crab Nebula was run again through the SAM and standard analyses, this time with a low gain ratio of 5.3 for both epochs.

5.2.1 V5 Crab Spectral Analysis

Both the V5 and V6 epochs see improved agreement between the SAM and standard analyses with reduced low gain ratios. Figure 5.8 shows the results of the comparison between the two analyses in V5 data with a low gain ratio of 5.1.

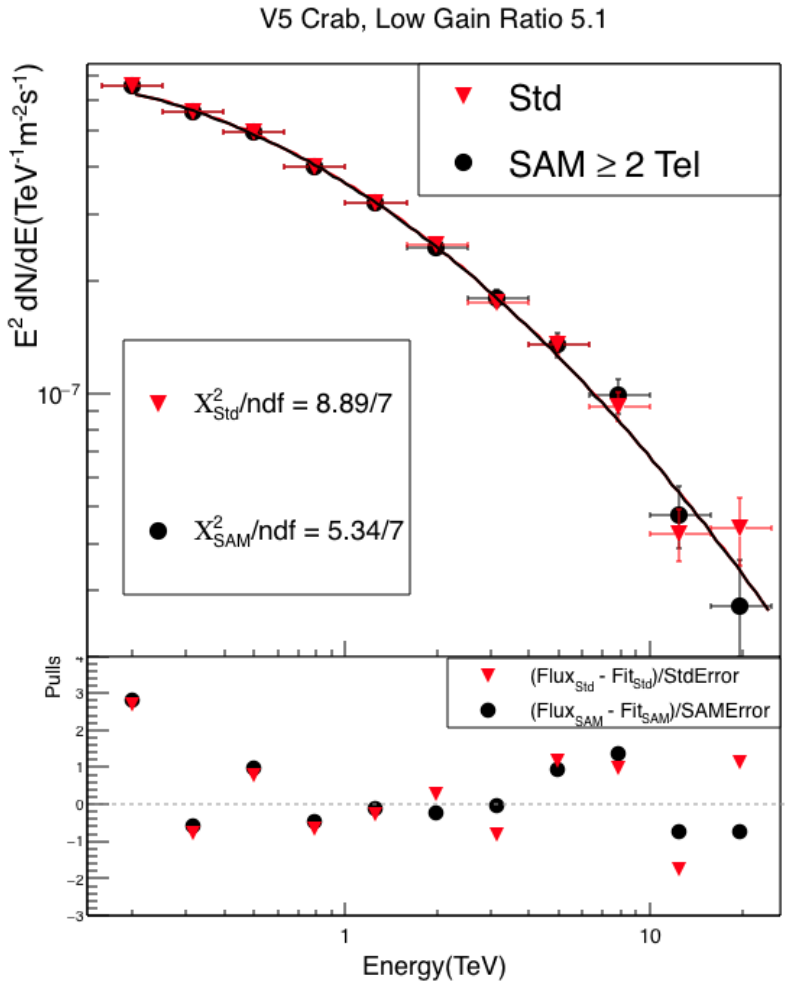

Figure 5.8 V5 Crab spectrum, comparing the standard and the SAM analysis. Data analyzed with a low gain ratio of 5.1. Pulls are shown beneath.

Another cross-check was performed by fitting the Crab spectrum with a power law above 1 TeV, at both values of the low gain ratio and in both the SAM and standard analyses. The results with the nominal low gain ratio of 6 are shown in Figure 5.9. The SAM analysis clearly softens the Crab spectrum above 1 TeV.

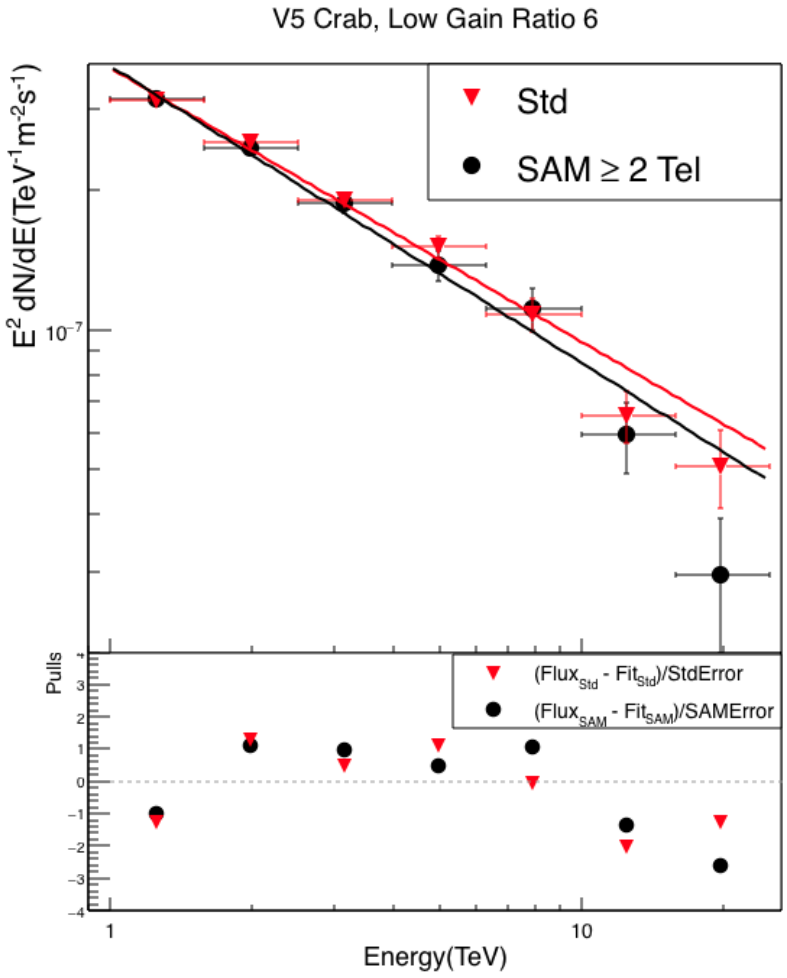

Figure 5.9 V5 Crab power law spectrum, comparing the standard and the SAM analysis. Data analyzed with a low gain ratio of 6. Pulls are shown beneath.

Figure 5.10 shows the results of applying a low gain ratio of 5.1 to the Crab analysis in V5. The agreement is much improved between the two spectral analyses. The spectral shapes show no significant bias from saturation of low gain channels, when an appropriate value of the low gain ratio is applied.

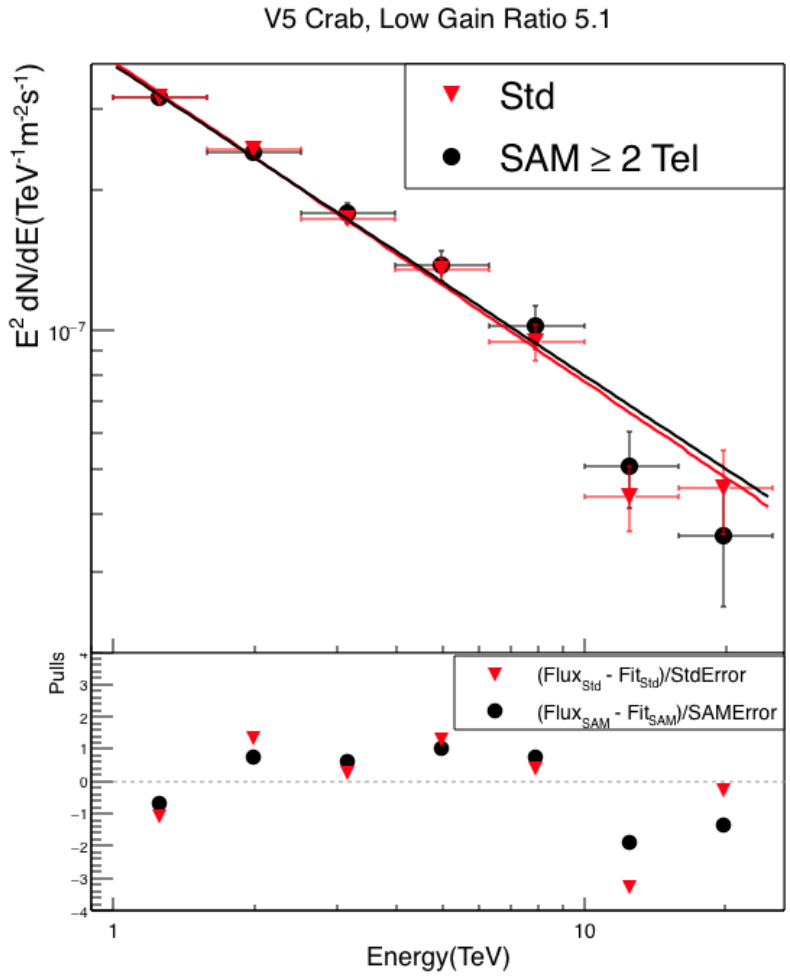

Figure 5.10 V5 Crab power law spectrum, comparing the standard and the SAM analysis. Data analyzed with a low gain ratio of 5.1. Pulls are shown beneath.

The results for the spectral analyses in V5 with power law fits are summarized in Table 5.1.

Table 5.1 Fit parameters for spectra obtained from V5 Crab Nebula data, with nominal low gain ratios compared to analysis with a low gain ratio of 5.1.

Analysis, Low Gain Ratio	Index α	σ	χ^2/ndf
V5 SAM, LGR = 6	2.64 ± 0.03	292σ	13.3/5
V5 Std, LGR = 6	2.59 ± 0.02	297σ	9.94/5
V5 SAM, LGR = 5.1	2.67 ± 0.03	292σ	8.37/5
V5 Std, LGR = 5.1	2.69 ± 0.02	296σ	15.7/5

Use of a low gain ratio of 5.1 produces much better agreement between the standard and SAM analyses in the V5 Crab spectra, without losing significance in the SAM spectrum. These results provide strong evidence for the use of a low gain ratio of 5.1 rather than 5.8 in data from the V5 epoch.

5.2.2 V6 Crab Spectral Analysis

The V6 Crab Nebula data also shows improved agreement between the two analysis methods when a low gain ratio of 5.3 is applied. The results are shown in Figure 5.11.

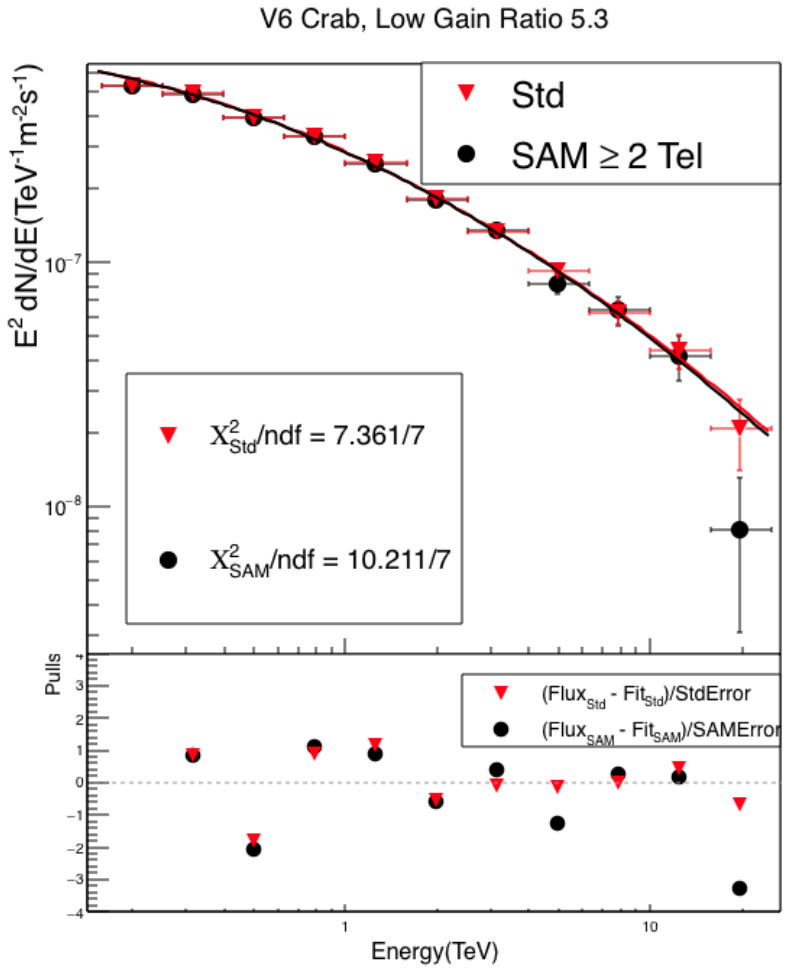

Figure 5.11 Spectrum of V6 Crab Nebula data, compared for a standard SAM energy reconstruction and analyzed with a low gain ratio of 5.3. Pulls are shown beneath.

Power law fits above 1 TeV were applied to the V6 Crab spectrum as well, for low gain ratios of 5.8 and 5.3. The results are shown in Figures 5.12 and 5.13. The results of the power law fits in V6 are summarized in Table 5.2.

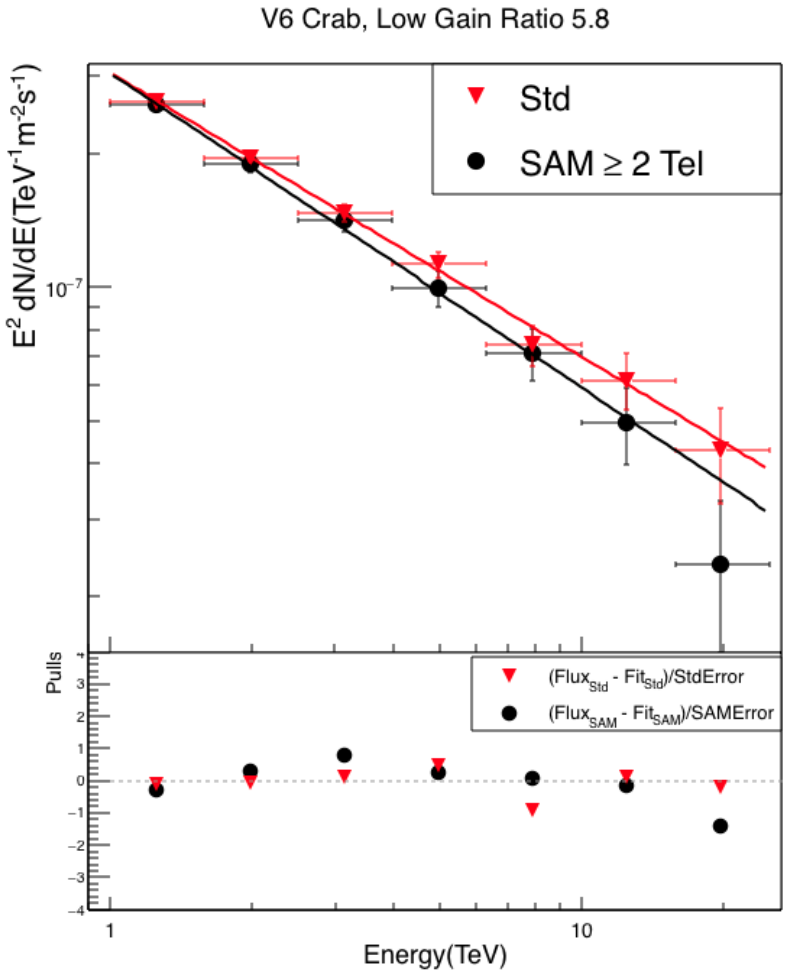

Figure 5.12 V6 Crab power law spectrum, compared for a standard SAM energy reconstruction and analyzed with a low gain ratio of 5.8. Pulls are shown beneath.

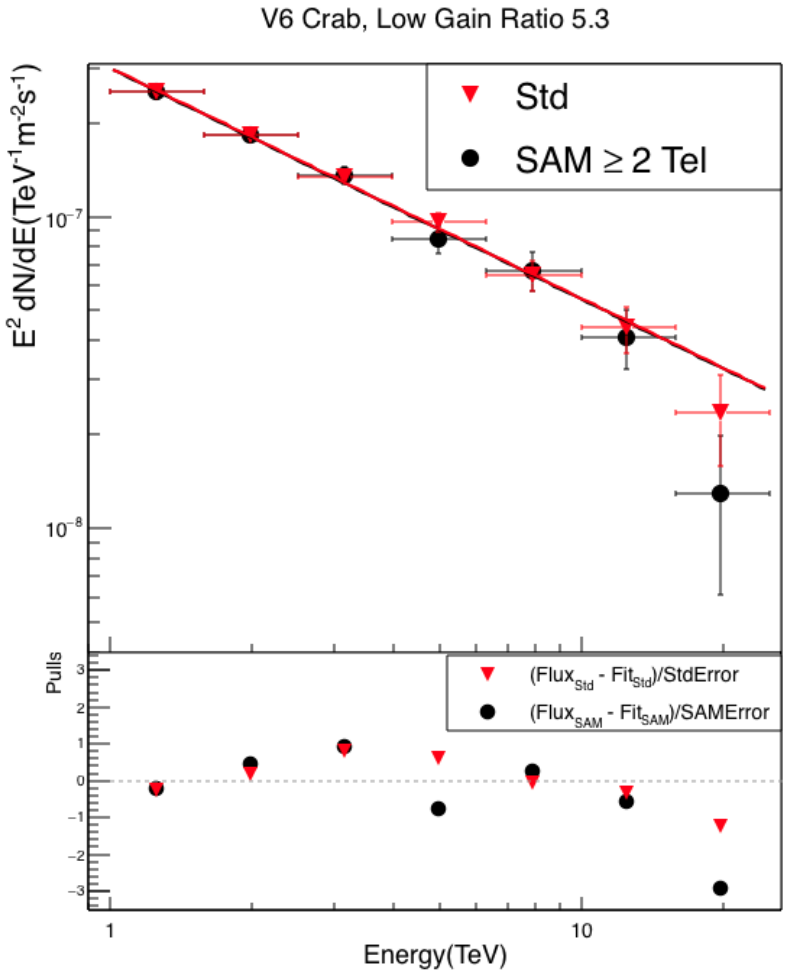

Figure 5.13 V6 Crab power law spectrum, compared for a standard SAM energy reconstruction and analyzed with a low gain ratio of 5.3. Pulls are shown beneath.

Table 5.2 Fit parameters for spectra obtained from V6 Crab Nebula data, with nominal low gain ratios compared to use of a low gain ratio of 5.3.

Analysis, Low Gain Ratio	Index α	σ	χ^2/ndf
V6 SAM, LGR = 5.8	2.71 ± 0.04	267σ	2.86/5
V6 Std, LGR = 5.8	2.64 ± 0.03	276σ	1.06/5
V6 SAM, LGR = 5.3	2.74 ± 0.04	267σ	2.63/5
V6 Std, LGR = 5.3	2.74 ± 0.03	274σ	2.08/4

Use of a low gain ratio of 5.3 produces much better agreement between the standard and SAM analyses in the V6 Crab spectra, without losing significance in the SAM spectrum. These results provide strong evidence for the use of a low gain ratio of 5.3 rather than 5.8 in data from the V6 epoch.

5.2.3 Combined Epochs Crab Spectral Analysis

Combining the Crab Nebula data from V5 and V6 both extends the spectrum to higher energies and provides an estimate of the bias due to choice of low gain ratio in spectra covering multiple epochs, such as the spectra used in setting EBL limits discussed in Chapter 7. Figure 5.14 shows the spectral comparison between a SAM and standard analysis with nominal low gain ratios, in the analysis of the combined V5 and V6 data. Spectra were fit with a log-parabolic function of the same form as in the individual epochs.

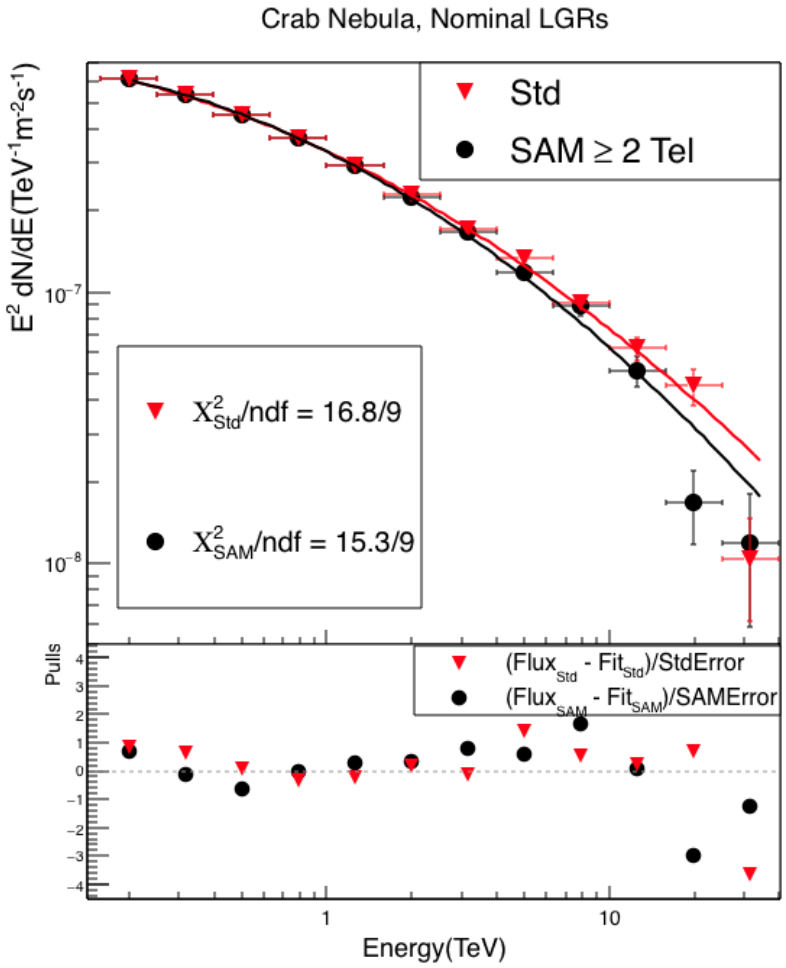

Figure 5.14 Spectral comparison of combined V5 and V6 Crab data, analyzed with low gain ratios of 6 in V5 and 5.8 in V6. Pulls are shown beneath.

Figure 5.15 shows the spectral comparison between a SAM and standard analysis with nominal low gain ratios, in the analysis of the combined V5 and V6 data.

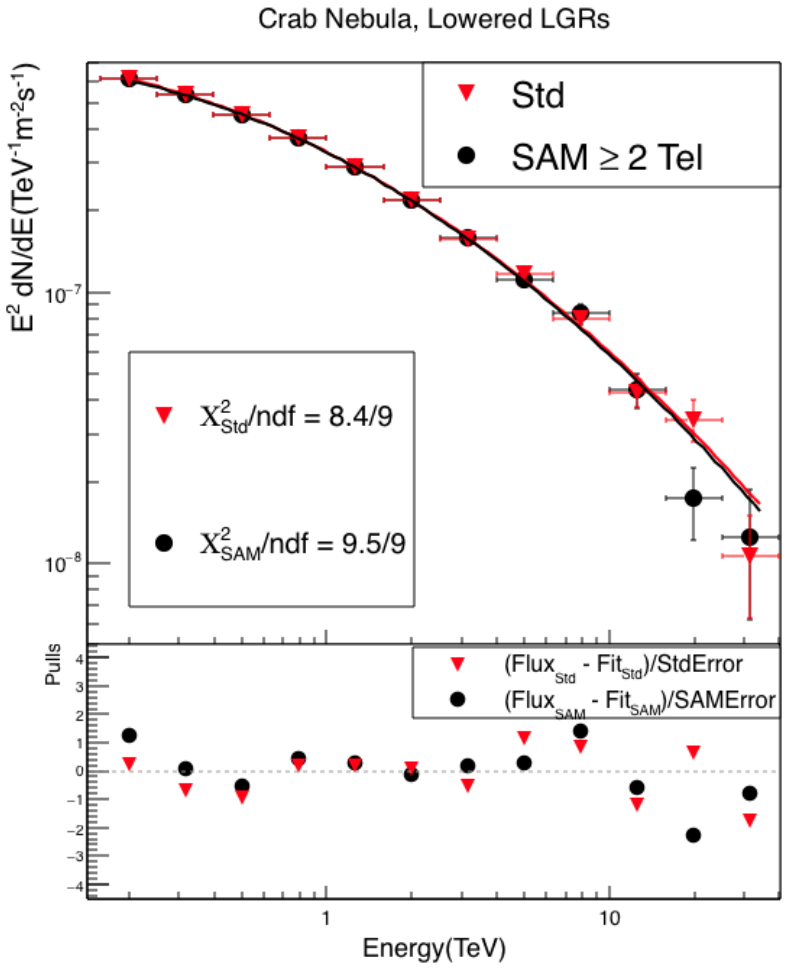

Figure 5.15 Spectral comparison of combined V5 and V6 Crab data, analyzed with low gain ratios of 5.1 in V5 and 5.3 in V6. Pulls are shown beneath.

The use of nominal low gain ratios causes a significant bias to the Crab spectrum measured over the combined V5 and V6 epochs. The spectra diverge at about 2–3 TeV. Table 5.3 gives the best fit parameters for the log-parabolic spectral fits in V5, V6, and the combined dataset. Over the full energy range of the combined dataset, the best fit index in the SAM analysis is softer than the standard analysis best fit index by greater than 3 σ. The SAM analysis also shows greater curvature over the standard analysis by approximately 3 σ.

Table 5.3 Fit parameters for spectra obtained from V5 and V6 Crab Nebula data, with nominal low gain ratios compared to data analysis with a low gain ratio of 5.3.

	α	β	χ^2/ndf	σ
V5 SAM, LGR = 6	2.49±0.01	0.0938±0.01	9.99/7	262σ
V5 Std, LGR = 6	2.47±0.01	0.0700±0.0088	6.62/7	297σ
V5 SAM, LGR = 5.1	2.50±0.01	0.0990±0.0105	5.3/7	292σ
V5 Std, LGR = 5.1	2.50±0.01	0.0993±0.0094	8.9/7	296σ
V6 SAM, LGR = 5.8	2.55 ± 0.01	0.0785 ± 0.012	6.02/7	263σ
V6 Std, LGR = 5.8	2.52 ± 0.01	0.0520 ± 0.011	8.58/7	272σ
V6 SAM, LGR = 5.3	2.56 ± 0.01	0.0853±0.013	10.2/7	271σ
V6 Std, LGR = 5.3	2.56 ± 0.01	0.0822±0.011	7.4/7	279σ
V5/V6 SAM, LGR = 6/5.8	2.520 ± 0.008	0.0875 ± 0.0056	15.3/9	395σ
V5/V6 Std, LGR = 6/5.8	2.493 ± 0.006	0.0718 ± 0.0048	16.8/9	405σ
V5/V6 SAM, LGR = 5.1/5.3	2.528 ± 0.008	0.0941±0.0058	9.5/9	395σ
V5/V6 Std, LGR = 5.1/5.3	2.534 ± 0.007	0.0900±0.0052	8.4/9	403σ

In addition to the improved measurement of the low gain ratio, the SAM analysis indicates that saturation of low gain channels does not contribute strongly to the systematic biases of a standard VERITAS analysis. In both the V5 and V6 epochs, there is excellent agreement between the standard analysis and the SAM analysis when a low gain ratio of 5.3 is applied in V6, or 5.1 in V5. The value of the low gain ratio contributes more significantly to systematic bias arising at multi-TeV energies than saturation of low gain channels. In addition, saturation of low gain channels does not occur until energies of about 10 TeV. The low gain ratio begins to effect energy bias as soon as pixels enter the low gain, however. Therefore, the low gain ratio causes a bias over a wider energy range than saturation and has a greater affect on spectral shapes above approximately 1–2 TeV.

5.2.4 V5 Mrk 421 Analysis

As a final cross-check, the SAM analysis was applied to the V5 spectrum of Mrk 421. Mrk 421 experiences a high level of variability in flux. Because different flux states show evidence of spectral index variability, only a subset of Mrk 421 data was chosen for analysis from the V5 epoch. The VHE spectrum of Mrk 421 had an average flux above 1 Crab Unit for the 2009–2010 season, with about 7 hours of observations fitting data selection criteria for the SAM analysis. The source is fit with an exponential cutoff of the form

$$\frac{\mathrm{d}N}{\mathrm{d}E} = N_0 \left(\frac{E}{E_0} \right)^{-\Gamma} \cdot e^{-E/E_{cut}} \tag{5.1}$$

where E_0 is fixed at 1 TeV.

The results of the spectral analysis are shown in Figures 5.16 and 5.17, for analyses with the low gain ratio set to 6 and 5.1, respectively. The best-fit spectral indices and cutoff energies for each analysis are summarized in Table 5.4.

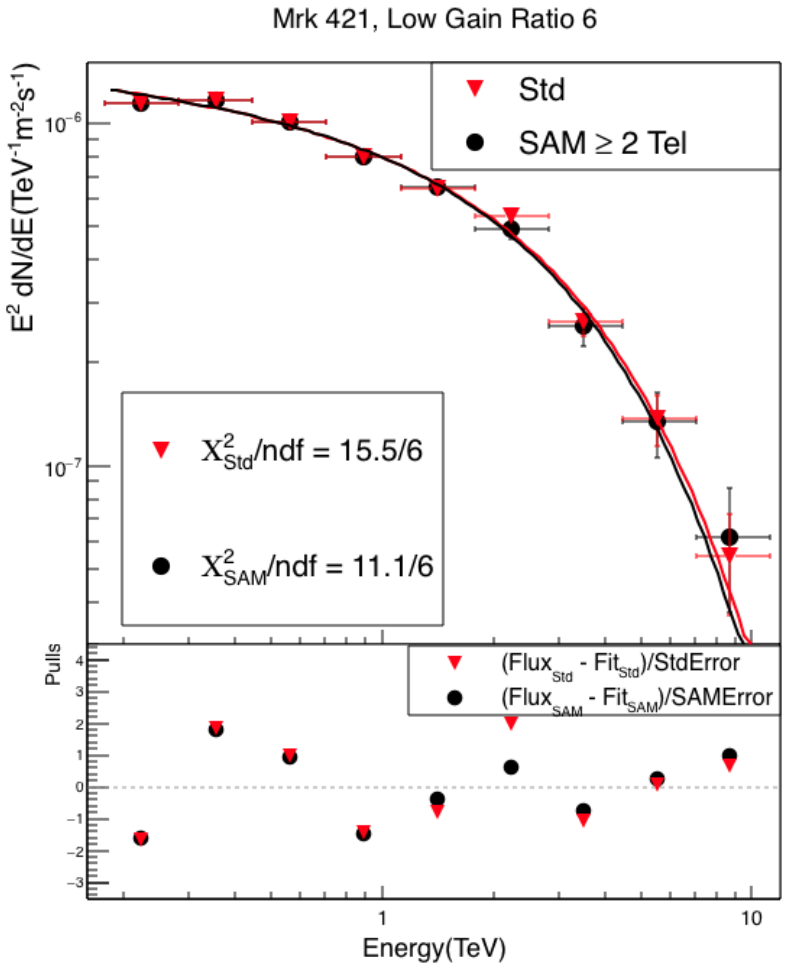

Figure 5.16 Spectral comparison of V5 Mrk 421 data, analyzed with a low gain ratio of 6. Pulls are shown beneath.

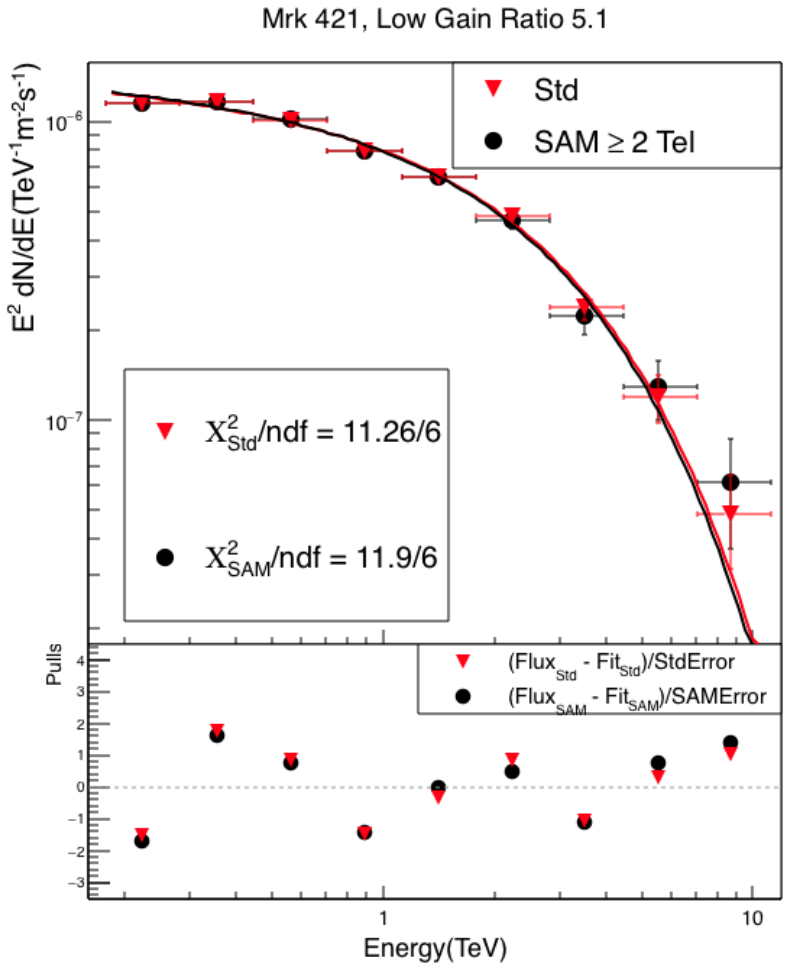

Figure 5.17 Spectral comparison of V5 Mrk 421 data, analyzed with a low gain ratio of 5.1. Pulls are shown beneath.

Table 5.4 Fit parameters for spectra obtained from V5 Mrk 421 data, analyzed with a standard and SAM analysis at both the nominal and the updated low gain ratio values.

Analysis, Low Gain Ratio	Index α	E_{cut} (TeV)
SAM, LGR = 6	2.09 ± 0.04	2.71 ± 0.33
Std, LGR = 6	2.10 ± 0.04	2.85 ± 0.29
SAM, LGR = 5.1	2.07 ± 0.05	2.41 ± 0.29
Std, LGR = 5.1	2.07 ± 0.04	2.48 ± 0.24

Due to the low cutoff energy of less than 3 TeV, the SAM analysis and updated low gain ratios have a smaller systematic effect on the 2010 spectrum of Mrk 421 than the Crab spectra from V5. The systematic effect from the nominal low gain ratios compared to the updated low gain ratios is below the statistical error on the index. The systematic effect on the cutoff energy, ΔE_{cut}, in a standard analysis is comparable to the statistical error on the standard analysis with nominal low gain ratios. Therefore, the systematic bias with nominal low gain ratios still has a non-negligible effect on the spectral shape.

CHAPTER 6. SHOWER MAXIMUM

The number of particles in a gamma-ray induced air shower follows a coma distribution, with the peak of the distribution corresponding to the height at which the maximum number of particles is produced in the shower. As discussed in Chapter 2, Section 2.1.2.2, this peak is dependent on the initial gamma-ray energy, E_0. The height at which this peak occurs is called "shower maximum" (with "shower max" and "shower height" often used synonymously), and follows a log-log distribution with respect to E_0.

6.1 Theoretical Shower Maximum

Recalling the discussion of shower maximum from Section 2.1.2.2, the point at which the maximum number of Cherenkov photons are produced can be found by solving Equation 2.9 for the depth, t at which number of particles, N is maximized. This occurs when the age parameter, s (described in Section 2.10), reaches the value $s = 1$. At a "shower age" of $s = 1$, the electrons and positrons in the shower no longer have enough energy to produce bremsstrahlung radiation. Therefore, no more particles are produced in the shower. The particles can continue to produce Cherenkov radiation below this limit, but no new particles are produced. Thus $s = 1$ places an upper limit on the age of shower maximum. Equations 2.9 and 2.10 are reproduced here, in Equations 6.1 and 6.2, respectively.

$$N(t) \approx \frac{0.31}{\beta_0^{1/2}} e^{t(1-1.5\ln(s))} \tag{6.1}$$

$$s = 3t/(t + 2\beta_0) \tag{6.2}$$

The shower depth is found from solving Equation 6.2 for $s = 1$. The energy is given in the term β_0, where $\beta_0 = \ln(E_0/E_c)$. The value of E_c is the critical energy for bremsstrahlung, $E_c = 84$ MeV. The radiation depths relate to slant depth by $\chi = 37.15t$.

Converting from slant depth to height above sea level can be tricky due to the non-uniform nature of the atmosphere. The simplest toy model provides a simple exponential relationship between slant depth and vertical height based on an isothermal atmosphere. For such an atmosphere, the relation is simply $\chi = e^{-h/h_0}$. However, this is a highly idealized atmosphere. In reality, the atmospheric is not isothermal, and more accurate models can be generated at different regimes for a more realistic temperature function.

One such realistic model is provided by Greider in [30], for an atmosphere. For depths of χ>230 g/cm^2, the Greider profile is given in Equation 6.3

$$h(\text{km}) = 44.34 - 11.861\chi^{0.19} \tag{6.3}$$

6.2 Reconstructing Shower Maximum with VEGAS

Versions of VEGAS prior to 2.5.7 contained only an incorrect calculation of shower maximum. The quantity labeled as shower max in prior versions of VEGAS reconstructed shower height from the distance between pairs of telescopes and the angle between the two telescope images. This calculation assumed that the angular distance between centroids in pairs of telescopes was equivalent to the angular distance between the telescopes measured from the shower core. The geometric reconstruction is shown in Figure 6.1.

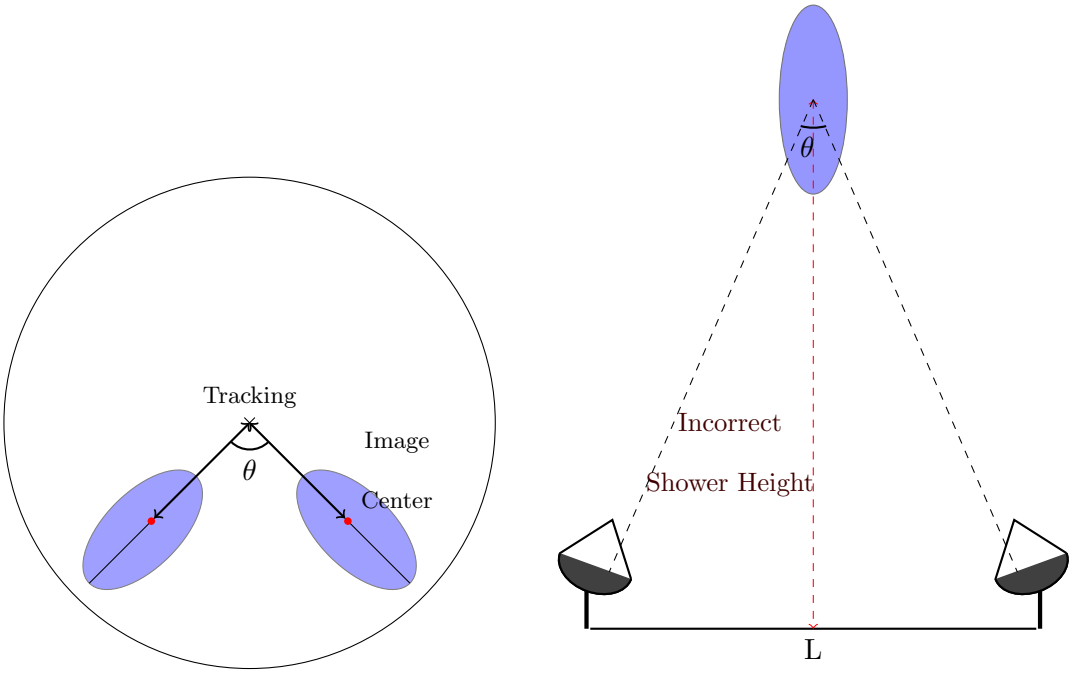

(a) Camera Coordinates (b) Incorrect Shower Max Reconstruction

Figure 6.1 Incorrect method for implementing geometric reconstruction of shower height in VEGAS.

This calculation produces a value that is roughly constant in energy, with a gaussian distribution of shower heights centered on about 10 km for all gamma-ray events. Cosmic ray events are reconstructed with a broader distribution and a similar mean, thus leading to a cut on the false shower height that is not motivated by an accurate reconstruction (as briefly discussed in Chapter 4). Figure 6.2 shows the shower height distribution as a function of energy for the old reconstruction in both V5 and V6.

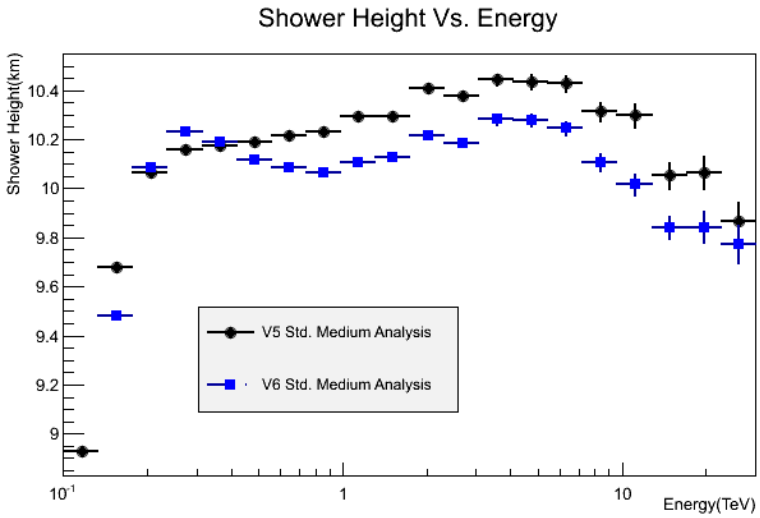

Figure 6.2 Reconstructed shower height with the old VEGAS method.

This method fails because the centroid displacement varies with both shower height and Cherenkov angle. Therefore, the angular displacement of the centroids between the two telescopes is not equivalent to the angular displacement between the two telescopes with respect to the shower maximum.

A more accurate calculation was implemented in VEGAS version 2.5.7, based on the calculated developed in [46], with some modifications to ensure accurate code implementation and account for shower physics.

6.2.1 Geometric Calculation of Shower Maximum

An accurate measure of shower maximum can be obtained geometrically from VERITAS data with a single telescope. Only the image centroid, angular pointing offset from the source position, and distance to shower core are necessary to reconstruct the shower maximum, for an accuracy of about 20%. Figure 6.3 shows the geometry of the telescope relative to the shower axis.

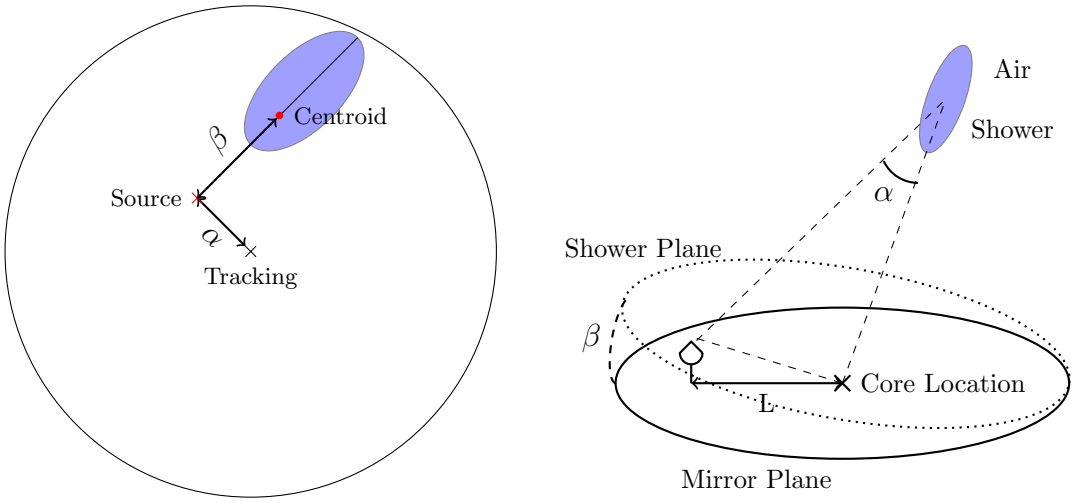

(a) Camera Coordinates

(b) Geometric Shower Max Reconstruction

Figure 6.3 Correct method for implementing geometric reconstruction of shower height in VEGAS.

The calculation of shower maximum arises from a simple triangle constructed between the image in the telescope, the location of the shower core in the mirror plane, and the shower maximum. The angular distance, α, in the camera between the tracking position and the image centroid, corresponds to the angle between the shower axis and the telescope location, as measured from the shower maximum. The calculation of shower maximum for observations taken at the source position, for which the mirror plane is equivalent to the shower plane is then simply shown in Equation 6.4.

$$h_{\max} = \frac{L}{\tan(\alpha)} \tag{6.4}$$

where L is the distance from the shower core in the mirror plane to the telescope location in the mirror plane.

For observations taken at an offset of angular distance β to the source position, a correction is applied as shown in Figure 6.3. This correction translates distance L, in the mirror plane into distance R in the shower plane. The distance R in the shower plane

is given by $R = \frac{L}{\cos(\beta)}$. The final resulting calculation of shower max from an individual telescope is shown in Equation 6.5.

$$h_{\max} = \frac{L}{\cos(\beta)\tan(\alpha)} \tag{6.5}$$

Having multiple telescopes can improve the accuracy of the final result by averaging out small errors from a single telescope. Therefore, all image telescopes can be looped over with a value of $h_{\max}$ obtained for each telescope, leading to a final calculation shown in Equation 6.6.

$$h_{\max} = \frac{1}{n_{tel}} \sum_{i=0}^{n_{tel}} \left(\frac{L_i}{\cos(\theta_i)\tan(\alpha_i)} \right) \tag{6.6}$$

This reconstruction gives the height of shower maximum above the VERITAS detector for showers in the shower plane. For increasing zenith angle, ϕ, the vertical shower height changes by a factor of $h_{max,zenith} = h_{max} \cdot \cos(\phi)$.

6.2.2 Shower Impact Distance and Shower Maximum

Due to the physics of the Cherenkov angle and photon arrival times within the shower, Equation 6.6 only provides a correct measure of shower height for telescopes falling within the Cherenkov ring on the ground (discussed in greater detail in Section 2.1.2.3). As shown by A. M. Hillas in [34], only a detector at certain distances from the shower core receives photons emitted from different heights along the shower axis simultaneously. These distances fall within the Cherenkov ring caused by the focusing of light at a particular distance from the core. The Cherenkov angle increases with increasing atmospheric depth, which leads to a bright rim at about 130–170 m from the core. Figure 6.4, from [34], shows a simple model of the timing and angle effects that lead to the Cherenkov ring.

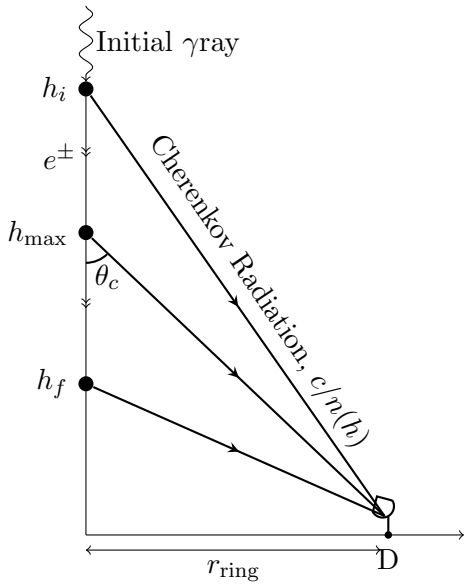

Figure 6.4 A simple model of light produced in a Cherenkov shower, based on Figure 1 of [34]. Photons emitted at across the full shower all arrive simultaneously to a detector, D, at distances r from the shower core corresponding to the radius of the Cherenkov ring.

A detector placed too close to the shower core will receive photons from lower heights earlier, thus negatively biasing the reconstructed shower maximum. The opposite occurs for a detector at too large a distance from the shower core. Therefore, not all telescopes in the array can be used to reconstruct shower height. Only those telescopes that sit near the Cherenkov ring will produce an accurate shower maximum from a geometric reconstruction of the image in the camera. This effect is shown in Figure 6.5, for example showers of 3 and 5 TeV. There is a clear rise in reconstructed shower height in telescopes closer to the shower core than 130 m. At impact distances of approximately 130–170 m, the reconstructed shower height is fairly flat. Beyond about 170 m, the reconstructed height rises again, for a positively biased shower maximum.

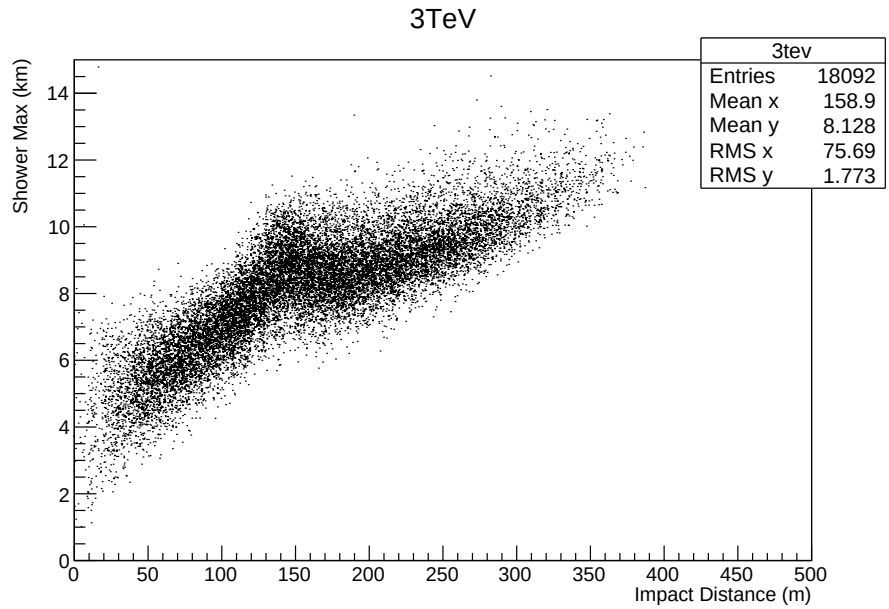

(a) 3 TeV

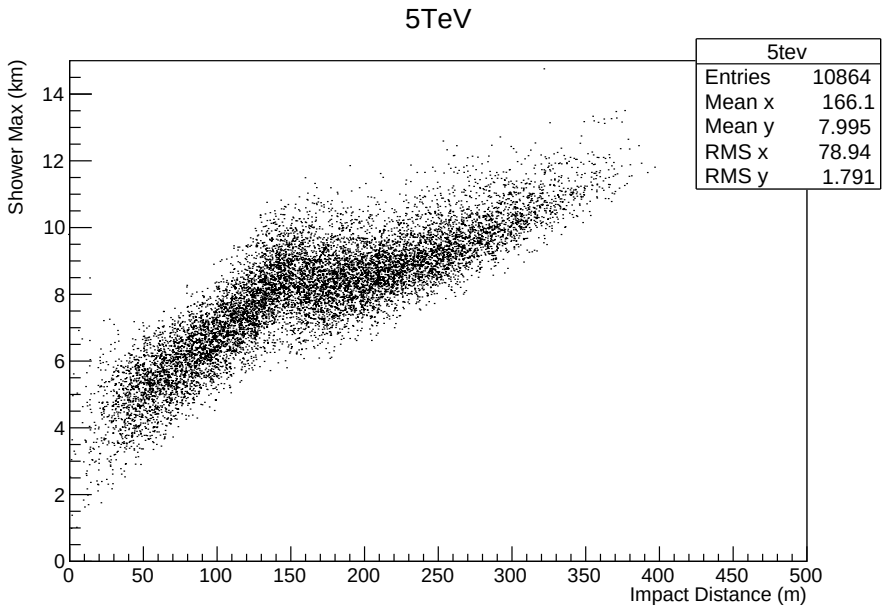

(b) 5 TeV

Figure 6.5 Reconstructed shower height from single telescopes compared to telescope impact distance.

Figure 6.6 shows the effect of impact distance on the reconstructed shower height from single telescopes, for a range of 100–300 m, in increments of 20 m. This reconstruction was tested on CORSIKA-grISUdet simulations at 20 degree zenith angle, generated for the V5 epoch. An impact distance range of 130–170 m was chosen for analysis presented in this chapter. Only those telescopes falling within the allowed range of impact distances are averaged to produce the reconstructed shower maximum from Equation 6.6.

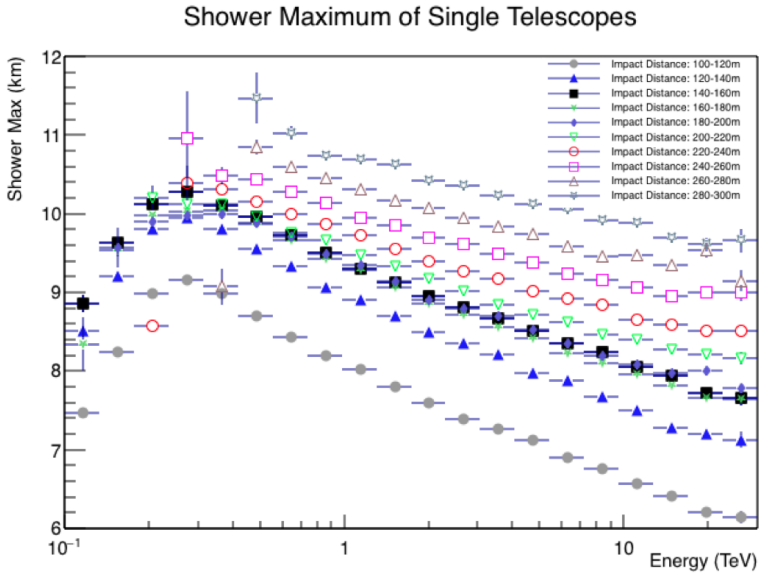

Figure 6.6 Reconstructed shower height from single telescopes at varying impact distances.

Figures 6.7 and 6.8 show the reconstructed shower height of V5 and V6 simulations at 20 degrees to zenith, for telescopes falling within 130–170 m of the shower core.

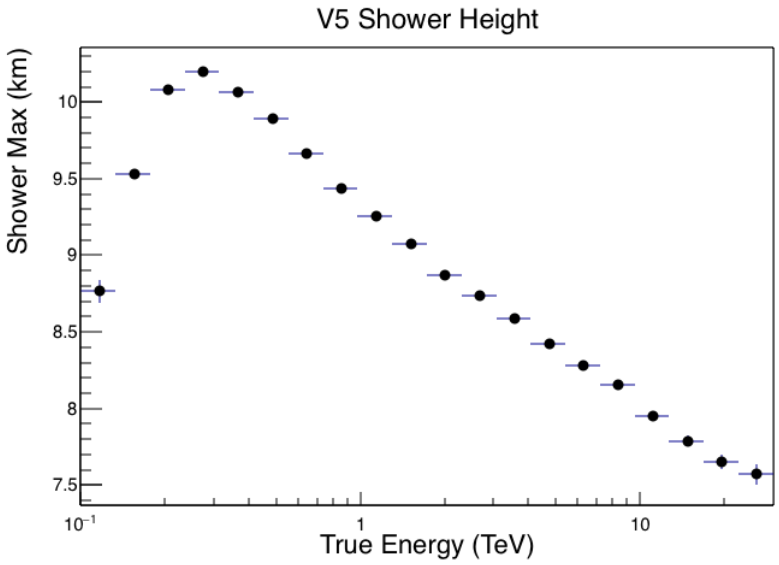

Figure 6.7 Reconstructed shower height in V5.

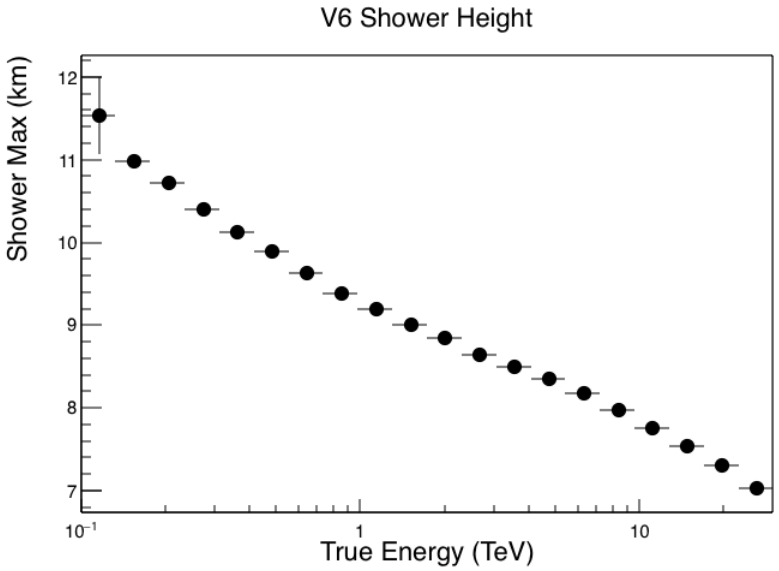

Figure 6.8 Reconstructed shower height in V6.

The shower height is well reconstructed in V5 with the updated shower maximum calculation.

6.2.3 Comparison of Shower Height Reconstruction to Simulations

Equation 6.6 provides height above sea level. To compare to theory, an accurate atmospheric profile must be used to convert depth in the atmosphere, χ, to vertical height. The use of different atmospheric profiles can lead to differences in atmospheric absorption of up to 60% [6]. Additionally, the reconstructed height begins 1.27 km above sea level, corresponding to the elevation of the array. Therefore, for an accurate comparison to theoretical values, the difference of 1.27 km is accounted for by subtracting that amount from the values from theory.

The air-shower simulation package, CORSIKA, also takes as an input an atmospheric profile which is used for all simulated air showers. For VERITAS simulations, this atmospheric profile is based on radiosonde measurements taken at the University of Arizona campus in Tucson, about 40 miles from the VERITAS location. The radiosonde measurements determine pressure, temperature, and relative humidity to high precision for the VERITAS sight, up to 37.5 km [14]. These measurements are then averaged into summer and winter atmospheres, extending roughly from April to October and November to March, respectively. The summer data excludes the monsoon months of July and August, during which VERITAS shuts down operations due to the high humidity and heavy rainfall typical of those months in the area. Above 37.5 km, MODTRAN models are used up to a height of 100 km.

Thus, to cross-check the shower maximum produced from CORSIKA simulations, the matching atmospheric profile used to produce the simulated gamma-rays should be used to compare reconstructed and simulated shower height. This atmospheric profile is given in Equation 6.7, for the conversion between atmospheric depth and vertical height above the elevation of VERITAS.

$$h(\text{km}) = 44.34 - 11.861\chi^{0.19} \tag{6.7}$$

Figure 6.9 shows the dependence of shower height on zenith angle, for 0, 20, and 30 degrees to zenith, compared to the true shower height from CORSIKA simulations at 20 degrees to zenith. The CORSIKA simulations take into account the height of the detector above sea level.

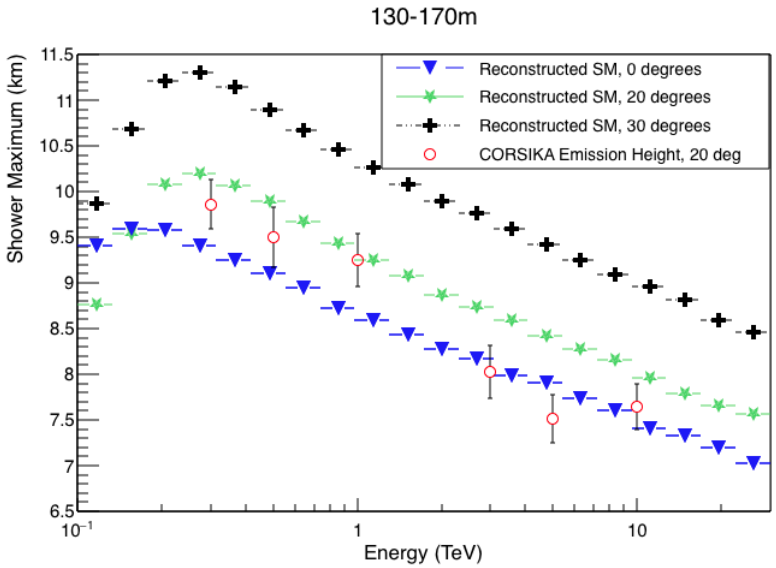

Figure 6.9 Reconstructed shower height from single telescopes at varying zenith angles.

The true shower height from CORSIKA agrees well at low energies with the reconstructed shower height at 20 degrees to zenith. The agreement is less strong at high energies. The shower height obtained from CORSIKA must to be corrected for zenith angle, as CORSIKA output is in slant depth which converts to vertical height from zenith, h_{zenith}, from Equation 6.7. The conversion for zenith angles $\phi > 0$ is given by $h_{rec} = h_{zenith}/\cos(\phi)$.

6.3 Applying Shower Maximum to VERITAS Energy Reconstruction in V5

As discussed in Chapter 3, the VERITAS reconstructs energy from lookup tables binned in impact distance and image size. The size of an image correlates directly to the amount of light striking the telescope. However, the size parameter in energy lookup tables is an

average quantity that does not take shower physics such as the height of the shower into account. Variations in shower maximum of events with the same initial energy give rise to one source of systematic bias in the energy reconstruction. Showers which occur lower lower in the atmosphere are brighter and will, on average, bias the energy reconstruction towards high energies. The opposite happens for higher, dimmer showers.

An accurate measure of shower maximum can therefore be used to iterate on the initial energy estimate from the lookup table. Applying shower maximum to the energy reconstruction has power to improve the overall energy bias.

6.3.1 Energy Bias from Variations in Shower Height

The shower height reconstruction described at the start of this chapter, measured only from telescopes within 130–170 m from the shower core, produces a strong correlation between reconstructed energy and reconstructed shower height. Both individual telescopes and the average shower maximum from all telescopes in the appropriate impact distance range show this correlation.

This correlation between reconstructed shower height and reconstructed energy bias, $E_{bias} = (E_{rec} - E_{true})/E_{true}$, for logarithmically spaced energy bins between 100 GeV and 30 TeV in the V5 epoch is shown in Figure 6.10. Though other sources of bias exist within the reconstructed energy, a linear relationship between shower height and reconstructed energy can be fit to each bin for the majority of events.

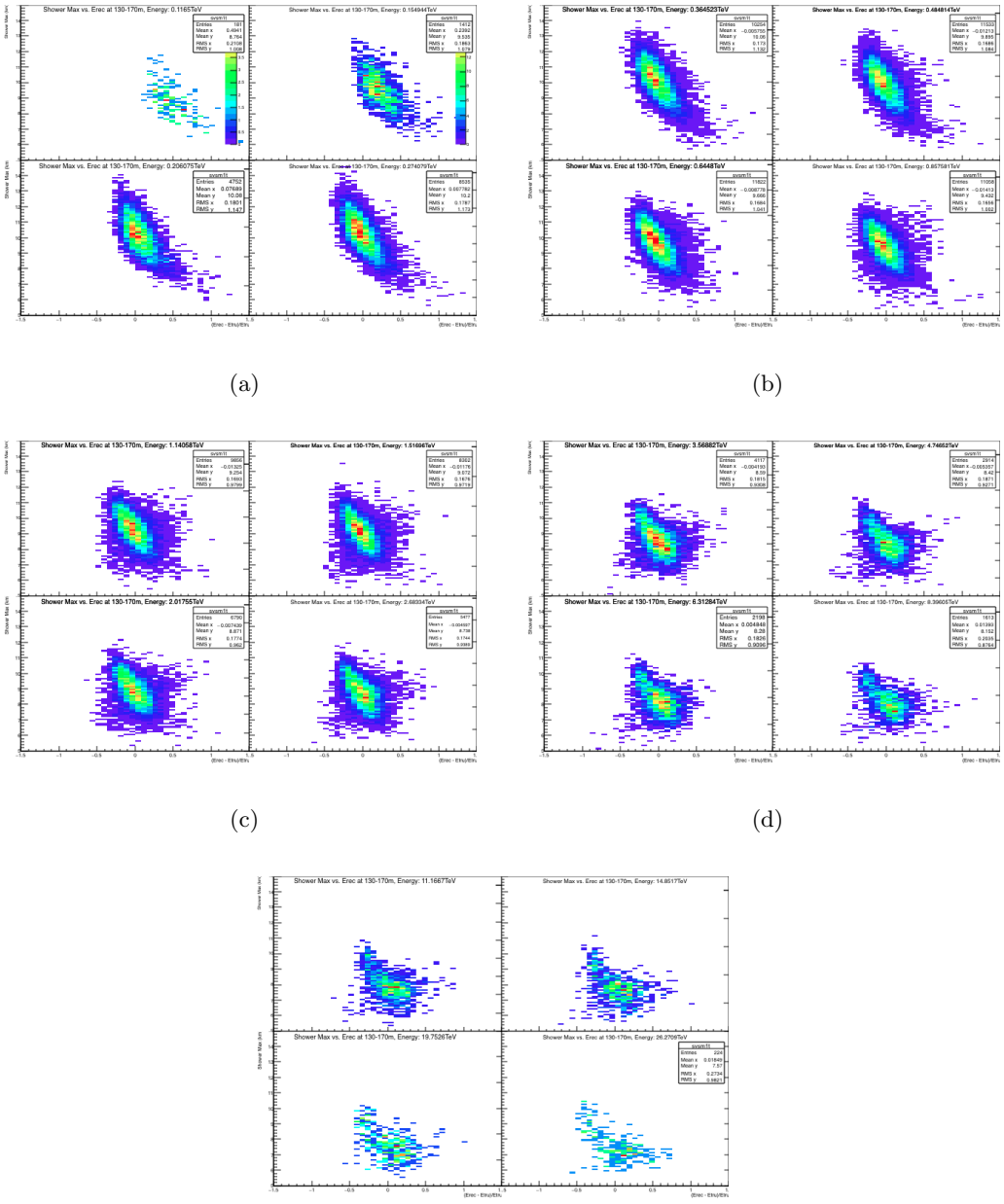

Figure 6.10 Reconstructed shower height compared to energy bias.

The energy bias increases to positive bias for deeper showers, and increases towards greater negative bias for showers reaching their maximum above the average shower height for that energy bin. This shows that energy reconstruction is correlated with depth of shower

maximum as reconstructed with the updated geometric method. Therefore, reconstructed shower maximum can be used to iterate on the initial energy reconstruction and improve the energy resolution of gamma-ray air-showers measured by VERITAS.

6.3.2 Shower Max Iteration

Because the shower height correlates nicely with energy when reconstructed from the appropriate impact distances, shower height can be used as a second order correction on the energy reconstruction. As shown in Section 6.3.1, image brightness correlates to the depth of shower maximum. Showers that penetrate deeper into the atmosphere produce brighter images at the same impact distance, while those which reach their maximum at a greater height produce dimmer images by the time they reach the array. The linear correlation between the reconstructed energy and shower height is shown in Figure 6.11, for showers of about 1 TeV and reconstructed height from Equation 6.6.

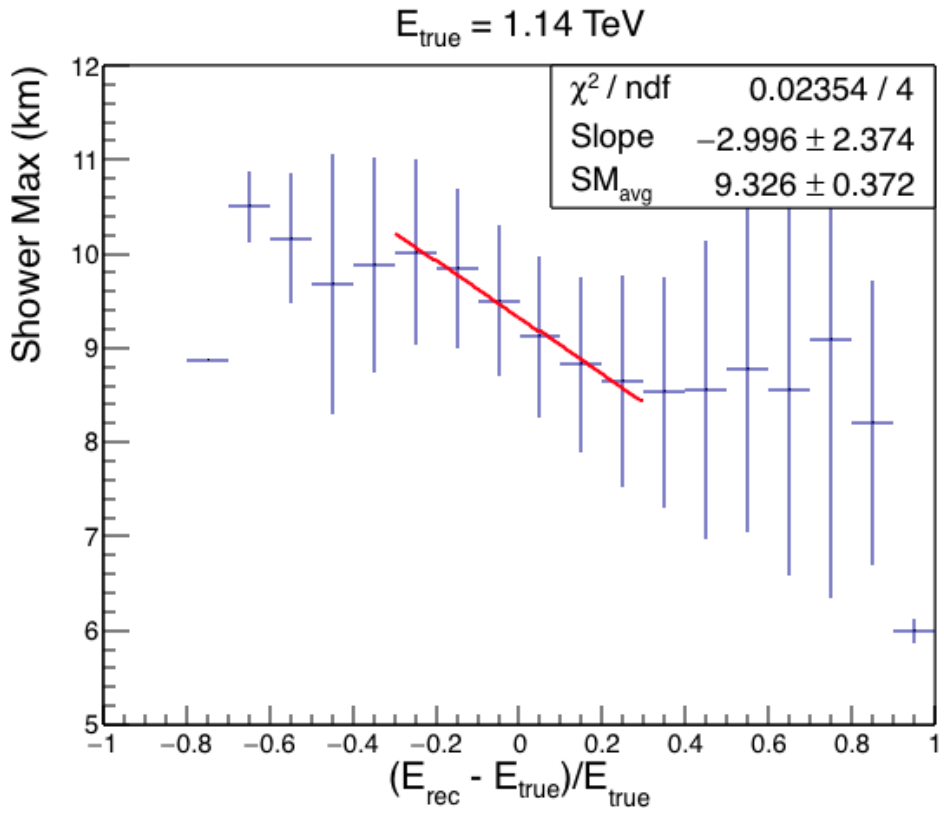

Figure 6.11 Reconstructed shower height compared to energy bias of simulated events at 1 TeV.

Therefore, the standard VERITAS energy reconstruction which considers only average image size at a given impact distance, broadens the energy resolution due to shower height fluctuations. Additionally, at the low energy threshold of the detector, only the brightest images will trigger an event. These brightest images correspond to the showers that penetrate more deeply than the average shower into the atmosphere, and thus are likely to fall into a higher reconstructed energy bin than they truly belong in. This effect is responsible for the sharp rise in the energy bias curve at energies of around 80–200 GeV (See Figure 3.10).

Shower height therefore has a lot of power to improve the energy resolution and energy bias, especially at the low end of the VERITAS energy range. A simple, second-order

correction can be introduced to iterate on the first reconstructed energy based upon the shower height and expected bias introduced at that shower height. The approximately linear correlation between reconstructed shower maximum, SM_{rec}, and expected energy bias, E_{bias}, is given in Equation 6.8, given the correct slope, a, and average shower height, SM_{avg}, for the energy bin matching the initial energy estimate. The average shower height is taken to be the height at which energy bias is zero.

$$E_{bias} = (SM_{avg} - SM_{rec})/a \tag{6.8}$$

where the negative slope of the energy bias is represented by subtracting the factor of aSM_{rec} from the average shower height. The bias on the energy is given by $E_{bias} = \Delta E/E_{true}$, where E_{true} is the true energy of the initial gamma ray, and $\Delta E = E_{true} - E_{rec}$. The slope, a, is input as a positive value during the reconstruction.

The expected energy bias provided by plugging shower height into the correct equation for the initially reconstructed energy bin then can be used to calculate a corrected energy, as shown in Equation 6.9.

$$E_{iterated} = \frac{E_{rec}}{(1 + E_{bias})} \tag{6.9}$$

Such a correction is hindered by the dependence of the correlation between energy bias and reconstructed shower height on the reconstructed energy bin. Therefore, the correction must be applied on a bin-by-bin basis, for coarse enough bins that a reconstructed even is unlikely to fall too far from its true bin, and fine enough bins that the correction retains a reasonable degree of accuracy.

The shower maximum iteration analysis (SMI analysis) uses the shower height to correct the energy value reconstructed from a lookup table in a second-order correction. Once a reconstructed energy has been calculated from the standard lookup tables, that value is used to consult the appropriate energy bin for the applicable linear correction values between energy bias and shower height. Then, the shower height and expected energy bias from

the fit are applied to the reconstructed energy, to shift it in the appropriate direction. A flowchart describing the shower max iteration in the stage4 energy reconstruction is shown in Figure 6.12.

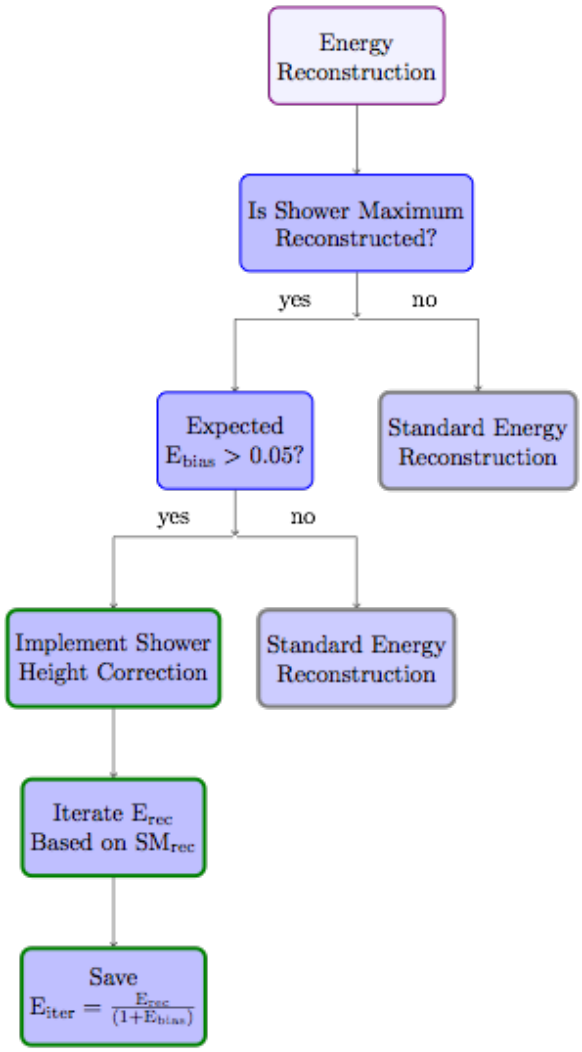

Figure 6.12 Flowchart of shower max iteration (SMI) on the energy reconstruction.

At multi-TeV energies, the tails of the distributions became non-linear for multi-TeV above about ±30% energy bias. Such extreme energy biases of greater than 30% is driven primarily by other factors, not the shower height. Therefore, multi-TeV events with an

expected bias due to shower height of greater than ±30% were excluded from the correction algorithm for energy bins above 1 TeV. For energies below about 1 TeV, however, the linear correlation is strong out to about +75% and −40% energy bias. Figure 6.13 shows this extended correlation in lower energy showers. Therefore, bins below 1 TeV were corrected for expected bias up to 75%.

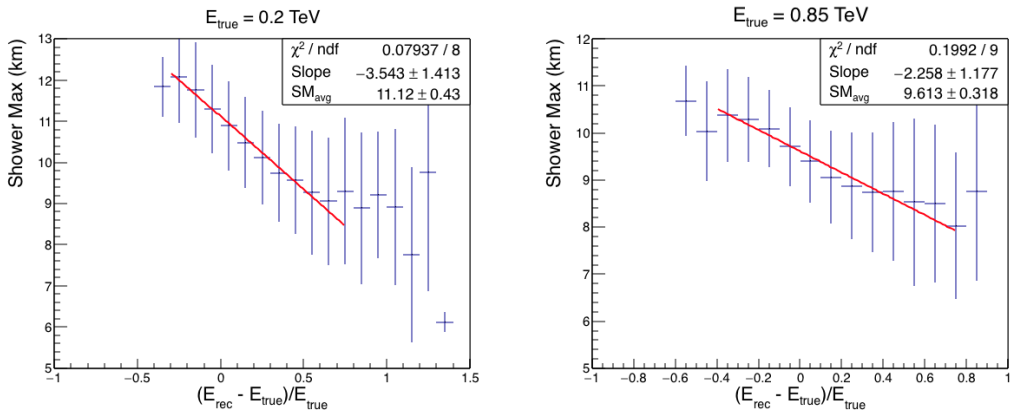

(a) (b)

Figure 6.13 Reconstructed shower height compared to energy bias of simulated events at 200 GeV and 850 GeV.

These quality exclusions brought the percentage of corrected events down to about 47% of total events with both reconstructable shower height and a good linear fit between shower height and energy bias.

6.3.3 Energy Bias Improvements with Shower Height

Applying the SMI analysis to simulated showers improves the energy bias. The improvement to overall energy bias is especially pronounced at the low energy threshold, where shower height dominates as the primary source of systematic bias. The resulting energy bias curve for these iterated events in V5 is shown in Figure 6.14.

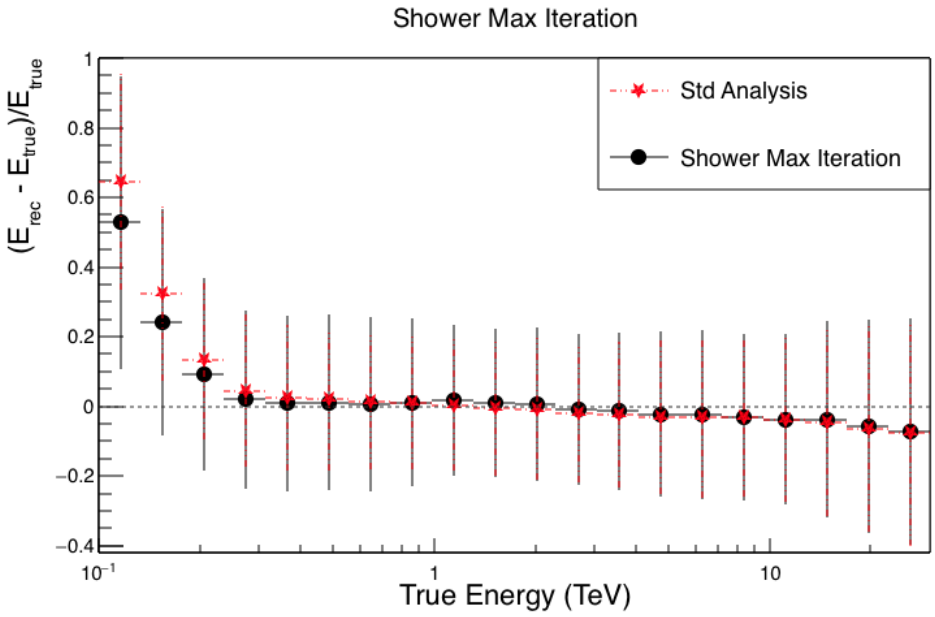

Figure 6.14 Shower max iteration effect on the energy bias.

The energy bias of all events shows only small effects across the majority of the VERITAS energy range. This is because the energy reconstruction is dominated by events for which either shower height could not be calculated, or for which the shower height fell outside the range of well-fit energy bias. To see the effect more clearly of the SMI analysis on the energy reconstruction, Figure 6.15 shows the energy bias of the SMI and standard analyses compared only for events for which energy was iterated based on shower height.

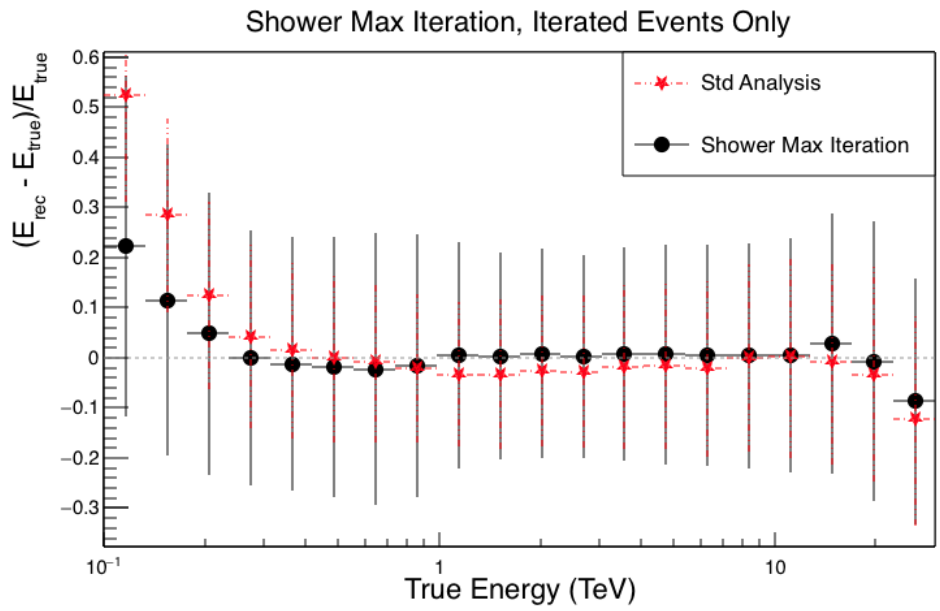

Figure 6.15 Shower max iteration effect on the energy bias, for only those events for which an accurate shower max can be calculated.

The bias curve becomes smoother across the entire VERITAS energy range from a second-order correction to reconstructed energy based on reconstructed shower maximum. The improvement is particularly significant for the low energy threshold. Bias of low energy events near threshold is decreased by a factor of 2-3 for events with reconstructable shower height and moderate expected bias.

6.4 Applying Shower Maximum to VERITAS Energy Reconstruction in V6

The studies done for V5 were reproduced on simulations from the V6 epoch. Shower height correlates with energy bias in simulations from the V6 epoch. The following subsections show the energy bias correlation and reconstructed energy with a simple iteration on the reconstructed energy with shower height for the V6 simulations. All studies were done one simulations at 20 degrees zenith angle.

6.4.1 Energy Bias and Shower Height in V6

The geometric reconstruction of an accurate shower maximum was applied to V6 simulations, and used to produce correlation plots between V6 energy bias and reconstructed shower height. Figure 6.16 shows this correlation in logarithmically spaced bins in energy between 100 GeV and 30 TeV, for four selected energies.

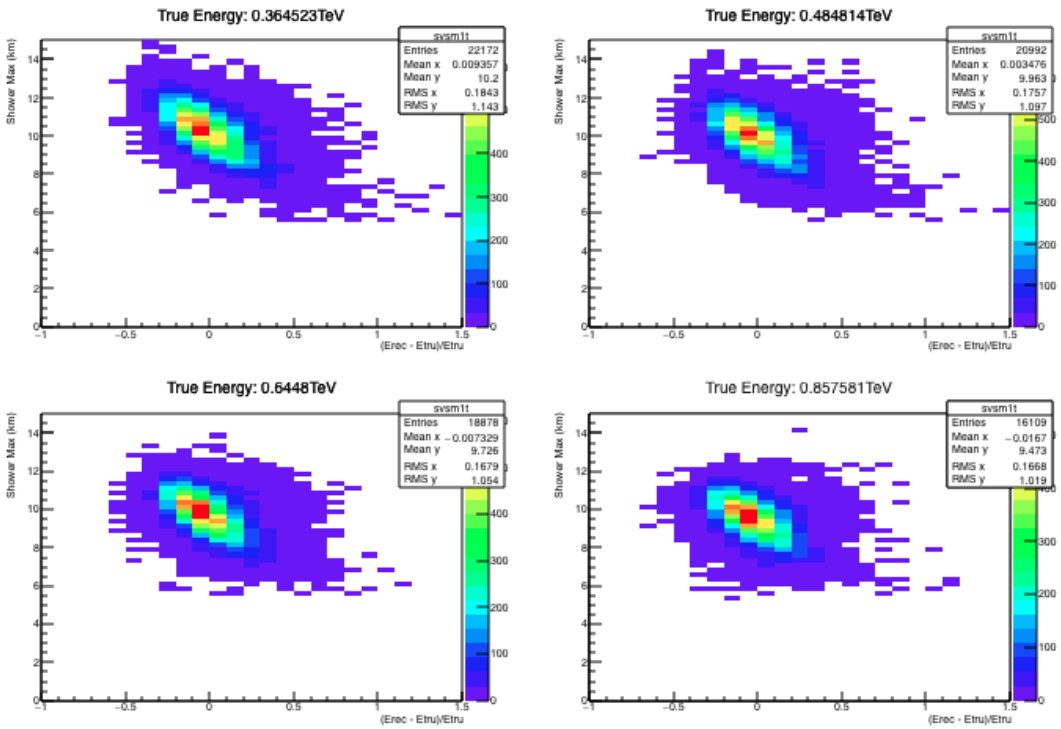

Figure 6.16 Reconstructed shower height compared to energy bias in V6 simulations. Color scale indicates number of events in each bin.

The effect of shower height on energy bias is similar in both V5 and V6 simulations. Deeper showers lead to brighter images with a positive energy bias, while showers occurring higher in the atmosphere lead to dimmer images with a negative energy bias. Figure 6.17 shows both a low and high energy shower, fit with a linear function in shower height and energy bias.

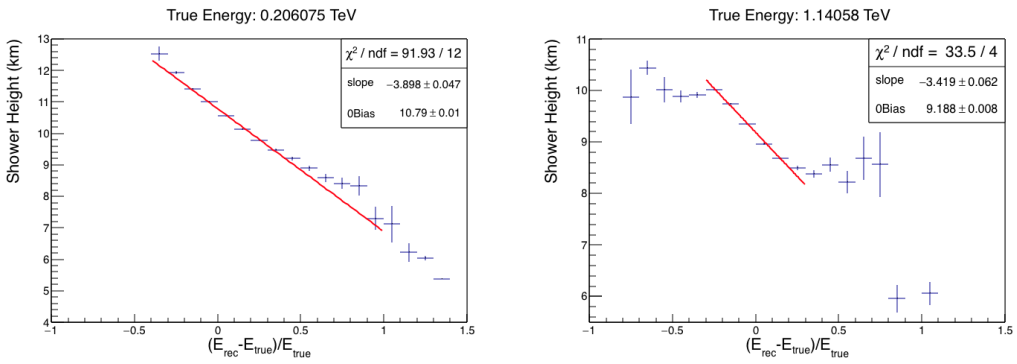

(a) (b)

Figure 6.17 Reconstructed shower height compared to energy bias of simulated events at 200 GeV and 850 GeV.

For V6 simulations, a linear fit below 1 TeV was in good agreement with the reconstructed values between about −40% and +100% expected bias. Above 1 TeV, the fits were good between ±30% expected bias out to 30 TeV.

6.4.2 Energy Bias from Shower Max Iteration in V6

The shower max iteration analysis was performed for the fits to V6 simulations at 20 degrees to zenith, similar to V5. The result of the shower max iteration on reconstructed energy is shown in Figure 6.18 for only those events whose energies were iterated. Figure 6.19 shows the effect of the shower max iteration on the set of all reconstructed events.

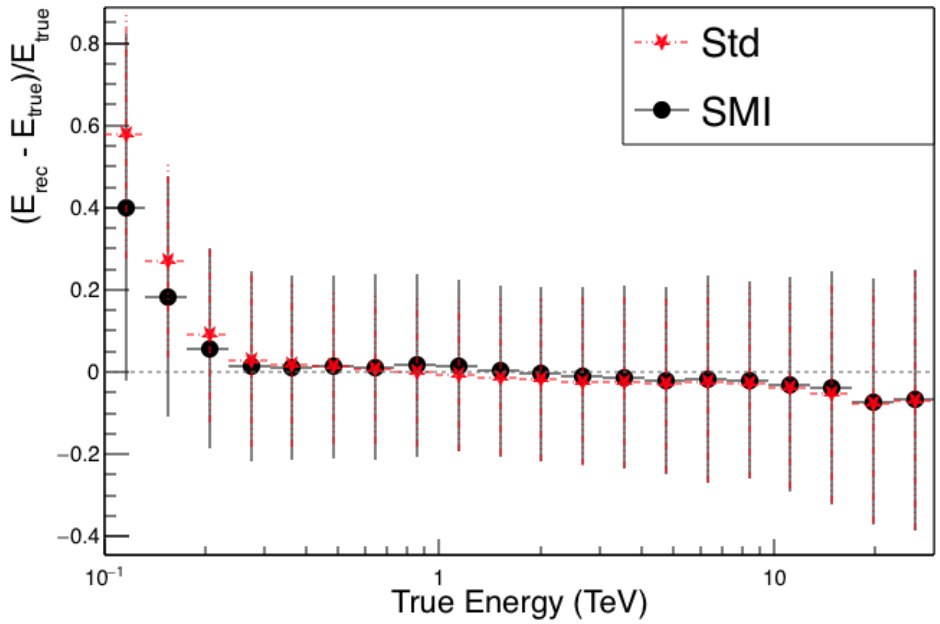

Figure 6.18 Shower max iteration effect on the energy bias.

Overall, the energy bias is improved for those events for which a reasonable shower height reconstruction exists.

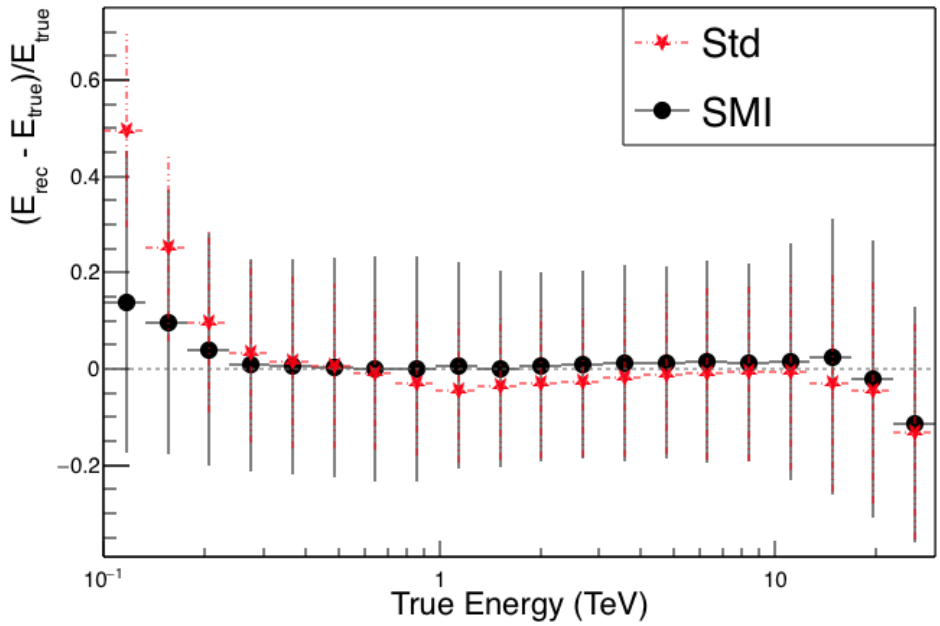

Figure 6.19 Shower max iteration effect on the energy bias, for only those events for which an accurate shower max can be calculated.

The bias curve in V6 simulations also shows prominent improvement to the average energy bias at the low energy threshold, in addition to an improved bias across the VERITAS energy range.

CHAPTER 7. THE GAMMA-RAY OPACITY OF THE UNIVERSE FROM EBL ATTENUATION

7.1 Extragalactic Background Light

All the integrated light at energies higher than those comprising the CMB, from both resolved and unresolved extragalactic sources, including potential diffuse backgrounds covering the range from IR to UV, makes up the cosmological quantity known as the extragalactic background light (EBL). Therefore, the exact shape of the EBL contains a map of cosmic evolution, from galaxies to stars to supernovae.

Much of the EBL intensity is powered by core collapse supernovae. Therefore, the total EBL intensity ties directly to the cosmological supernova rate and the expected flux of supernova neutrinos, a subject of increasing interest in the unfolding era of multi-messenger astrophysics. At a few μm wavelengths, around 15% of the EBL intensity arises from dust enshrouded AGN. The dust around these AGN can absorb and re-radiate up to 90% of the X-ray energy produced in each AGN. Therefore, the X-ray background can be used to estimate the EBL at μm intensity [18]. At mid-IR intensities, however, zodiacal light impedes our ability to directly measure the EBL intensity. Lower limits are placed by counting up resolved galaxies and integrating the total light produced. Upper limits, however, are more difficult to come by.

As discussed in Chapter 1, blazars provide a unique probe of the EBL intensity across IR wavelengths. By exploiting known physics and hardness limits on intrinsic blazar spectra, the spectra of blazars can be used to place upper limits on the density of the EBL over a range of wavelengths. These upper limits, combined with lower limits from direct galaxy

observations, narrow our uncertainty on the shape of the EBL, which provides critical insight into rates of galaxy formation, star formation, and supernovae throughout the history of our universe, which provides insight into a number of cosmological questions.

7.1.1 The Attenuation of Gamma-rays from Extragalactic Sources

As VHE photons traverse the distance between their source galaxy and our own observatories on earth, they are attenuated by EBL photons in the IR. By determining the density of EBL photons required to de-absorb an observed spectrum and regain an intrinsic spectrum of maximum physical hardness of -1.5 [18], an upper limit to the EBL density can be placed. This method is illustrated in Figure 7.1. The source blazar produces an intrinsic gamma-ray spectrum illustrated by the black curve. The gamma rays reaching earth are measured by VERITAS and reconstructed into the red spectrum, which shows the energy-dependent attenuation of gamma rays, which is stronger at higher energies. The blue shaded region between the observed and intrinsic spectra then provides a measure of the density of EBL photons between the source and earth.

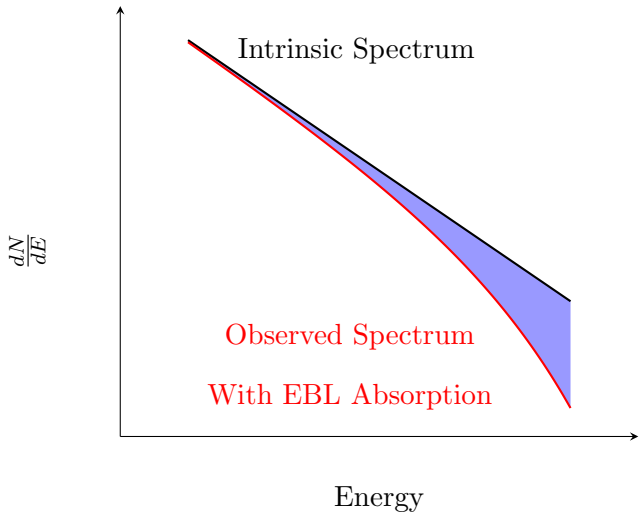

Figure 7.1 A simple model of the effects of EBL absorption on a distant blazar spectrum.

EBL and gamma-ray photon interactions may result in pair-production when the energy of the two photons in the center of momentum exceeds the energy for a particle anti-particle pair. For an $e^+ + e^-$ pair, the calculation of this threshold energy is reproduced from Chapter 1 in Equation 7.1. Here, $\mu = \cos(\theta)$, and θ is the angle between the two photons. Absorption of gamma-ray photons by EBL photons increases with both gamma-ray energy and source distance, given by redshift in z. Above a few tens of TeV, the universe becomes opaque to gamma rays. The redshift at which gamma rays from a source are fully absorbed by EBL photons decreases with increasing energy. By about $z = 1$, the universe is opaque to gamma rays above about 1 TeV [28].

$$\epsilon_{th}(E_\gamma, \mu, z) = \frac{2(m_e c^2)^2}{E_\gamma(1-\mu)} \tag{7.1}$$

The opacity of the EBL field to the gamma rays passing through it is given by integrating over $\frac{dl}{dz}$, the photon number density as a function of redshift and energy given in Equation C.3, and the interaction cross-section, $\sigma_{\gamma\gamma}$ (provided in Appendix C), relative to the EBL energy ϵ', the angle of interaction, and redshift. The full integral is shown in Equation 7.2.

$$\tau_\gamma(E_\gamma, z) = \int_0^z \int_{-1}^{1} \int_{\epsilon_{\mathrm{th}'}}^{\infty} \frac{dl}{dz} \frac{1-\mu}{2} n_\epsilon(\epsilon', z) \sigma_{\gamma\gamma}(E'_\gamma, \epsilon', \mu) d\epsilon' d\mu dz' \tag{7.2}$$

Numerical integration is required to evaluate the opacity, τ. In order to determine the distance of the blazars in the work used for this thesis, a relationship between distance and redshift is invoked following cosmological principles, for a flat ΛCDM cosmology. The terms in the integral are discussed in further detail in Appendix C.

Figure 7.2 shows typical opacities for several different redshifts, calculated from [21]. The increasing opacity with increasing gamma-ray energy is clearly seen in the positive slope of all the curves between 100 GeV and 100 TeV. The slight plateau that appears around gamma-ray energies between about 1–10 TeV is caused by the dip in the EBL intensity between about 1–15 μm [18].

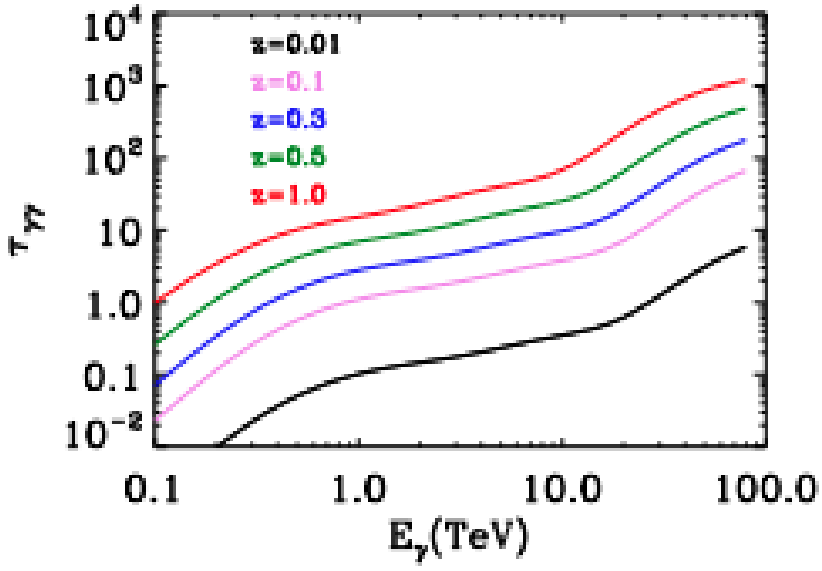

Figure 7.2 Typical values of tau at VHE energies. Opacity calculated from EBL model of [21]. Image from [18]

Once τ is calculated, the de-absorption is a simple exponential expression given in Equation 7.3.

$$\frac{\mathrm{d}N}{\mathrm{d}E} = \left(\frac{\mathrm{d}N}{\mathrm{d}E}\right)_{\mathrm{obs}} \times e^{\tau(E_\gamma, z)} \tag{7.3}$$

Typical VERITAS spectra are given as reconstructed flux per energy bin, with the width of the bin chosen during analysis. Therefore, the de-absorption of a spectrum produced by VERITAS analysis uses an average opacity value at the center of each energy bin to de-absorb an entire bin in energy. For the EBL limits this thesis is concerned with, a constant binning of 5 bins per decade in energy was used for all spectra.

7.1.2 EBL Evolution

Equation C.2 gives the EBL density at a $z = 0$. The $(1 + z)^3$ term assumes a flat expansion of the universe with no EBL evolution in z. A realistic model of EBL evolution,

however, accounts for a non-uniform galaxy evolution. To first order, this evolution can be decoupled from the density at $z = 0$ and modeled with a factor evol(z), such that $\mathrm{d}\epsilon' \frac{\mathrm{d}n}{\mathrm{d}\epsilon'}(\epsilon', z)$ goes to $\mathrm{d}\epsilon \frac{\mathrm{d}n}{\mathrm{d}\epsilon}(\epsilon, 0) \times \mathrm{evol}(z)$ [7]. This factor is given in Equation 7.4.

$$\mathrm{evol}(z) = (1 + z)^{3 - f_{\mathrm{evo}}} \tag{7.4}$$

For this work, an evolutionary factor of 1.7 was chosen as the ideal factor out to $z = 1$. The differences between the chosen f_{evo}value and the model is less than the differences between opacities in different EBL models, as can be seen in Figure C.5. The uncertainty in the value of $f_{\mathrm{evo}}$is also well within the range of other sources of statistical and systematic uncertainties.

See Appendix C for a detailed overview of the choice of f_{evo}.

7.2 Obtaining Upper Limits to EBL Density from Blazar Spectra

In order to obtain upper limits on EBL density, the method, e.g. see Raue and Mazin (2008) was followed, with some modifications.

Instead of a grid of fixed points at logarithmically spaced values of λ_{EBL}, values of νl_ν were chosen randomly and smoothly with replacement between previous upper and lower limits. From this method, a smooth set of EBL curves filling the phase space was generated between 0.18μm – 100.00μm.

These EBL curves were then used to calculate opacities to de-absorb the blazar spectra. Then Chi sq values of the resulting fits were used to weight the spectra and obtain the likelihood of a given value of νl_ν at each bin of λ. The methodology is described in further detail in Appendix B.

7.3 Application of Low Gain Systematics to EBL Upper Limits

Uncertainty in the VERITAS energy reconstruction propagates to the EBL density upper limits. Sources of systematic error produce systematic errors in the calculated EBL limits. The saturation effects discussed in Chapter 4 creates bias in two possible directions.

- Saturation of the data combined with pulses leaking out of the readout window causes an artificially softened spectrum, as more light is lost in the data than simulations. Therefore, an observed spectrum can be de-absorbed with a greater density of EBL photons, leading to a loosening of the upper limits.
- A low gain ratio in data that is too high leads to an artificially hardened spectrum. Therefore, an observed spectrum reaches the hardness limit of $\Gamma = 1.5$ more swiftly, leading to artificially tightened upper limits. In this case, the systematic bias caused by FADC saturation requires the upper limits on the EBL density to be loosened.

As demonstrated in Chapter 4, removing low gain channels from the analysis by looking only at the less bright tails of high-energy showers shows spectral softening in data from both the V5 and the V6 epoch. Further studies were done in Chapter 5, in which the low gain ratio used in standard VEGAS analysis was determined to be too high.

There are currently six blazars used for VERITAS EBL analysis with spectra extending above 8 TeV. One of these six sources, 1ES 1959+650, is a low elevation source which rarely rises above 60 degrees elevation at the VERITAS latitude. At low elevation, image brightness is strongly attenuated by the additional atmosphere through which the shower must travel. Therefore, significantly fewer images flip into low gain at multi-TeV energies in these low elevation images, and the low gain is not a significant concern. For this reason, 1ES 1959+650 was not considered in the following section on blazar analysis.

In the following section, the five remaining blazars that extend above 8 TeV are analyzed with a standard analysis and a SAM analysis. All five remaining blazars considered for the SAM analysis are high-frequency peaked BL Lac objects, or HBLs. The difference between

the spectral indices is then used to estimate the bias arising from the low gain switch in the electronics. As was done for the validation data set on the Crab Nebula in Chapter 4, all data was chosen to be good weather data at zenith angles of less than 30 degrees. Due to the decreased statistics present for several of the five sources, data was allowed to be marked as A or B weather, corresponding to perfectly clear weather, and somewhat hazy weather with no clouds, respectively.

The stringent quality cuts ensure the calculation of the systematics due to the low gain switch is as free as possible from competing sources of bias. As discussed above, low elevation (high zenith angle) images are already attenuated heavily by the atmosphere, and produce minimal bias from the low gain channels. For poor, hazy weather or cloud cover, the systematics are muddled both by the introduction of further sources of uncertainty from the weather and by increased attenuation of photons within the shower due to increased opacity of the atmosphere.

7.4 Blazar Analysis

The majority of the exposure time meeting SAM quality criteria on RGB J0710+591, 1ES 2344+514, and H1426+428 was acquired in V6. The remaining two sources, 1ES 1218+304 and 1ES 0229+200, had the majority of their data meeting SAM analysis quality criteria taken in V5.

All sources were initially analyzed with both the nominal low gain values of 6 in V5 and 5.8 in V6. The sources were then re-analyzed with the low gain ratio of 5.1 in V5 and 5.3 in V6, as determined from the data/MC studies and SAM analysis shown in Chapter 5.

7.4.1 1ES 2344+514

1ES 2344+514 was the third blazar detected at VHE energies [59]. The source is an HBL located at a redshift of $z = 0.044$. This makes it a nearby blazar; the effect of EBL absorption is expected to be very low even out to multi-TeV energies. Therefore, any bias

to the spectrum from the low gain channels should not produce a large change in the EBL upper limits.

7.4.1.1 Runlist and Analysis Notes

Approximately 18 hours of high-quality data was taken on 1ES 2344 over the course of the V5 and V6 epochs, corresponding to 65 data runs. Of these runs, 23 were taken during the V5 epoch, corresponding to approximately 6 hours of V5 data. The remaining 42 runs were taken during the V6 epoch, corresponding to approximately 12 hours of V6 data.

7.4.1.2 Spectral Analysis

The results of the spectral analysis with nominal low gain ratios are shown in Figure 7.3, and summarized in Table 7.1. The combined V5 and V6 spectral analysis of 1ES 2344+514 produces a moderately soft spectrum that extends to 4 TeV. The standard analysis is in poor agreement with the SAM analysis above 1 TeV. As expected from the results on the Crab spectral analyses in Chapter 4, the use of the SAM analysis causes the spectrum to soften above 1 TeV.

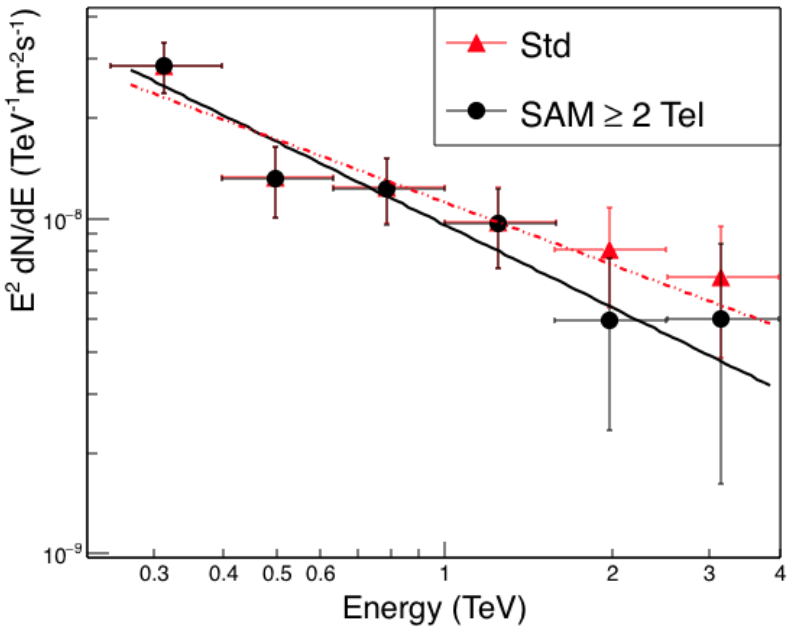

Figure 7.3 Results of the spectral analysis on the HBL 1ES2344+514, analyzed with both a standard VEGAS analysis and the SAM energy reconstruction. Low gain ratio of 6 used for V5 data, and 5.8 used for V6 data.

Table 7.1 Fit parameters for spectra obtained from the HBL 1ES2344+514, compared for a standard analysis and a SAM energy reconstruction.

	Index Γ	Norm	χ^2/ndf	Significance
SAM	2.82 ± 0.21	$0.96{\cdot}10^{-8} \pm 0.16{\cdot}10^{-8}$	2.56/3	11σ
Std	2.62 ± 0.18	$1.11{\cdot}10^{-8} \pm 0.14{\cdot}10^{-8}$	3.16/4	11.5σ

The spectral analysis with the updated low gain ratios in V5 and V6 improved the agreement between the standard analysis and the SAM analysis. The results are shown in Figure 7.4. Table 7.2 gives the spectral fit values.

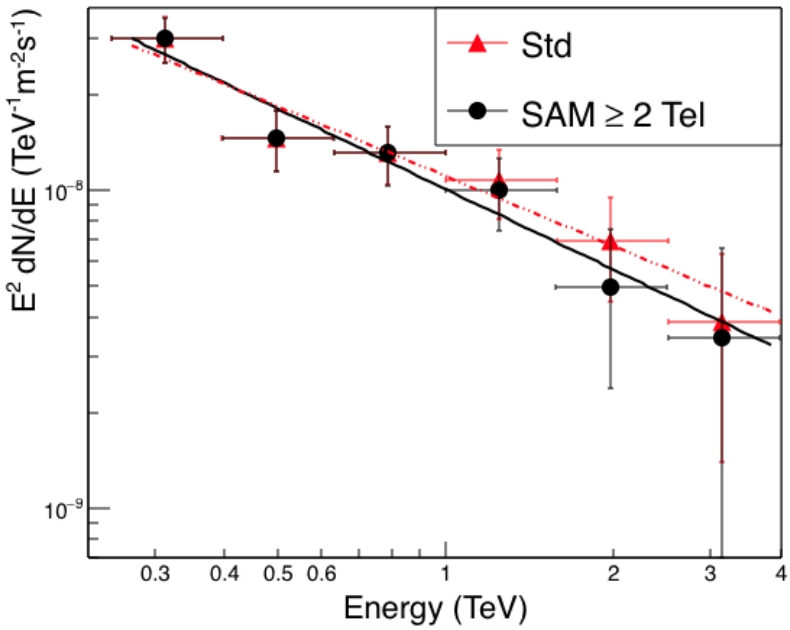

Figure 7.4 Results of the spectral analysis on the HBL 1ES2344+514, analyzed with both a standard VEGAS analysis and the SAM energy reconstruction. Low gain ratio of 5.1 used in V5, and 5.3 used in V6.

Table 7.2 Fit parameters for spectra obtained from the HBL 1ES2344+514, compared for a standard analysis and a SAM energy reconstruction.

	Index Γ	Norm	χ^2/ndf	Significance
SAM	2.84 ± 0.20	$1.01 \cdot 10^{-8} \pm 0.15 \cdot 10^{-8}$	2.3/3	11.8σ
Std	2.73 ± 0.19	$1.11 \cdot 10^{-8} \pm 0.15 \cdot 10^{-8}$	2.47/3	12.1σ

7.4.2 1ES 0229+200

1ES 0229+200 is located at a redshift of $z = 0.14$. HESS discovered 1ES 0229+200 at VHE energies in 2007, and VERITAS later observed the source between 2009–2011 for a second VHE detection [20] [59]. Since 2011, VERITAS has collected over 100 hours of

observations on 1ES 0229+200, of which approximately 80.5 hours passed quality cuts for analysis with the SAM energy reconstruction. It is a hard spectrum blazar, with a VHE power law index of approximately $\Gamma = 2.5$, and a quiescent flux of about 2% Crab between about 300 GeV and 15 TeV [59].

7.4.2.1 Runlist and Analysis Tables

Between fall 2009 and summer 2016, VERITAS collected 80.5 hours of exposure meeting the SAM quality criteria on 1ES0229+200, in 20- to 30-minute runs. Of this data, 160 20-minute runs were taken in the V5 epoch for a total of approximately 48 hours of useable exposure time. Only 80 runs were taken in the V6 epoch meeting SAM Analysis criteria. These runs were primarily 30-minute runs, however, for a total of 32.5 hours of exposure in V6. In total, 240 20- to 30-minute runs were included in the analysis presented below.

7.4.2.2 Spectral Analysis

The combined V5 and V6 spectrum of 1ES0229+200 extends out to approximately 2.5 TeV in the SAM analysis. Reconstructing the energy with the SAM analysis produces a spectrum in good agreement with the standard analysis. This result is expected due to the lack of significant energy bins above 2.5 TeV. The results of the spectral analysis with nominal low gain ratios are shown in Figure 7.5, and summarized in Table 7.3.

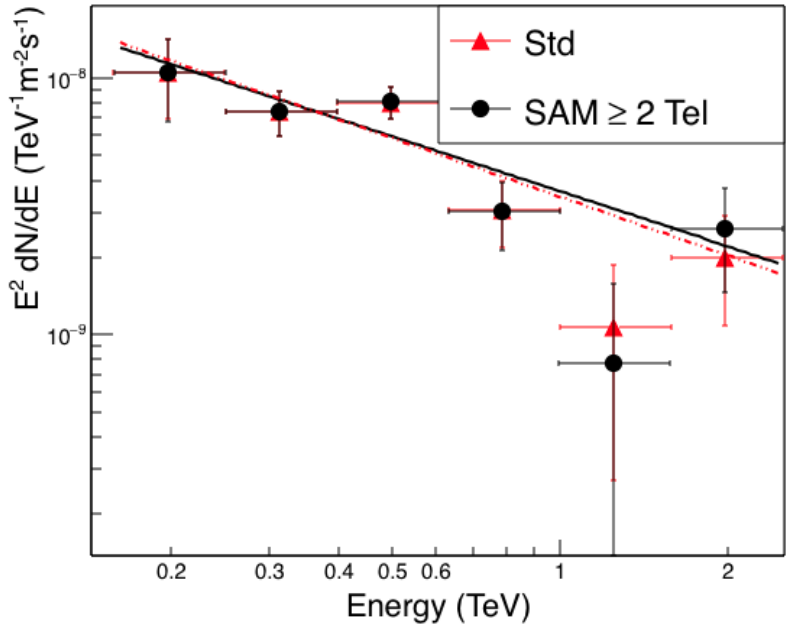

Figure 7.5 Results of the spectral analysis on the HBL 1ES0229+200, analyzed with both a standard VEGAS analysis and the SAM energy reconstruction. Low gain ratio of 6 used for V5 data, and 5.8 used for V6 data.

Table 7.3 Fit parameters for spectra obtained from the HBL 1ES0229+200, compared for a standard analysis and a SAM energy reconstruction.

	Index Γ	Norm	χ^2/ndf	Significance
SAM	2.71 ± 0.19	$3.62 \cdot 10^{-9} \pm 0.65 \cdot 10^{-9}$	5.94/3	9.99σ
Std	2.76 ± 0.18	$3.485 \cdot 10^{-9} \pm 0.59 \cdot 10^{-9}$	5.61/3	10.1σ

The spectral comparison with updated low gain ratios in V5 and V6 is shown in Figure 7.6. Table 7.4 gives the spectral fit values.

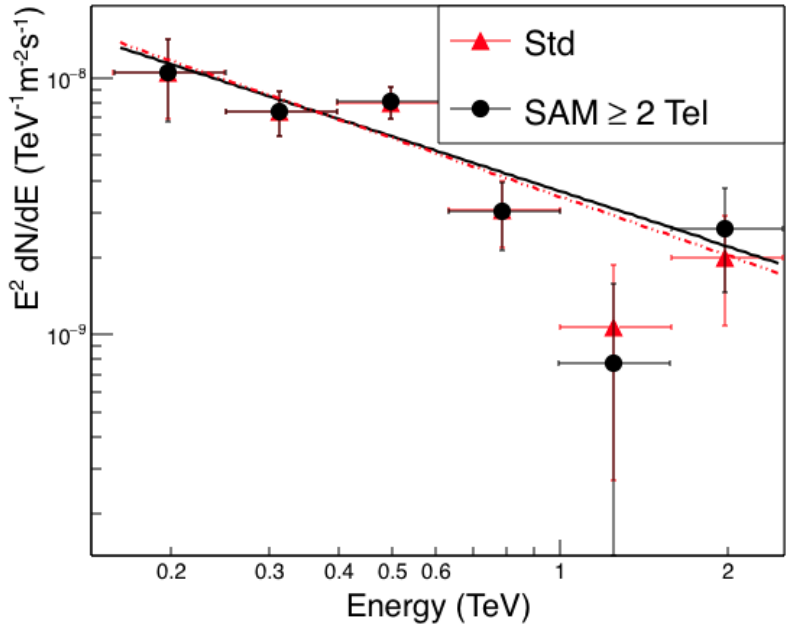

Figure 7.6 Results of the spectral analysis on the HBL 1ES0229+200, analyzed with both a standard VEGAS analysis and the SAM energy reconstruction. Low gain ratio of 5.1 used in V5, and 5.3 used in V6.

Table 7.4 Fit parameters for spectra obtained from the HBL 1ES0229+200 with updated low gain ratios, compared for a standard analysis and a SAM energy reconstruction.

	Index Γ	Norm	χ^2/ndf	Significance
SAM	2.71 ± 0.19	$3.62 \cdot 10^{-9} \pm 0.65 \cdot 10^{-9}$	5.07/3	10.2σ
Std	2.73 ± 0.22	$3.57 \cdot 10^{-9} \pm 0.77 \cdot 10^{-9}$	4.83/2	10.3σ

Though agreement between the spectral shapes was already good with the nominal low gain ratios, an analysis with updated low gain ratios improved the agreement slightly.

7.4.3 RGB J0710+591

RGBJ 0710 is an HBL located at a redshift of $z = 0.125$. It was discovered at VHE energies by the VERITAS collaboration in 2009 [59]. Both VERITAS and Fermi have observed emission from RGBJ 0710+591, with a hard emission spectrum measured by Fermi of $\Gamma = 1.5$ between 100 MeV and 300 GeV. VERITAS measures a power law spectral index of approximately $\Gamma = 2.7$ that extends out to multi-TeV energies [59].

7.4.3.1 Runlist and Analysis Notes

Between fall 2009 and fall 2018, VERITAS collected approximately 48 hours of exposure meeting the SAM quality criteria on RGB J0710+591, in 20-30 minute runs. Of this data, 65 runs, or about 18 hours, were taken in the V5 epoch. The remaining 74 runs, corresponding to 30 hours of data, were taken in the V6 epoch, for a total of 139 runs.

7.4.3.2 Spectral Analysis

The combined V5 and V6 spectrum of RGB J0710+591 extends to approximately 4 TeV in the SAM analysis. The results of the spectral analysis with nominal low gain ratios are shown in Figure 7.7, and summarized in Table 7.5. The standard and SAM analyses yield poor agreement of the spectral shapes with nominal low gain ratios. The two analysis methods produce a tension in the spectral indices greater than 1σ.

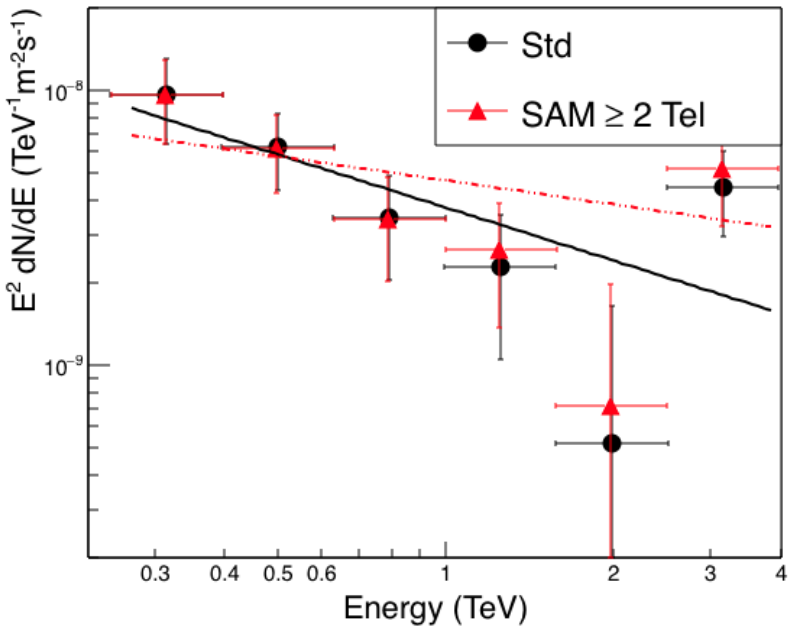

Figure 7.7 Results of the spectral analysis on the HBL RGB J0710+591, analyzed with both a standard VEGAS analysis and the SAM energy reconstruction. Low gain ratio of 6 used for V5 data, and 5.8 used for V6 data.

Table 7.5 Fit parameters for spectra obtained from the HBL RGB J0710+591 with nominal low gain ratios, compared for a standard analysis and a SAM energy reconstruction.

	Index Γ	Norm	χ^2/ndf	Significance
SAM	2.64 ± 0.45	$3.76 \cdot 10^{-9} \pm 0.94 \cdot 10^{-9}$	3.85/3	5.64σ
Std	2.29 ± 0.32	$4.72 \cdot 10^{-9} \pm 0.94 \cdot 10^{-9}$	2.67/2	5.65σ

The spectrum of RGB J0710+591 is particularly hardened in the standard analysis by the comparatively high significance of the highest energy bin.

The results of an analysis of RGB J0710 with updated low gain ratios from the Max1 comparisons is shown in Figure 7.8. The results of the spectral fits are given in Table 7.6.

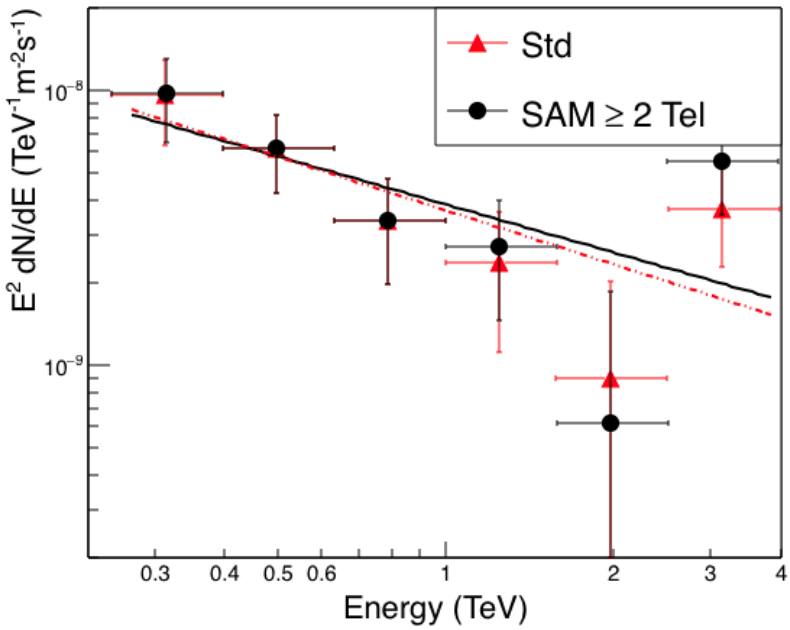

Figure 7.8 Results of the spectral analysis on the HBL RGB J0710+591, analyzed with both a standard VEGAS analysis and the SAM energy reconstruction. Low gain ratio of 5.1 used in V5, and 5.3 used in V6.

Table 7.6 Fit parameters for spectra obtained from the HBL RGB J0710+591 with updated low gain ratios, compared for a standard analysis and a SAM energy reconstruction.

	Index Γ	Norm	χ^2/ndf	Significance
SAM	2.58 ± 0.45	$3.86 \cdot 10^{-9} \pm 0.94 \cdot 10^{-9}$	4.29/3	5.68σ
Std	2.65 ± 0.40	$3.67 \cdot 10^{-9} \pm 0.85 \cdot 10^{-9}$	3.06/3	5.67σ

The spectral agreement between the standard and SAM analyses is greatly improved with the use of the updated low gain ratios.

7.4.4 1ES 1218+304

1ES 1218+308 is located at a redshift of $z = 0.182$. VHE gamma rays were first discovered from this blazar by the MAGIC collaboration in 2006 [19], and subsequently discovered by VERITAS in 2009 [54]. The quiescent flux is approximately 8% of the Crab flux at 1 TeV. Though many hours of data have been taken on 1ES 1218+304, the source is typically measured with a power law index of $\Gamma \approx 3$ in the quiescent state. Therefore, statistics decrease quickly at high energies, and the spectrum only extends to about 4 TeV in the SAM analysis.

7.4.4.1 Runlist and Analysis Tables

240 runs meeting the SAM Analysis quality requirements were taken during the V5 and V6 epochs, for a total of 80 hours of useable data. Of this, 167 runs were taken in the V5 epoch, and only 73 data runs were taken during the V6 epoch.

7.4.4.2 Spectral Analysis

The results of the spectral analysis on combined V5 and V6 data produce good agreement between the standard analysis and the SAM analysis with nominal low gain ratios. The spectral comparison with nominal low gain ratios is shown in Figure 7.9, and the results of the spectral fits are summarized in Table 7.7.

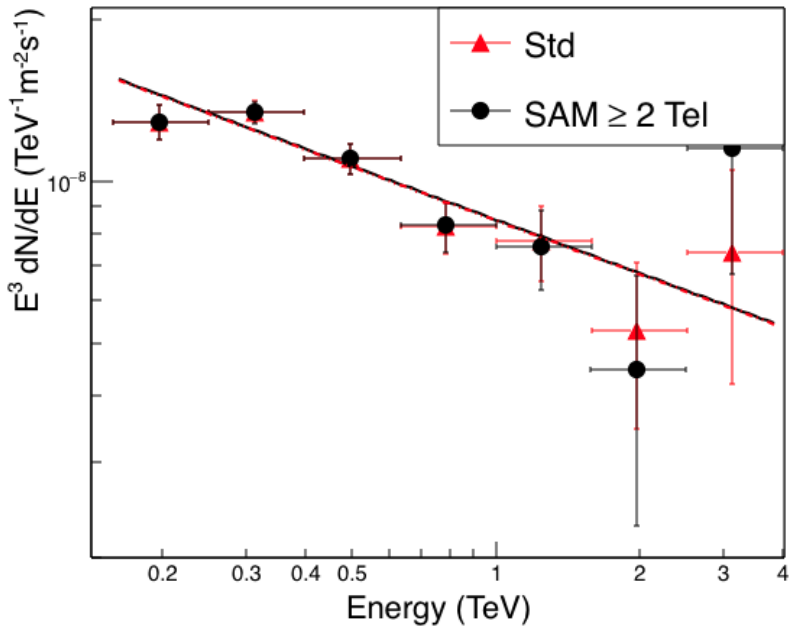

Figure 7.9 Results of the spectral analysis on the HBL 1ES1218, analyzed with both a standard VEGAS analysis and the SAM energy reconstruction. Low gain ratio of 6 used for V5 data, and 5.8 used for V6 data.

Table 7.7 Fit parameters for spectra obtained from the HBL 1ES1218+304, compared for a standard analysis and a SAM energy reconstruction.

	Index Γ	Norm	χ^2/ndf	Significance
SAM	3.33 ± 0.06	$8.49 \cdot 10^{-9} \pm 0.56 \cdot 10^{-9}$	9.21/5	46σ
Std	3.33 ± 0.06	$8.46 \cdot 10^{-9} \pm 0.53 \cdot 10^{-9}$	7.60/5	46σ

Applying the low gain ratios determined by Max1 distributions does not change the spectral shape significantly. The results of an analysis of 1ES1218+304 with updated low gain ratios from the Max1 comparisons is shown in Figure 7.10. The results of the spectral fits are given in Table 7.6.

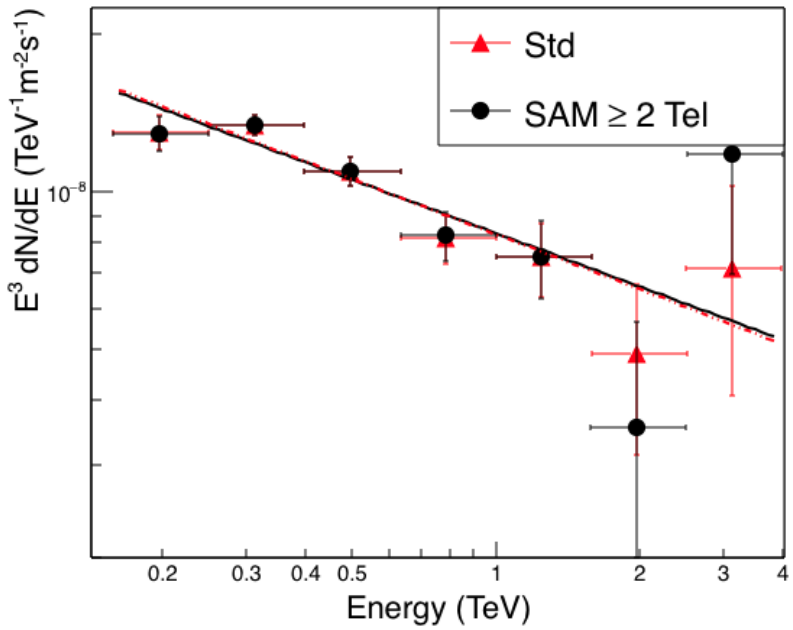

Figure 7.10 Results of the spectral analysis on the HBL 1ES1218, analyzed with both a standard VEGAS analysis and the SAM energy reconstruction. Low gain ratio of 5.1 used in V5, and 5.3 used in V6

Table 7.8 Fit parameters for spectra obtained from the HBL 1ES1218+304, compared for a standard analysis and a SAM energy reconstruction.

	Index Γ	Norm	χ^2/ndf	Significance
SAM	3.34 ± 0.06	$8.35 \cdot 10^{-9} \pm 0.55 \cdot 10^{-9}$	10.2/5	46σ
Std	3.35 ± 0.06	$8.31 \cdot 10^{-9} \pm 0.53 \cdot 10^{-9}$	7.63/5	46σ

The spectral shapes remain in excellent agreement when analyzed with the updated low gain ratios. The index changes negligibly.

7.4.5 H 1426+428

The first detection of VHE emission from H1426+428 came from the Whipple 10-m in 2002 [39]. It is located at a moderate redshift of $z = 0.129$. The Whipple detection showed H1426+428 to be a soft spectrum blazar, with an index of $\Gamma = 3.55$ [39]. In this work, both the standard VEGAS analysis and the SAM analysis with nominal low gain ratios produce a power law index of about $\Gamma = 2.7$.

7.4.5.1 Runlist and Analysis Tables

There are 156 SAM-quality data runs for H1426, corresponding to 58 total hours of high-quality, high elevation exposure. Of these, 71 runs were taken during the V5 epoch for approximately 13 hours of exposure, and 85 runs were taken during the V6 epoch for approximately 45 hours of exposure.

7.4.5.2 Spectrum

The combined V5 and V6 spectrum of H1426+428 extends out to 2.5 TeV. Reconstructing the energy with the SAM analysis produces a spectrum slightly harder than the spectrum produced by the standard analysis. The results of the spectral analysis are shown in Figure 7.11, and summarized in Table 7.9.

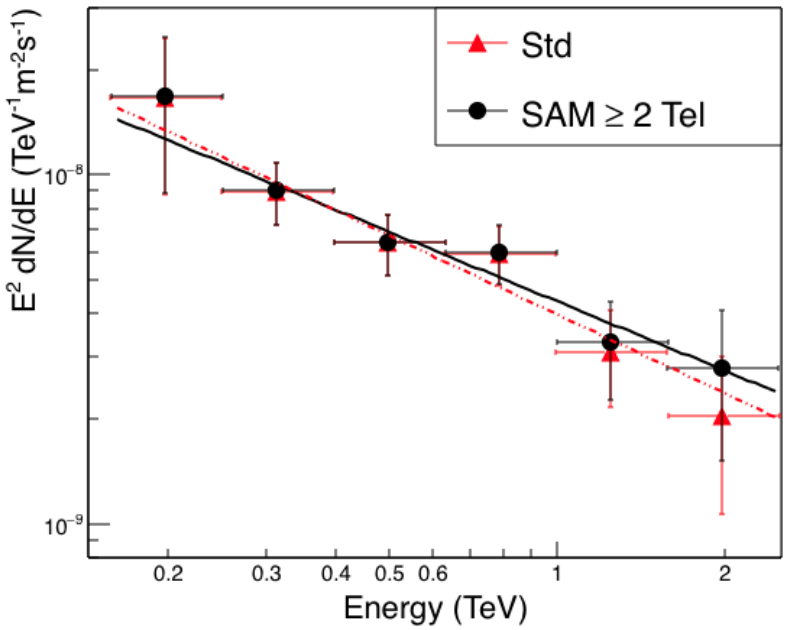

Figure 7.11 Results of the spectral analysis of the blazar H1426+428, analyzed with both a standard VEGAS analysis and the SAM energy reconstruction. Low gain ratio of 6 used for V5 data, and 5.8 used for V6 data.

Table 7.9 Fit parameters for spectra obtained from the blazar H1426+428, compared for a standard analysis and a SAM energy reconstruction.

	Index Γ	Norm	χ^2/ndf	Significance
SAM	2.66 ± 0.18	$4.34 \cdot 10^{-9} \pm 0.63 \cdot 10^{-9}$	1.25/4	10.7σ
Std	2.75 ± 0.17	$3.98 \cdot 10^{-9} \pm 0.57 \cdot 10^{-9}$	1.55/4	10.7σ

H 1426+428 and 1ES0229+200 are the only two EBL sources analyzed in this chapter for which the SAM analysis produces a harder spectrum than the standard analysis.

The results of an analysis of H 1426+428 with updated low gain ratios from the Max1 comparisons is shown in Figure 7.12. The results of the spectral fits are given in Table 7.10.

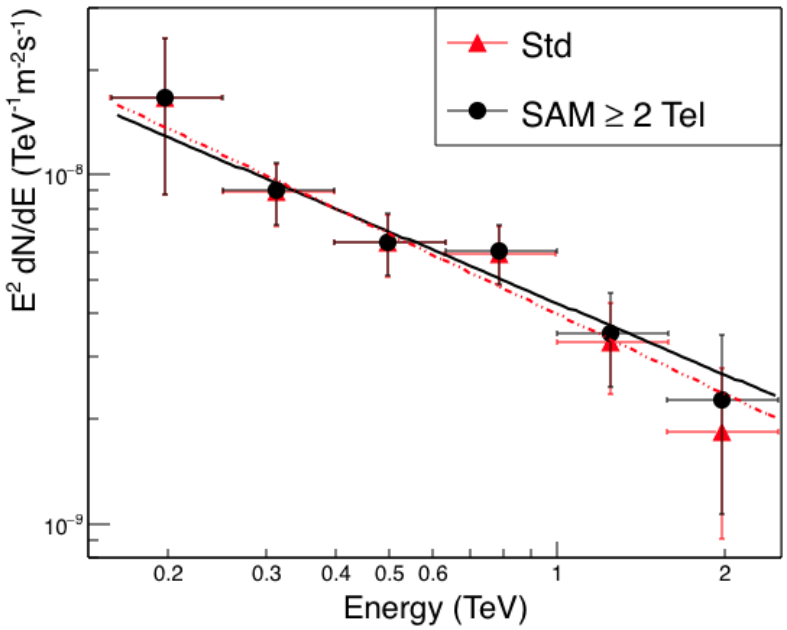

Figure 7.12 Results of the spectral analysis of the blazar H1426+428, analyzed with both a standard VEGAS analysis and the SAM energy reconstruction. Updated low gain ratios of 5.1 in V5 and 5.3 in V6 were used in spectral analysis.

Table 7.10 Fit parameters for spectra obtained from the blazar H1426+428, compared for a standard analysis and a SAM energy reconstruction.

	Index Γ	Norm	χ^2/ndf	Significance
SAM	2.68 ± 0.18	$4.29 \cdot 10^{-9} \pm 0.62 \cdot 10^{-9}$	1.29/4	10.7σ
Std	2.76 ± 0.17	$3.99 \cdot 10^{-9} \pm 0.56 \cdot 10^{-9}$	1.74/4	10.7σ

Applying the low gain ratios determined by Max1 distributions has little effect on spectral agreement, which is expected when the spectrum only extends to 2.5 TeV.

7.5 Effects from Saturation Bias on EBL Density Upper Limits

The TeV spectrum of five high elevation VERITAS blazars extends above 2–3 TeV in a SAM analysis. Data was selected for each of the five blazars to maximize saturation effects and minimize competing bias. With these criteria applied to the datasets, three of the five sources extend to approximately 2.5 TeV, and the remaining two extend to approximately 4 TeV in a VEGAS analysis with both a standard and a SAM energy reconstruction.

Only RGB J0710+591 and 1ES2344+514 showed a difference in measured spectral index greater than 1 σ between an analysis with a standard energy reconstruction and a SAM energy reconstruction, when analyzed with nominal low gain ratios. The use of the updated low gain ratios determined in Chapter 5 in analysis brought the disagreement between the spectral indices of a standard and a SAM analysis to less than 1 σ for both sources.

None of the five sources analyzed in this chapter showed significant spectral hardening in the SAM analysis over the standard analysis, when the updated low gain ratios were implemented. For these reasons, the systematic bias from low gain channels is expected to be minimal in the calculation of EBL constraints from VERITAS blazars.

CHAPTER 8. DISCUSSION AND CONCLUSIONS

Analysis of VERITAS data is complicated by systematics that affect the energy reconstruction. This bias, measured as the relative difference between measured energy and true energy, $(E_{True} - E_{Rec})/E_{True}$, should be as close to zero as possible in an ideal analysis. In data, bias arises from multiple sources, from variations in the shower physics to limitations of the detector.

The primary purpose of this thesis was to investigate and quantify the effect on the energy reconstruction arising from saturation of the FADC electronics in low gain mode. The SAM analysis, described in Chapter 4, was developed as an unbiased method of investigating this saturation bias. Validation of the SAM analysis on data from the Crab nebula revealed an improper handling of the low gain switch, which was further investigated in Chapter 5.

The results of these studies are summarized in Section 8.1. The studies in Chapter 5 determine the correct low gain ratio to apply in a VERITAS analysis, and the bias from saturation of FADC electronics in low gain mode is shown to be on the order of a few percent on the spectral reconstruction out to energies above 15 TeV when the corrected low gain ratios are implemented in the analysis. Section 8.2 summarizes the results the application of the SAM analysis and the corrected low gain ratios to five TeV blazars.

Lastly, the results of a separate analysis method designed to investigate systematics arising from variations in shower height are discussed in Section 8.3.

8.1 FADC Bias in the Low Gain Mode

The low gain switch extends the dynamic range of the electronics and thus the energy range over which VERITAS cameras can collect light before saturation. However, the handling of the low gain switch in both simulations and analysis can create three potential biases on energy spectra:

1. The high-low gain switch can cause a discontinuity in the dc spectrum if it is not handled correctly. A mismatch in the ratio of high to low gain between the ratio in data and the ratio used during analysis creates a fundamentally non-physical discontinuity in the energy bias arising immediately at the low gain switch and causes an offset in the dc spectrum across the entire dynamic range of the low gain. This effect can cause reconstructed spectra above a few TeV to artificially harden in an analysis which applies too high of a ratio, or to artificially soften in an analysis which applies too low of a ratio.
2. Low gain channels can saturate due to the pulse shape not being correctly modeled in the Monte Carlo simulations. This saturation causes a negative energy bias, because the simulations recover more light in low gain channels than the data. This effect leads to artificial softening of reconstructed spectra above several TeV, and becomes more pronounced with increasing energy.
3. Low gain channels also reach the limit of their dynamic range level and saturate from extremely bright showers of energies of approximately 10 TeV and greater. This leads to a bias at the highest energy range of spectra reconstructed from VERITAS data. This bias leads to artificial softening of spectra reconstructed above approximately 10 TeV.

The SAM analysis was developed to address the question of saturation in the low gain channels by not including images in the energy reconstruction if they fell in the bright core region of the shower for showers initiated by multi-TeV gamma rays. These images were

determined in Chapter 4 to contain a significant portion of total light in the image in low gain channels. For this reasons, the SAM analysis largely avoids issues of saturation of low gain channels, and is only moderately affected by the choice of low gain ratio. Therefore, it provides a useful validation tool for assessing the low gain ratio, saturation in the low gain from data/MC mismatch, and FADC saturation in the low gain mode. It serves as an alternative analysis for assessing the bias arising from each of these quantities in a standard VERITAS analysis.

Each of the three possible sources of bias from low gain channels will either harden or soften spectra measured above a few TeV with a VERITAS analysis. The SAM analysis provides a method for measuring the spectral shape using only images that are not biased by the low gain. Therefore, a spectrum reconstructed from a SAM analysis will be harder than the same spectrum reconstructed from a standard analysis at multi-TeV energies, if the primary bias arises from either saturation effects in low gain channels or from analysis using a high to low gain ratio set below the true value of the ratio. If the primary bias arises from a high to low gain ratio set above the true ratio, the SAM analysis will reconstruct a softer spectrum than the standard analysis method at multi-TeV energies.

The following sections present the results and conclusions drawn from the application of the SAM analysis to data from the Crab Nebula and five high-energy blazars.

8.1.1 The VERITAS Low Gain Ratio

In the initial validation of the SAM analysis using observations from the Crab Nebula taken during both the V5 and V6 epochs, the SAM analysis had the effect of softening the spectral shapes above a few TeV over the spectra reconstructed with a standard analysis. The energy reconstructed code was tested thoroughly on MC simulations, to show that the SAM analysis accurately reconstructs simulated spectra with artificially forced saturation (see Appendix A). A softer spectrum in the SAM analysis therefore indicated that the low

gain ratios were set too high in the standard analysis, and occurred in the independent analysis of both epochs.

The dc distribution of Max1 was determined to be an excellent method for testing the low gain ratio. A non-physical discontinuity occurs in this distribution when the ratio applied to measured dc during analysis does not match the ratio applied to data by the electronics. This is shown in Chapter 5. Below the low gain switch, the distributions of data and MC simulations match. Above the switch, the distribution of Max1 in data jumps above the simulated distribution for an applied ratio above the true ratio and drops below the simulated distribution for an applied ratio below the true ratio. This effect is also seen in the distributions of Max2 and Max3, as demonstrated in Appendix A.

This non-physical, discontinuous bias arises as soon as any channels in an image used for energy reconstruction switch into low gain, and it affects the entire dynamic range of the low gain mode. In V5, the low gain switch occurs at approximately 700 dc. This Max1 dc value is reached in V5 in images of showers with energy around 1–2 TeV. In V6, the low gain switch occurs at approximately 900 dc. This Max1 dc value is also reached in V6 in images of showers with energy around 1–2 TeV.

The application of the nominal values of the low gain ratio in analysis of V5 and V6 data produces a jump in the Max1 distribution above the switch. Above the jump, for a low gain channel in data and simulations with the same measured dc, the dc in data is multiplied by too high a value during analysis and thus biases the reconstructed energy towards higher energies. This leads to a loss of reconstructed events in the energy regime immediately above the switch and too many reconstructed events in energy bins above the jump.

The low gain ratio in V5 produces the best agreement between data/MC at 5.1. The best data/MC agreement in V6 is achieved with a low gain ratio of 5.3.

8.1.2 Low Gain Ratio Validation with the SAM Analysis

Chapter 4 describes the development and validation of the SAM analysis. Chapter 5 reapplies the SAM analysis to data from the Crab Nebula, analyzed with the updated low gain ratios for V5 and V6. Rerunning the SAM and standard analyses on V5 and V6 Crab Nebula data with the decreased low gain ratios produced well-matched spectra both between epochs and between analyses. This match further indicates that, with the use of the correct value of the low gain ratio in analysis, the systematic bias due to the mismatch between real and simulated low gain pulses is a only a small contribution to energy bias and spectral reconstruction.

The SAM analysis and both sets of low gain ratios were also used in the analysis of the five blazar sources discussed in Chapter 7. The results of these analyses and the Crab Nebula validation are summarized in Table 8.1. The power law index is given for each source, for the the standard and SAM analyses with each low gain ratio. The nominal low gain ratios of 6 in V5 and 5.8 in V6 are denoted with the subscript "nominal", while the updated low gain ratios of 5.1 in V5 and 5.3 in V6 are denoted with the subscript "updated".

Table 8.1 Summary of spectral indices for five blazar sources fit to the full observed energy range, and the Crab Nebula power law spectral indices above 1 TeV, obtained from standard VERITAS analysis and a SAM analysis with both nominal and updated low gain ratios in V5 and V6.

Source	$\Gamma_{\text{Std\_nominal}}$	$\Gamma_{\text{Std\_updated}}$	$\Gamma_{\text{SAM\_nominal}}$	$\Gamma_{\text{SAM\_updated}}$	Energy Range (TeV)
V5 Crab	2.59 ± 0.02	2.69 ± 0.02	2.64 ± 0.03	2.67 ± 0.03	1–25
V6 Crab	2.64 ± 0.03	2.74 ± 0.03	2.71 ± 0.04	2.74 ± 0.04	1–25
1ES2344+514	2.62 ± 0.18	2.73 ± 0.19	2.82 ± 0.21	2.84 ± 0.20	0.25–4
1ES0229+200	2.76 ± 0.18	2.73 ± 0.22	2.71 ± 0.19	2.71 ± 0.19	0.16–2.5
RGB J0710+591	2.29 ± 0.32	2.65 ± 0.40	2.64 ± 0.45	2.58 ± 0.45	0.25–4
1ES1218+304	3.33 ± 0.06	3.35 ± 0.06	3.33 ± 0.06	3.34 ± 0.06	0.16–4
H 1424+428	2.75 ± 0.17	2.76 ± 0.17	2.66 ± 0.18	2.68 ± 0.18	0.16–2.5

For all Crab spectra, the use of nominal low gain ratios in V5 and V6 leads to harder spectral shapes in the standard analysis than in the SAM analysis. For the majority of the spectra analyzed, the choice of the lowered ratios leads to improved agreement between the standard and the SAM analysis. Both the data/MC comparisons of Max1 and the SAM analysis provide strong evidence that the correct low gain ratios to use in VERITAS analysis are 5.1 in V5 and 5.3 in V6.

The SAM analysis provides an excellent method for cross-checking the value of the low gain ratio. Due to the choice of only unbiased telescopes for the energy reconstruction in the SAM analysis, a choice of the low gain ratio that is poorly matched to the real value in data shows up in the comparison between SAM and standard spectra at high energies. In a standard analysis that uses a value that is too high, the spectrum is hardened above the SAM analysis spectrum. With the correct choice of low gain ratio, the SAM analysis agrees well with the standard VERITAS analysis.

In Monte Carlo simulations, events above 1–2 TeV show an energy bias which increases with increasing energy, on the order of 5–10% between 2–30 TeV. The SAM analysis, however, shows that the actual effect of saturation in low gain channels produces a less than 1 σ affect on the spectral reconstruction out to energies greater than 15 TeV. The greater systematic effect arises from the handling of the low gain ratio. The use of the nominal values of ratios in V5 and V6 biases the spectral reconstruction towards harder spectral shape above approximately 1 TeV. The bias leads to a difference of about $\Delta(\alpha) \approx 0.1$ on the power law spectral index of the Crab Nebula above 1 TeV. The statistical error on the reconstructed index of the Crab Nebula above 1 TeV is only $\Delta(\alpha) = 0.02$. The systematic bias from the use of nominal low gain ratios in analysis of the high energy portion of a high statistics spectrum such as the Crab Nebula is therefore approximately a factor of 5 times greater than the statistical error.

The use of the corrected low gain ratios in analysis of Crab data produces a bias well in line with the statistical error of $\Delta(\alpha) \approx 0.02$. Therefore, the FADCs are a good fit to

the VERITAS energy range. Switching to low gain channels when the high gain saturates works well at reconstructing spectra up to 20–30 TeV.

8.2 EBL Upper Limits

Only multi-TeV air-showers arriving from within a few tens of degrees from zenith lead to significant saturation in the VERITAS cameras. Therefore, only those blazars with observations above 60 degrees and multi-TeV spectra measured from a standard VERITAS analysis were considered for spectral reconstruction with the SAM analysis. Five blazars at low to moderate redshifts fit all these critera; their analysis is presented in Chapter 7, and the results of the spectral fits are summarized in the previous section.

Of these five blazars, only RGB J0710+591 and 1ES2344+514 showed a change in spectral index of approximately 1 σ between the choice of nominal or decreased low gain ratios in a standard analysis. RGB J0710+519 and 1ES2344+514 were also the only EBL sources with approximately 1 σ difference in the spectral index of a standard and SAM analysis using nominal low gain ratios. All other sources had less than 1 σ difference in spectral indices between analyses with respect to energy reconstruction and choice of low gain ratios.

None of the five blazar spectral analyses extended above 4 TeV in a SAM analysis with either set of low gain ratios. This, combined with the small variations in spectral index due to choice of low gain ratio for three of the five sources, indicates a negligible bias on EBL upper limits due to FADC saturation or the handling of the low gain ratios.

8.3 Shower Maximum Iteration

In addition to bias at high energies from the low gain switch, another bias is introduced by the shower physics and variations in showers at all energies. Each gamma-ray induced air shower has an expected penetration depth into the atmosphere and height of shower maximum that is dependent on initial gamma ray energy. However, this quantity has high

statistical variation, which leads to showers of the same energy penetrating to a broad range of atmospheric depths, with the average value occurring at the expected value for that energy. Therefore, including shower height in the energy reconstruction should lead to improved energy bias and improved energy resolution.

The Shower Maximum Iteration (SMI) performs a second-order correction to the energy reconstruction accounting for reconstructed shower height. This iteration method does a second-order correction to the energy reconstruction in order to account for shower height in reconstructed energy.

In particular, the sharp upturn in energy bias at the low energy threshold of the VERITAS energy range is largely driven by variations in shower maximum. As initial gamma-ray energy decreases, showers become dimmer. At the low energy threshold, showers are no longer bright enough to trigger the detector. However, due to the statistical fluctuations in shower maximum, low energy showers which develop deeper than average in the atmosphere still produce bright enough showers to trigger the detector. Because those showers which trigger the detector are brighter than an average shower of that energy, however, their size overlaps with the size of higher energy showers, and for the majority of showers $E_{Rec} > E_{True}$. As initial energy decreases, this feature becomes more pronounced.

Adding shower maximum to the energy reconstruction improves bias across the whole energy range. The most dramatic improvement, however, is seen at the low energy threshold. The SMI analysis was not fully implemented and applied to data in this thesis, but the effect on the energy bias of simulations is promising.

BIBLIOGRAPHY

[1] A. A. Abdo. Fermi large area telescope observations of Markarian 421: The missing piece of its spectral energy distribution. *Astrophys. J.*, 736:131, 2011.

[2] F. Aharonian. Observations of the Crab Nebula with HESS. *Astronomy & Astrophysics*, 457:899–915, 2006.

[3] F. Aharonian. The H.E.S.S. Survey of the Inner Galaxy in Very High-energy Gamma-rays. *Astrophys. J.*, 636:777–797, 2006.

[4] E. Aliu. A search for enhanced very high energy gamma-ray emission from the 2013 march crab nebula flare. *Astrophysical Journal Letters*, 781(1), 2013.

[5] R. Beck and R. Wieblinski. Magnetic fields in the milky way and in galaxies. Feb 2018.

[6] K. Bernlohr. Impact of atmospheric parameters on the atmospheric cherenkov technique. *Astroparticle Physics*, 12:255–268, Jan 2000.

[7] J. Biteau and D. A. Williams. The extragalactic background light, the hubble constant, and anomalies: Conclusions from 20 years of tev gamma-ray observations. *The Astrophysical Journal*, 812(1):60, 2015.

[8] P. M. S. Blackett. *Phys. Abst.*, 52:4347, 1949.

[9] S. D. Bloom and A. P. Marscher. An analysis of the synchrotron self-compton model for the multi–wave band spectra of blazars. *ApJ*, 461:657, Apr 1996.

[10] G. Breit and J. A. Wheeler. Collision of two light quanta. *Phys. Rev.*, 46:1087–1091, Dec 1934.

[11] J. Cronin. Cosmic rays at the energy frontiers. *Sci. Am.*, 276:44–49, Jan 1997.

[12] J. H. D. Berge, S. Funk. Background modeling in very-high-energy gamma-ray astronomy. *Astronomy & Astrophysics*, 466(3):1219–1229, 2007.

[13] M. Daniel. The veritas standard data analysis. 3:1325, 10 2007.

[14] M. K. Daniel. Application of radiosonde data to veritas simulations. *Proceedings of the 30th International Cosmic Ray Conference*, pages 1329–1332, 2007.

[15] M. Davies and E. Cotton. Design of the quartermaster solar furnace. *Journal of Solar Energy*, 1:16–22, 1957.

[16] A. Domínguez. Extragalactic background light inferred from aegis galaxy-sed-type fractions. *Monthly Notices of the Royal Astronomical Society*, 410(4):2556–2578, 2011.

[17] E. Dwek. The COBE Diffuse Infrared Background Experiment Search for the Cosmic Infrared Background. IV. Cosmological Implications. *APJ*, 508:106–122, Nov. 1998.

[18] E. Dwek and F. Krennrich. The Extragalactic Background Light and the Gamma-ray Opacity of the Universe. *Astropart. Phys.*, 43:112–133, 2013.

[19] f. t. M. C. E. Albert. Discovery of very high energy gamma rays from 1es 1218+30.4. *The Astrophysical Journal*, 642:L119–L122, May 2006.

[20] f. t. H. C. F. Aharonian. New constraints on the mid-ir ebl from the hess discovery of vhe ?-rays from 1es 0229+200. *A & A*, 475:L9–L13, Sept 2007.

[21] J. D. Finke, S. Razzaque, and C. D. Dermer. Modeling the Extragalactic Background Light from Stars and Dust. *Astrophys. J.*, 712:238–249, Mar. 2010.

[22] A. Franceschini, G. Godighiero, and M. Vaccari. Extragalactic optical-infrared background radiation, its time evolution and the cosmic photon-photon opacity. *A& A*, 487(3):837–852, 2008.

[23] I. Frank and I. Tamm. *Coherent Visible Radiation of Fast Electrons Passing Through Matter*, pages 29–35. Springer Berlin Heidelberg, Berlin, Heidelberg, 1991.

[24] T. K. Gaisser, R. Engel, and E. Resconi. *Cosmic Rays and Particle Physics*. Cambridge University Press; 2nd Edition, Cambridge, 2016.

[25] W. Galbraith and J. V. Jelley. Light pulses from the night sky associated with cosmic rays. *Nature*, 171:349–350, 1953.

[26] K. Gibbs. The veritas atmospheric cherenkov telescopes: Positioner, optics, and associated components. *Proceedings of the 28thth International Cosmic Ray Conference*, 5:2823–2826, 2003.

[27] R. C. Gilmore. Semi-analytic modelling of the extragalactic background light and consequences for extragalactic gamma-ray spectra. *Monthly Notices of the Royal Astronomical Society*, 422(4):3189–3207, 2012.

[28] R. J. Gould and G. P. Schréder. Opacity of the universe to high-energy photons. *Phys. Rev.*, 155:1408–1411, Mar 1967.

[29] R. J. Gould and G. P. Schréder. Pair production in photon-photon collisions. *Phys. Rev.*, 155:1404–1407, Mar 1967.

[30] P. K. F. Greider. *Extensive Air Showers: High Energy Phenomena and Astrophysical Aspects*. Springer, New York, 2010.

[31] K. Greissen. Cosmic ray showers. *Annual Review of Nuclear Science*, 10:63–108, 1960.

[32] D. Heck, J. Knapp, J. N. Capdevielle, G. Schatz, and T. Thouw. CORSIKA: A Monte Carlo code to simulate extensive air showers, 1998.

[33] V. Hess. On the observations of the penetrating radiation during seven balloon flights. *Phys. Z.*, 13:1084, 1912.

[34] A. M. Hillas. The sensitivity of cerenkov radiation pulses to the longitudinal development of cosmic-ray showers. *Journal of Physics G: Nuclear Physics*, 8(10):1475, 1982.

[35] A. M. Hillas. Cerenkov light images of EAS produced by primary gamma. *International Cosmic Ray Conference*, 3, Aug. 1985.

[36] A. M. Hillas. The spectrum of tev gamma rays from the crab nebula. *The Astrophysical Journal*, 503(2):744–759, 1998.

[37] J. Holder. The first veritas telescope. *Astroparticle Physics*, 25:391–401, 2006.

[38] J. Holder. Veritas: Hawc's neighbour to the north. 2015.

[39] D. Horan. Detection of the bl lacertae object h1426+428 at tev gamma-ray energies. *The Astrophysical Journal*, 571:753–762, Jun 2002.

[40] P. A. Čerenkov. Visible radiation produced by electrons moving in a medium with velocities exceeding that of light. *Phys. Rev.*, 52:378–379, Aug 1937.

[41] J. V. Jelley and N. A. Porter. Čerenkov Radiation from the Night Sky, and its Application to Gamma-Ray Astronomy. *Quarterly Journal of the Royal Astronomical Society*, 4:275, Sept. 1963.

[42] F. Jordan, P. & Krennrich. The design of light concentrators for a 12 m cherenkov telescope. 2004.

[43] F. Krennrich. Stereoscopic observations of gamma rays at the whipple observatory. *Astroparticle Physics*, 8(4):213 – 221, 1998.

[44] G. Lafferty and T. Wyatt. Where to stick your data points: The treatment of measurements within wide bins. *Nuclear Instruments and Methods in Physics Research Section*

A: Accelerators, Spectrometers, Detectors and Associated Equipment, 355:541–547, Feb 1995.

[45] T.-P. Li and Y.-Q. Ma. Analysis methods for results in gamma-ray astronomy. *apj*, 272:317–324, Sept. 1983.

[46] A. Madhavan. *The VHE Gamma-ray Spectra of Several Hard-spectrum Blazars from Long-term Observations with VERITAS Telescope Array*. PhD thesis, Iowa State University, 2013.

[47] Mohanty, G. Measurement of tev gamma-ray spectra with the cherenkov imaging technique. *Astroparticle Physics*, 9:15–43, 1998.

[48] N. Park. Performance of the veritas experiment. *Proceedings of the 34th International Cosmic Ray Conference*, 2016.

[49] J. Perkins. VERITAS Telescope 1 Relocation: Details and Improvements. In *AAS/High Energy Astrophysics Division #11*, volume 42 of *Bulletin of the American Astronomical Society*, page 719, Mar. 2010.

[50] J. Rajotte. Upgrade and performance of the veritas telescope array. 766:61–64, 12 2014.

[51] M. Raue and D. Mazin. Optical depth for vhe ?-rays from distant sources from a generic ebl density. *International Journal of Modern Physics*, 17(9):1515–1520, 2008.

[52] P. F. Rebillot. The veritas flash adc electronics system. *Proceedings of the 28th International Cosmic Ray Conference*, 2003.

[53] E. Roache. Mirror facets for the veritas telescopes. *Proceedings of the 29th International Cosmic Ray Conference*, 3:1397–1400, 2008.

[54] f. t. V. C. V. A. Acciari. Veritas observations of the bl lac object 1es 1218+304. *The Astrophysical Journal*, 695:1370–1375, April 2009.

[55] T. C. Weekes. Observation of TeV gamma rays from the Crab nebula using the atmospheric Cerenkov imaging technique. *Astrophysics Journal*, 342:379–395, 1989.

[56] T. C. Weekes. The Atmospheric Cerenkov imaging technique for very high energy gamma-ray astronomy. In *Lectures given at the International Heraeus Summer School: Physics with Cosmic Accelerators, Bad Honnef, Germany, July 5-16, 2004*, 2005.

[57] A. Weinstein. The veritas trigger system. *Proceedings of the 30th International Cosmic Ray Conference*, 3:1539–1542, 2008.

[58] R. Winston. Light collection within the framework of geometrical optics. *Journal of the Optical Society of America*, 60(2):245–247, 1970.

[59] Wystan Benbow for the VERITAS Collaboration. VHE Blazar Discoveries with VERITAS. *ArXiv e-prints*, Sept. 2011.

APPENDIX A. SATURATION AVOIDANCE METHOD AND THE LOW GAIN RATIO

Saturation Avoidance Method

Proof of Concept

The core distance reconstruction is shown in Chapter 4, for V5 simulations with and without the low gain switch. Figure A.1 shows the resolution on the core distance reconstruction for selected energy bins above 1 TeV.

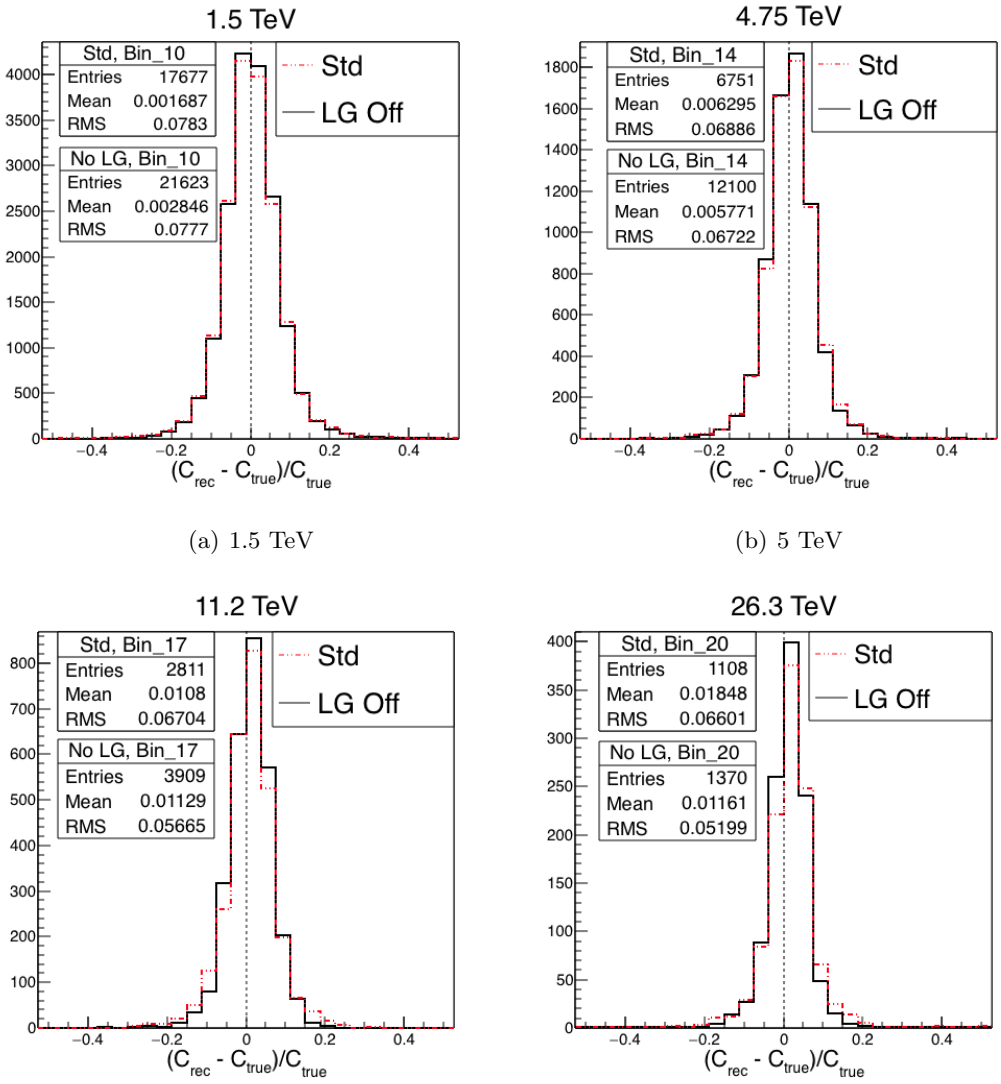

(a) 1.5 TeV

(b) 5 TeV

(c) 11 TeV

(d) 26 TeV

Figure A.1 The resolution on the reconstructed core location for select energy bins above 1 TeV. The red curve shows simulations without the low gain switch enabled, while the black curve shows the resolution for simulations with the low gain enabled.

The resolution on reconstructed core distance shows no significant effect from saturation. Even up to 30 TeV, events are reconstructed with statistically equivalent accuracy regardless of the presence of the low gain switch.

The distance cut applied in stage 4 removes images that leak off the edges of the camera. The SAM cuts are designed to avoid heavily saturated images by using only at those images obtained from telescopes far from the center of the light pool in the energy reconstruction. A larger impact distance between telescope and shower core leads to a greater likelihood of part of the image leaking off the edge of the camera. Therefore, Figure **??** shows the distance parameter for images at an impact distance greater than 150 m, compared to the distance parameter for all images participating in a reconstructed event.

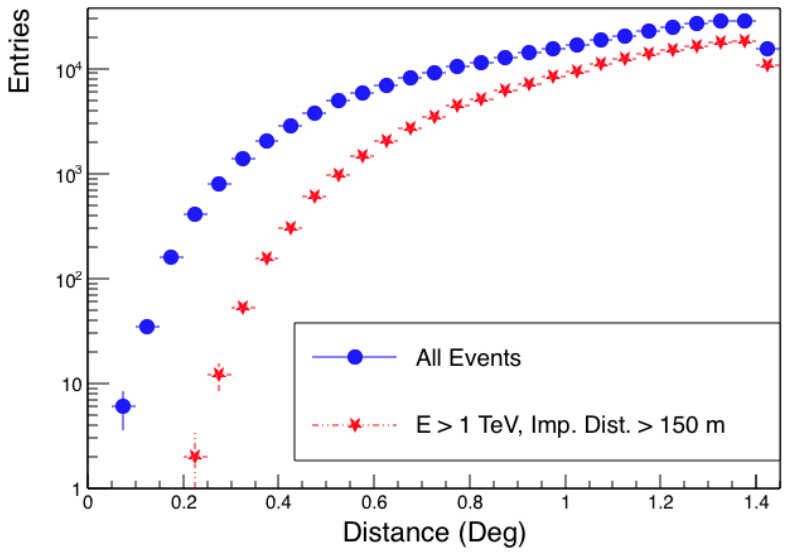

Figure A.2 Distance from camera center of simulated events in V5, plotted for telescopes with an impact distance greater than 150 m and initial energy greater than 1 TeV in the red curve, and for all images passing standard analysis cuts in the blue curve.

The more distant images peak at a higher distance value than images near the shower core, as expected. However, all images past the cut are removed from the analysis; therefore, there should not be a significant impact on images passing SAM cuts from image loss off the camera. Because this analysis is concerned with high energy events that have larger images in the camera, extending the standard distance cut to capture a higher number of events would result in a loss of light that would bias the results of the analysis.

Standard Cuts

The SAM energy reconstruction has no significant effect on standard analysis cuts, as seen in the following figures. Figure A.3 shows the SAM energy reconstruction applied in V5, while Figure A.4 shows the SAM energy reconstruction applied in V6.

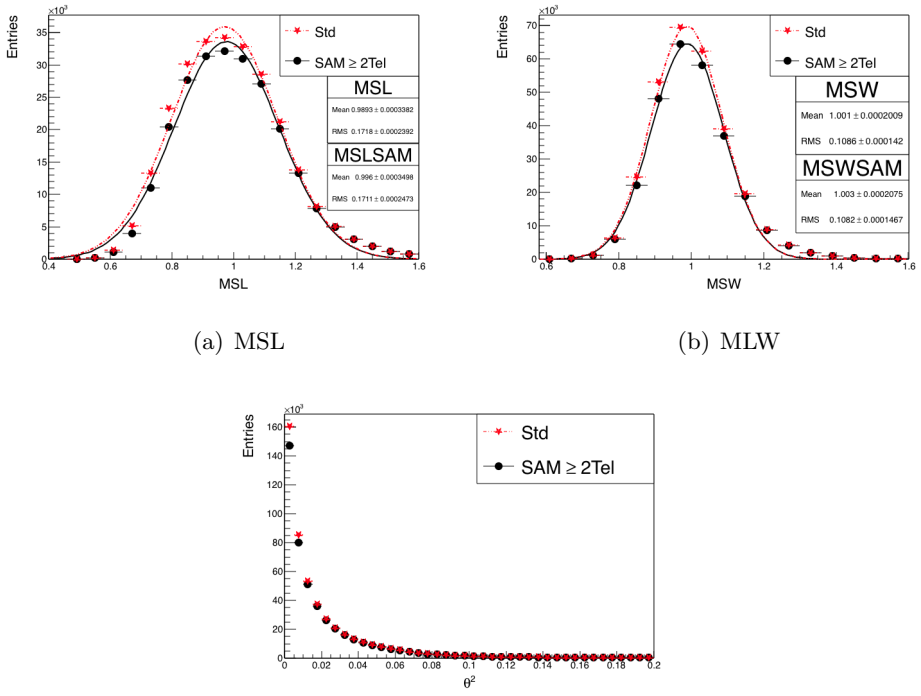

(a) MSL

(b) MLW

(c) θ^2

Figure A.3 Comparison of MSL (a), MSW (b), and θ^2 (c), for the standard analysis with medium cuts and the SAM energy reconstruction, in the V5 epoch. All simulations were run at 20 degree zenith angle.

Table A.1 shows the mean values of the mean scaled parameters and their RMS deviation.

Table A.1 MSL and MSW show no significant variation from the mean and RMS values with the SAM energy reconstruction in the V5 epoch.

	$\text{mean}_{\text{standard}}$	$\text{RMS}_{\text{standard}}$	mean_{SAM}	RMS_{SAM}
MSL	0.989	0.17	0.996	0.17
MSW	1.001	0.11	1.003	0.11

Once again, there is no significant difference in the distributions of MSPs for the standard analysis compared to the SAM analysis, in the V5 epoch.

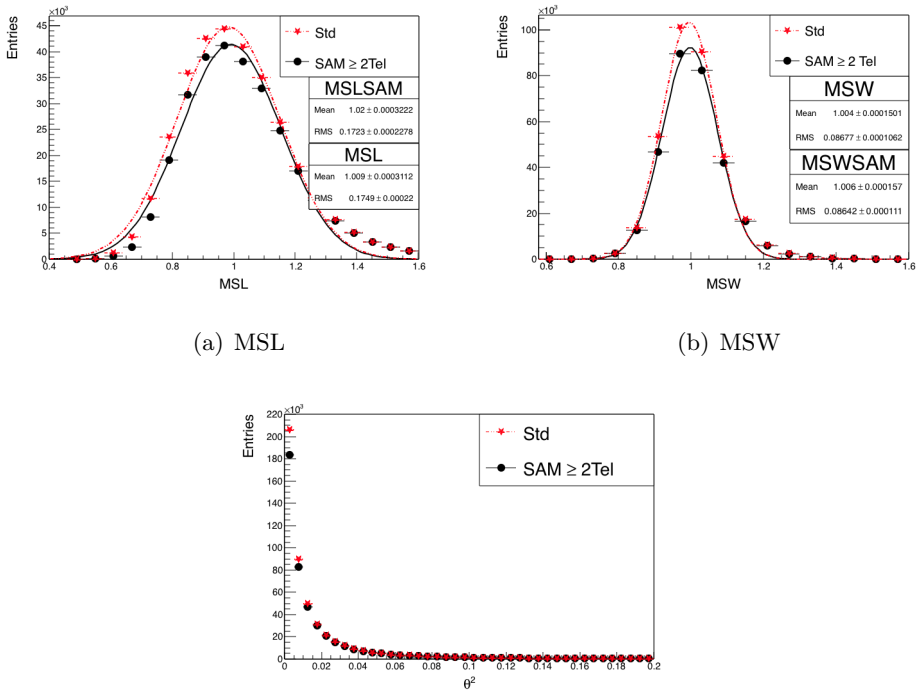

(a) MSL

(b) MSW

(c) θ^2

Figure A.4 Comparison of MSL (a), MSW (b), and θ^2 (c), for the standard analysis with medium cuts and the SAM energy reconstruction, in the V6 epoch. All simulations were run at 20 degree zenith angle.

Table A.2 shows the mean values of the mean scaled parameters and their RMS deviation.

Table A.2 MSL and MSW show no significant variation from the mean and RMS values with the SAM energy reconstruction in the V6 epoch.

	$\text{mean}_{\text{standard}}$	$\text{RMS}_{\text{standard}}$	mean_{SAM}	RMS_{SAM}
MSL	1.02	0.17	1.01	0.17
MSW	1.01	0.086	1.00	0.085

As in the V5 epoch, the V6 epoch shows no significant difference in the distributions of MSPs for the standard analysis compared to the SAM analysis.

Although standard cuts are applied as box cuts with no energy dependence, it is useful to look at the MSL and MSW parameters at energies above a few TeV, where the SAM reconstruction kicks in. Figure A.5 shows MSL, MSW, and θ^2 for events with energy greater than 3 TeV, for the V6 epoch. The MSL parameter increases at high energies for events analyzed with the SAM energy reconstruction. This is expected, as SAM selects for distant events at high energies, and length increases with impact distance. A very slight broadening of θ^2 is seen for the SAM events at high energies as well. This also follows nicely from the expectations of Figure 4.6(b).

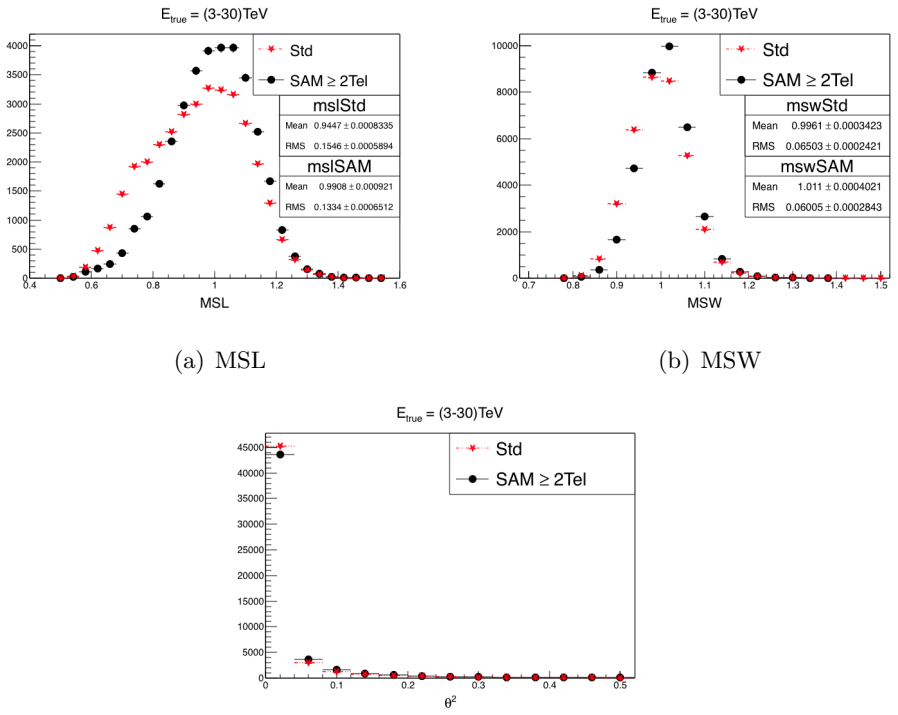

(a) MSL

(b) MSW

(c) θ^2

Figure A.5 Comparison of MSL (a), MSW (b), and θ^2 (c), for the standard analysis with medium cuts and the SAM energy reconstruction, at energies above 3 TeV. All simulations were run at 20 degree zenith angle. Plots are scaled to account for loss of statistics in SAM energy reconstruction.

The MSL parameter broadens towards the low end of the distribution for the standard analysis at high energies. This is not surprising, as more high energy showers can be detected over a wider range of impact distances, and showers with larger core distance from the array will produce longer images in the camera. Therefore, the distribution of lengths for a standard analysis at high energies is expected to be broader than at lower energies. The SAM energy reconstruction removes events that occur close to the array, however, which means the distribution of length parameters is more similar for all events. Because the values of MSL for both the standard analysis and the analysis with SAM energy reconstruction are similar at higher values of MSL, where the cut applied in stage 5 becomes relevant, no changes were made to the stage 5 cuts. The values of MSW and θ^2 were not significantly altered at high energies by the introduction of the SAM energy reconstruction.

Effect of SAM Analysis on an Artificially Saturated Spectrum

In order to test the SAM energy reconstruction on a spectrum, artificial saturation of 10% of the image size was applied to images that would be cut from energy reconstruction during the SAM analysis. Any image with a size greater than 10^4 dc at an impact distance of less than 150 m from the shower core had its size reduced by 10%. This matches the region where the majority of saturation should occur, according to Figure figSvID.

This artificial saturation was applied to a spectrum simulated with grISUdet for the V6 epoch, at 20 degrees to zenith and 0.5 degree source offset from the center of the camera. The simulated events were generated as a power law in energy with an index of -2.0.

The results of the SAM analysis on the reconstructed spectrum with artificial saturation are shown in Figure A.6. Table tabSimSAMCheck shows the fit parameters and χ^2/ndf for each reconstructed spectrum.

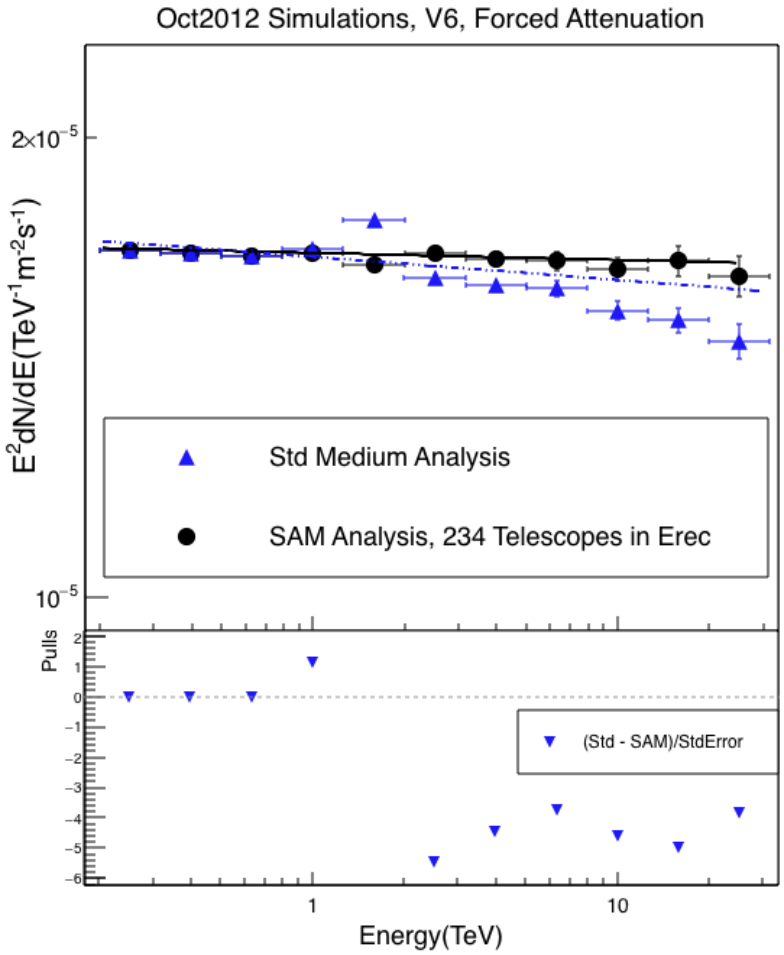

Figure A.6 V6 grISUdet simulations with 10% attenuation applied to the image size in the region cut by the SAM analysis. Spectrum in plotted in bins of reconstructed energy

Table A.3 Fit parameters for spectra obtained from simulations with artificial saturation added, compared for the standard analysis and the SAM energy reconstruction.

Analysis	Index α	Norm	χ^2/ndf
SAM	2.0045 ± 0.0023	$1.67 \cdot 10^{-5}$	4.97/8
Std	2.015 ± 0.0019	$1.67 \cdot 10^{-5}$	167/8

From this cross-check, it is clear that the SAM analysis reproduces the simulated spectrum with much greater accuracy than the standard analysis that includes all heavily saturated images. The saturated spectrum reconstructed with the standard analysis clearly curves and steepens in the TeV range, leading to a very poorly fit to a power law. The spectrum reconstructed with the SAM analysis, in comparison, is well fit by a power law with an index of -2.0045 $\pm$ 0.0023, which is well matched to the initial simulated index of -2.0.

The standard analysis, furthermore, shows a clear feature around 1–2 TeV where the low gain switch turns on. A pile-up effect occurs in the energy reconstruction for events just above the saturation threshold, which are reconstructed into the same energy bin as events just below the saturation threshold. This shows up in the bin at about 1.5 TeV that is reconstructed to a flux well above the rest of the spectrum. This feature can be used in spectra extending to multi-TeV energies to deduce the existence of significant saturation in a reconstructed spectrum.

Low Gain Ratio Data/MC Comparisons

The low gain ratio in VERITAS can be measured by comparing pixel brightness between data and MC simulations. In this section, several supplementary plots are shown to complement and reinforce the conclusions reached in Section 5.1 of Chapter 4.

A.0.1 Max1

The jump in the Max1 distribution of data above approximately 700 dc, as shown in Chapter 4, Figure 5.2, strongly indicates that the low gain ratio of 5.8 used in standard analyses of V6 data is too high, and therefore causing an upward bias in measured pixel size of low gain channels. Further studies were done to determine a more appropriate value of the low gain ratio. The V6 Crab Nebula data was analyzed with values of the low gain

ratio equaling 5.0, 5.2, 5.3, and 5.4. Below, the Max1 data/MC distributions are shown for 5.0 (Figure A.7) 5.2 (Figure A.8), 5.3 (Figure A.9), and 5.4 (Figure A.10).

VEGAS applies the low gain ratio in the first two analysis stages. Therefore, in order to run data/MC comparisons with different low gain ratios, each value tested required re-analyzing the data from the raw VBF files. Due to the size and computing time requirements of running stages 1 and 2 in VEGAS, the initial testing was performed for smaller subsets of about half the V6 Crab data, rather than the full 46 hours.

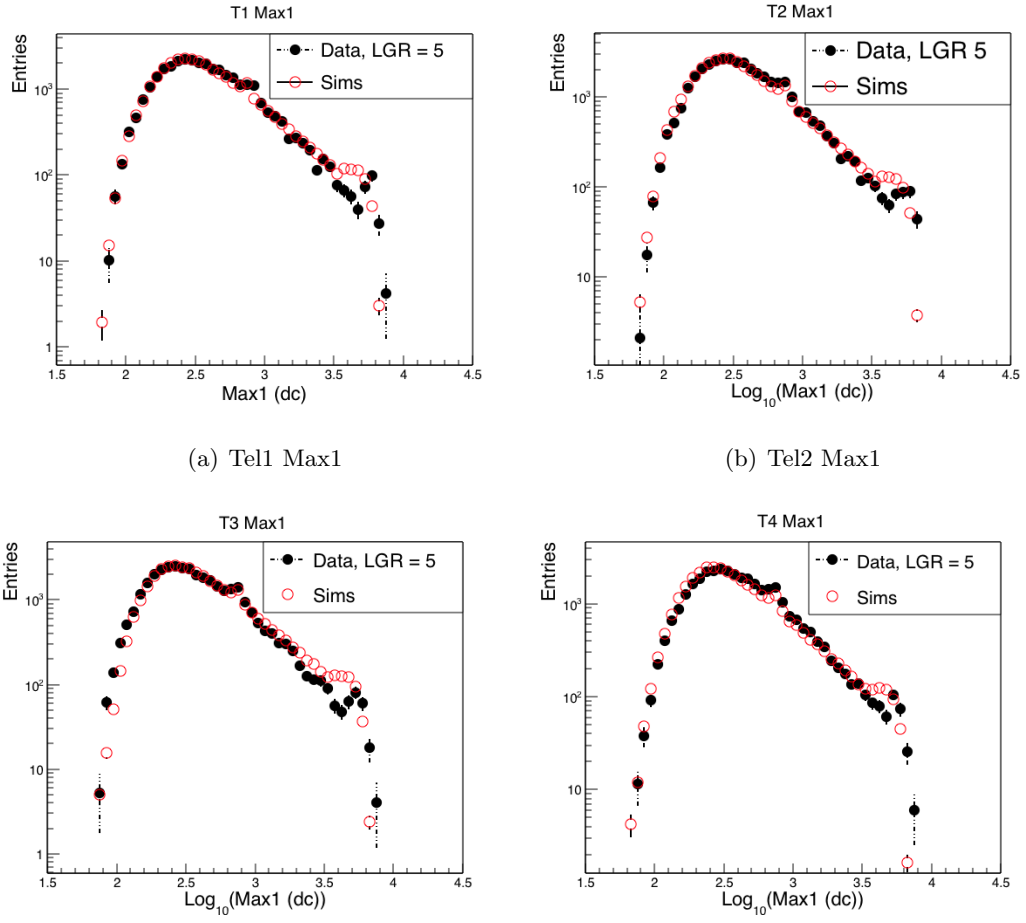

(a) Tel1 Max1

(b) Tel2 Max1

(c) Tel3 Max1

(d) Tel4 Max1

Figure A.7 Data/MC comparison of Max1 for data reconstructed with a low gain ratio of 5.0.

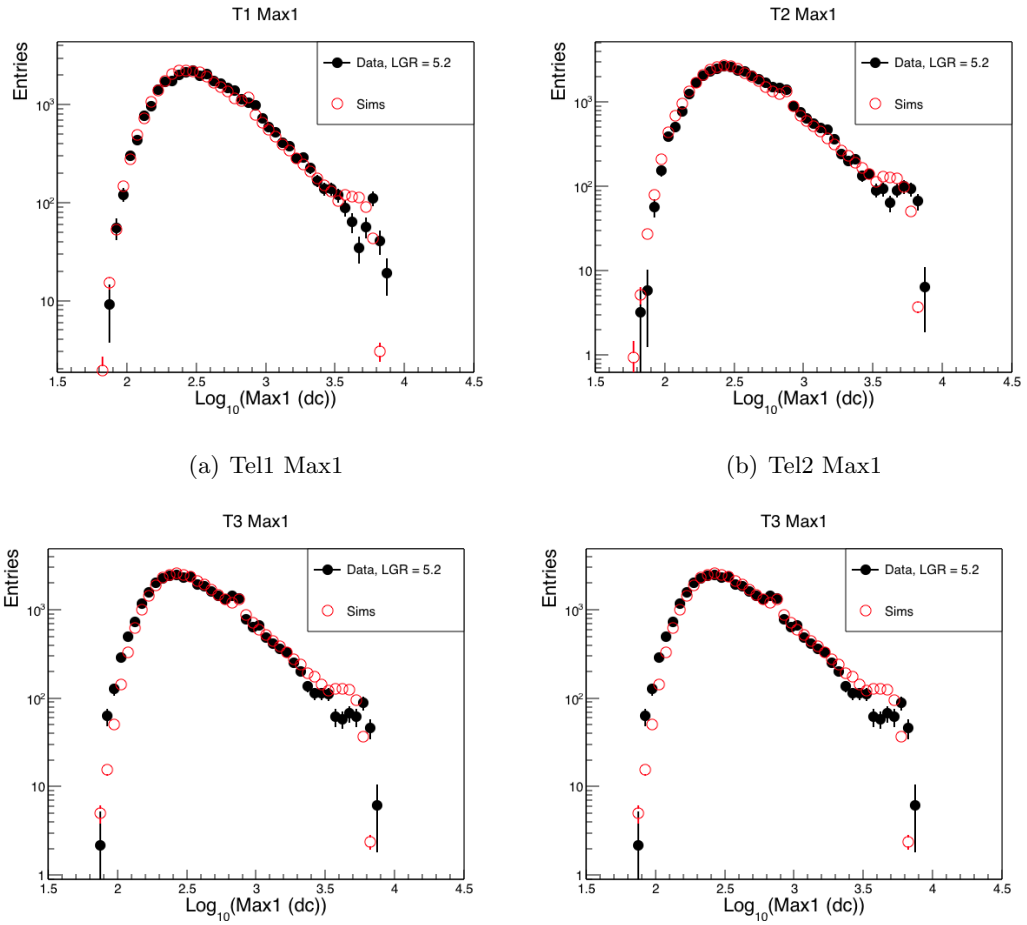

(a) Tel1 Max1

(b) Tel2 Max1

(c) Tel3 Max1

(d) Tel4 Max1

Figure A.8 Data/MC comparison of Max1 for data reconstructed with a low gain ratio of 5.2.

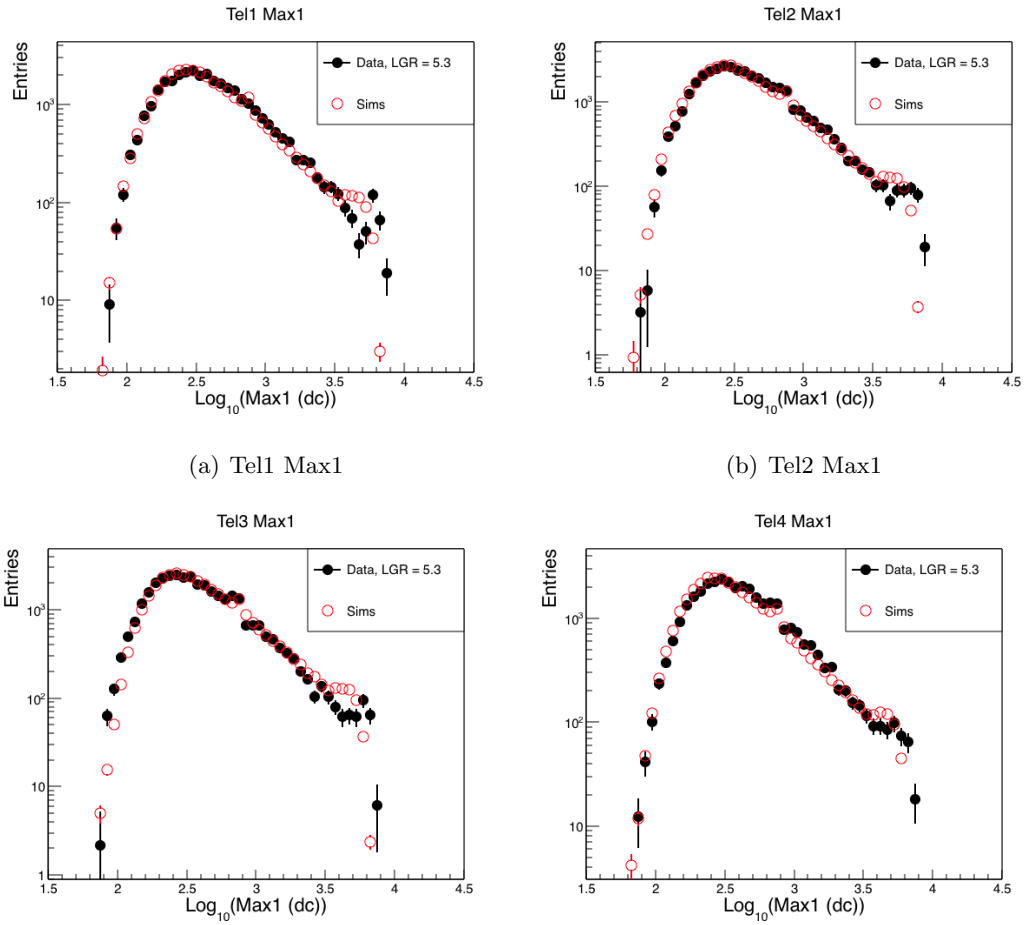

(a) Tel1 Max1

(b) Tel2 Max1

(c) Tel3 Max1

(d) Tel4 Max1

Figure A.9 Data/MC comparison of Max1 for data reconstructed with a low gain ratio of 5.3.

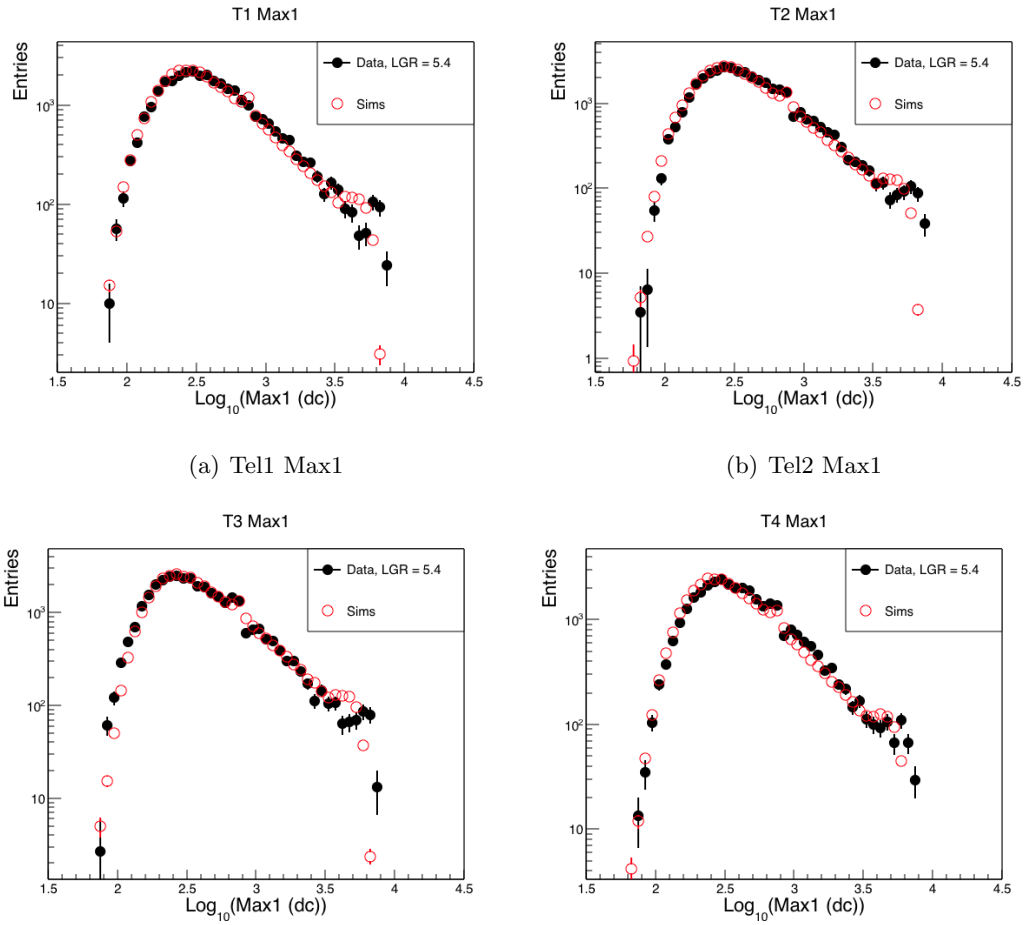

(a) Tel1 Max1

(b) Tel2 Max1

(c) Tel3 Max1

(d) Tel4 Max1

Figure A.10 Data/MC comparison of Max1 for data reconstructed with a low gain ratio of 5.4.

The Max1 distributions vary with the low gain ratio applied, though all Max1 distributions become smoother for ratios below 5.8. This provides further strong evidence that the low gain ratio is driving the hardening of the V6 Crab spectrum with the standard analysis. All telescopes except for T1 show a bump at about 700 dc arising from inefficiency in the switch between high and low gain. This bump is also apparent in the simulations. This occurs due to the fact that events right on the edge of switching may lose some light and fail to switch, causing an increased number of events at lower Max1, and a slight jump before

the distribution continues at Max1 values above the low gain switch. For low values of the low gain ratio, there is a greater pile-up of events at the transition. In addition, for extreme values of the low gain ratio, 4.5 and 7, the effect is even clearer.

Several other features can be seen in the Max1 distributions. The Max1 distributions vary between telescopes, with T3 data/MC comparisons indicating the highest low gain ratio between the four telescopes, and T4 indicating the lowest ratio. In addition, the choice of 5 for the simulated low gain ratio creates a mismatch between data and simulations at the high energy tails of the Max1 distribution. The mismatch is caused by both the higher ratio in data and by the broadening of low gain pulses in data, due to the design of the electronics Simulated low gain pulses see no broadening over high gain pulses, as they are simply scaled down models of the high gain pulse. This leads to low gain pulses in data which peak at lower dc values than simulated pulses in the FADCs, for the same reconstructed Max1 value. A lower peak in data leads to slower saturation of the low gain (see Figure 3.13), which shows up in the Max1 distribution where the tails of the simulated Max1 distribution level off due to saturation earlier than the distribution taken from data.

Because VEGAS applies the low gain ratio equally to all telescopes, a ratio that provides the best match between data and simulations, as well as the smoothest transition between high and low gain, was chosen as the optimal low gain ratio value. This ratio was used in the re-analysis of V6 Crab data provided in the final section of this chapter. On average, a low gain ratio of 5.3 creates the best data/MC match and the smoothest curves. Though there is variance between telescopes, an average ratio largely washes out that variation and allows for the most accurate reconstruction of energy from the image size.

A.0.2 Max2 and Max3

The distributions of Max2 and Max3, which measure the integrated charge of the second and third brightest image pixels, respectively, contain the same features shown in the Max1

distributions. Figure A.11 shows the data/MC comparisons for Max2 in T2, with a low gain ratio of 5.8 applied in Figure A.0.2, and 5.3 applied in Figure A.0.2.

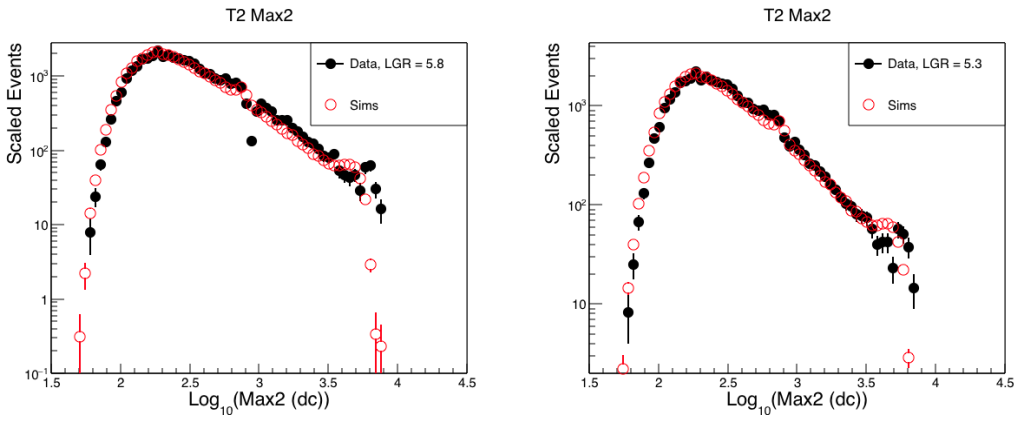

(a) Tel2 Max2, LGR = 5.8 (b) Tel2 Max2, LGR = 5.3

Figure A.11 Data/MC comparison of size for data reconstructed with a low gain ratio of 5.8 in (a), and a ratio of 5.3 in (b).

Figure A.12 shows the data/MC comparisons for Max3 in T2, with a low gain ratio of 5.8 applied in Figure A.0.2, and 5.3 applied in Figure A.0.2.

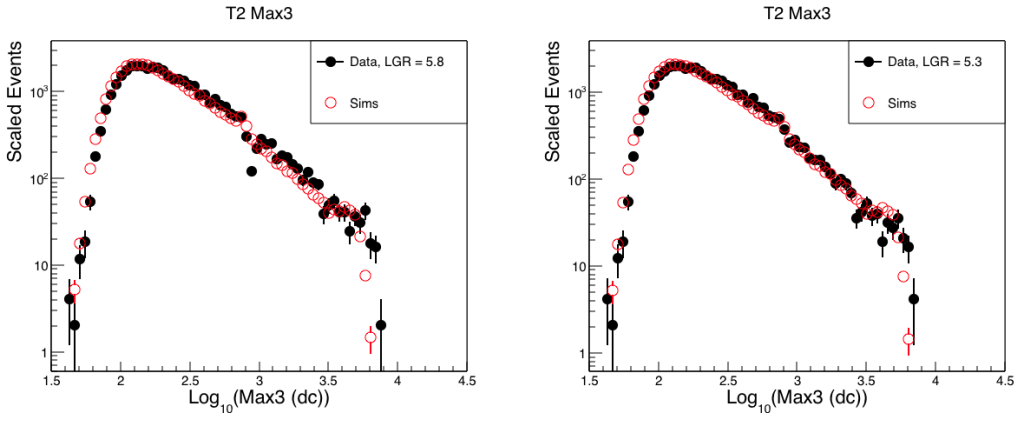

(a) Tel2 Max3, LGR = 5.8 (b) Tel2 Max3, LGR = 5.3

Figure A.12 Data/MC comparison of Max3 for data reconstructed with a low gain ratio of 5.8 in (a), and a ratio of 5.3 in (b).

APPENDIX B. SPLINE METHOD

Spline Generation

Upper limits on the EBL were calculated following the methods of works such as [51] and [7]. 480 thousand splines were generated by interpolating between randomly chosen intensities at 12 wavelengths, λ_{EBL} = 0.18, 0.32, 0.56, 1.0, 1.8, 3.2, 5.6, 10, 18, 32, 56, and 100 μm. At each λ_{EBL}, an intensity was drawn randomly in log space between 1–50 mW m^{-2} sr^{-1}. The intensities were restricted only by the condition that the intensity at subsequent values of λ_{EBL} cannot increase by more than a factor of 2.4, or decrease more steeply than a factor of 0.4, as compared to the intensity at the previous value of λ_{EBL}. This condition causes non-uniform distributions at all values of λ_{EBL} greater than 0.18. Uniformity is recovered by applying a weight to the splines during the calculation of EBL intensity probability for each value of λ_{EBL}.

The current upper and lower bounds on the EBL intensity were not considered in the initial spline generation and intensity probability calculations. Strict lower bounds arise from direct measurements of the integrated light from resolved galaxies, but it was possible in several bins for the probability distributions of intensity from the blazar measurements to extend below these strict lower bounds. Therefore, to obtain the most complete probability space, the lower bounds were applied only at the end.

For each EBL source, the observed spectrum was de-absorbed with each of the 480 thousand splines described above, and fit to new "intrinsic" spectral parameters. If the observed spectrum was best fit by a power law, only power law fits were considered for the de-absorbed spectra. If the observed spectrum was best fit by a curved spectrum, the

de-absorbed spectra were fit with a power law, a power law with exponential cutoff, and a log parabola. The EBL intensities were then weighted at each redshift by the goodness of fit of the de-absorbed spectrum. The resulting distributions of intensity at each λ_{EBL} provide the confidence regions for the EBL SED derived from analysis of VERITAS blazars.

The evolution of the EBL with redshift is discussed in Appendix C.

APPENDIX C. EXTRAGALACTIC BACKGROUND LIGHT UPPER LIMITS

Theoretical Models of the EBL

There are four main methods of constructing theoretical models of the EBL [16]. Forward evolution begins with initial cosmological models of the early universe and evolves them forward in time, using semi-analytical models of galaxy formation. Backwards evolution extrapolates current star and galaxy populations backwards in time. Both of these models are heavily dependent on theoretical cosmology. Two other methods involve more observational quantities, such as the third method of evolving galaxy counts across a range of redshifts via observable quantities such as star formation rates in the universe. The final method is "galaxy counting", determining evolution of galaxy populations via direct observations across a range of redshifts.

Both forward and backward evolution models are heavily dependent on the values of cosmological constants chosen for the model. Therefore, they are subject to the same uncertainties as the chosen models. Direct galaxy observations provide absolute lower limits to the density of the EBL. The true intensity of the EBL is expected to be higher than galaxy counting estimates, both because galaxies provide only one source of contribution to the EBL, and because only galaxies bright enough to observe can be counted, though even dimmer galaxies will contribute some amount to total EBL intensity. Galaxy counting also fails to take into account any diffuse EBL background. Figure C.1 shows several models derived from theoretical cosmological principles and from direct measurements of galaxy luminosity.

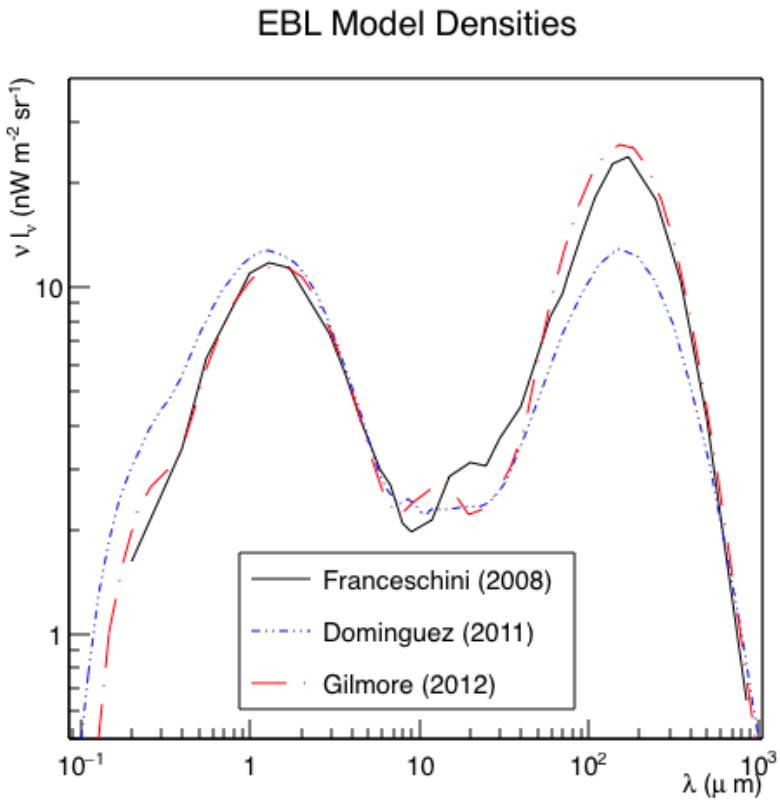

Figure C.1 EBL SEDs for three theoretical models. The earlier two models use direct galaxy observations, while the blue curve from Gilmore (2012) uses forward evolution to obtain the SED shown in the figure. There are also features of note around 10–20 μm, arising from contributions from PAHs.

Some models include a small peak around 11.2 μm for polycyclic aromatic hydrocarbons (PAH). PAHs are complex, multi-ring organic molecules assumed to form in the outflow of massive AGB stars. These molecules make up a substantial portion of the mid-IR EBL density. They absorb the UV light of their massive stellar originators, and re-emit photons down in the mid-IR. The composition and density of PAHs is not known to high accuracy. Therefore, different models include different levels of contribution.

The EBL SED is typically given in terms of νI_ν, with units $\frac{nW}{m^2 sr}$. The relation between spectral energy ϵ and number density of photons at a given redshift, $n_\epsilon(\epsilon, z)$, is given by Equation C.1.

$$\epsilon^2 n_\epsilon(\epsilon, z) = \left(\frac{4\pi}{c}\right)\nu I_\nu \tag{C.1}$$

The photon energies must be transformed to account for redshifting due to cosmological expansion, where $\epsilon' = (1+z)\epsilon$. Equation C.2 gives the relation between $n_\epsilon(\epsilon', z)$ and $n_\epsilon(\epsilon, 0)$, with number of photons is conserved across redshifts.

$$n_\epsilon(\epsilon', z)\mathrm{d}\epsilon' = (1+z)^3 n_\epsilon(\epsilon, 0)\mathrm{d}\epsilon \tag{C.2}$$

It is then simple to convert Equation C.2 into a differential energy density, as in Equation C.3

$$n_\epsilon(\epsilon', z)\mathrm{d}\epsilon' = (1+z)^4\left(\frac{4\pi}{c}\right)\left(\frac{\nu I_\nu(\nu, 0)}{\epsilon'^2}\right)\mathrm{d}\epsilon' \tag{C.3}$$

Direct measurement of the EBL density from earth is made extremely difficult to high zodical foreground emission. Therefore, indirect measurements and theoretical models are important to accurately reconstructing cosmological history.

Gamma-ray Absorption by the EBL

In order to determine the distance of the blazar, a relationship between distance and redshift is invoked following cosmological principles in Equation C.4, for a flat ΛCDM cosmology.

$$\frac{\mathrm{d}l}{\mathrm{d}z} = \frac{c}{(1+z)H_0}\frac{1}{\sqrt{\left[(1+z)^2(\Omega_m z + 1) + z(2+z)\right]\left[(1+z)\Omega_r - \Omega_\Lambda\right]}} \tag{C.4}$$

Ω_r, Ω_m, and Ω_Λ are the relative density of radiation, matter, and the cosmological constant respectively, such that $\Omega_r + \Omega_m + \Omega_\Lambda = 1$. H_0 refers to the current value of the

Hubble parameter. Integrating Equation C.4 between $z = 0$ to z gives the total distance between earth and a source at z. This is done analytically. A flat ΛCDM cosmology is assumed, with $H_0 = 70$ km s^{-1}Mpc^{-1}, $\Omega_m = 0.27$, $\Omega_\Lambda = 0.73$, and $\Omega_r = 0$. Setting $\Omega_r = 0$ allows Equation C.4 to be simplified into Equation C.5.

$$\frac{\mathrm{d}l}{\mathrm{d}z} = \frac{c}{(1+z)H_0} \frac{1}{\sqrt{\Omega_\Lambda + \Omega_m(1+z)^3}} \tag{C.5}$$

The $\gamma\gamma$ cross section for pair production was first described by Briet and Wheeler in 1934 [10]. Gould and Schroder also described the process of $\gamma\gamma$ pair production and absorption probabilities for VHE gamma rays in [29]; this cross-section is reproduced here in Equation C.6.

$$\sigma_{\gamma\gamma}(E_\gamma, \epsilon, \mu) = \frac{3}{16}\sigma_T^2(1-\beta^2)\left[2\beta(\beta^2-2) + (3-\beta^4)\ln\frac{1+\beta}{1-\beta}\right] \tag{C.6}$$

where σ_T is the Thomson cross-section, and β is given by Equation C.7.

$$\beta^2 = 1 - \frac{2m_e^2c^4}{E_0\epsilon}\frac{1}{1+z}\frac{1}{1-\mu} \tag{C.7}$$

Here, ϵ denotes the energy of the EBL photons at redshift z. From Equation C.7, it can be seen that $\beta^2 \geq 0$ is equivalent to the pair production threshold. The EBL is transparent to gamma rays with energy, E_0 such that $\beta^2 < 0$.

EBL Evolution

Values of $f_{\mathrm{evo}}$are compared to three theoretical EBL models to approximate the systematic bias on the upper limits to the EBL density. The values chosen in this study are f_{evo}=1.2, 1.7 and 2.2, following the method of [7].

The theoretical models chosen come from Dominguez (2011), Franceschini (2008), and Gilmore (2012). These models were derived as follows:

- **Dominguez:** Direct galaxy observations from Extended Groth Strip International Survey (AEGIS). Multiwavelength data from about 6000 galaxies covering a redshift range of $z = 0.2 - -1$ provides the lower limits on the EBL.
- **Franceschini:** A mixture of direct multiwavelength measurements, upper limits from COBE, and backwards evolution from cosmological models went into the Franceschini EBL density model.
- **Gilmore:** Provides EBL intensity based forward evolution from semi-analytic models (SAMs), using Λ cold dark matter models of cosmology to trace structure formation in the early universe.

The three values of $F_{\rm evo}$ were used to calculate τ from Equation 7.2. Figure C.2 shows the opacity vs. energy in TeV for each value of $F_{\rm evo}$ compared to each of the three models discussed above, for $z = 0.2$.

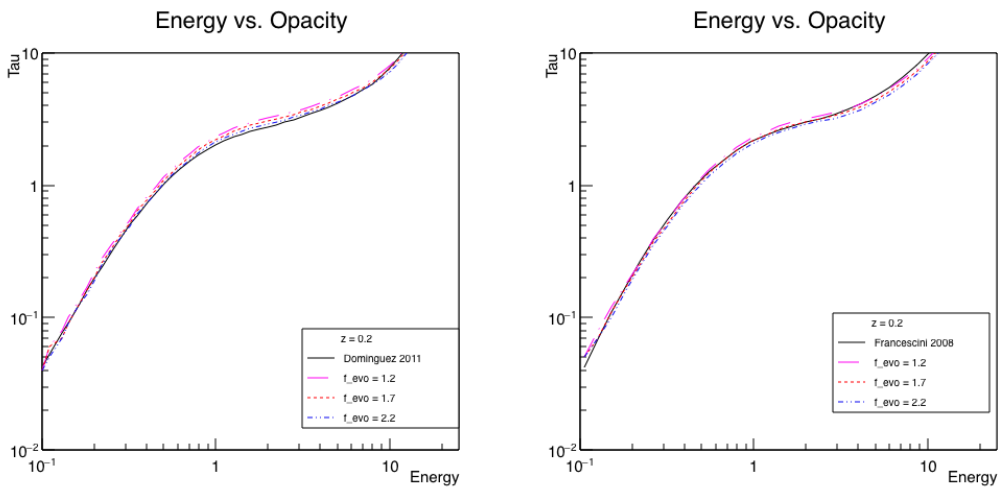

(a) Dominguez (2011)

(b) Franceschini (2008)

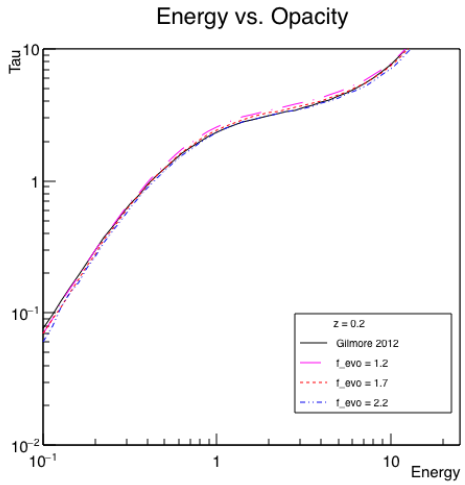

(c) Gilmore (2012)

Figure C.2 Gamma-ray opacity for 3 different values of $F_{\rm evo}$ compared to 3 different models, for $z = 0.2$.

Figure C.3 shows the fractional difference in opacity at varying redshifts, compared to Gilmore (2012), for each of the three evolutionary values.

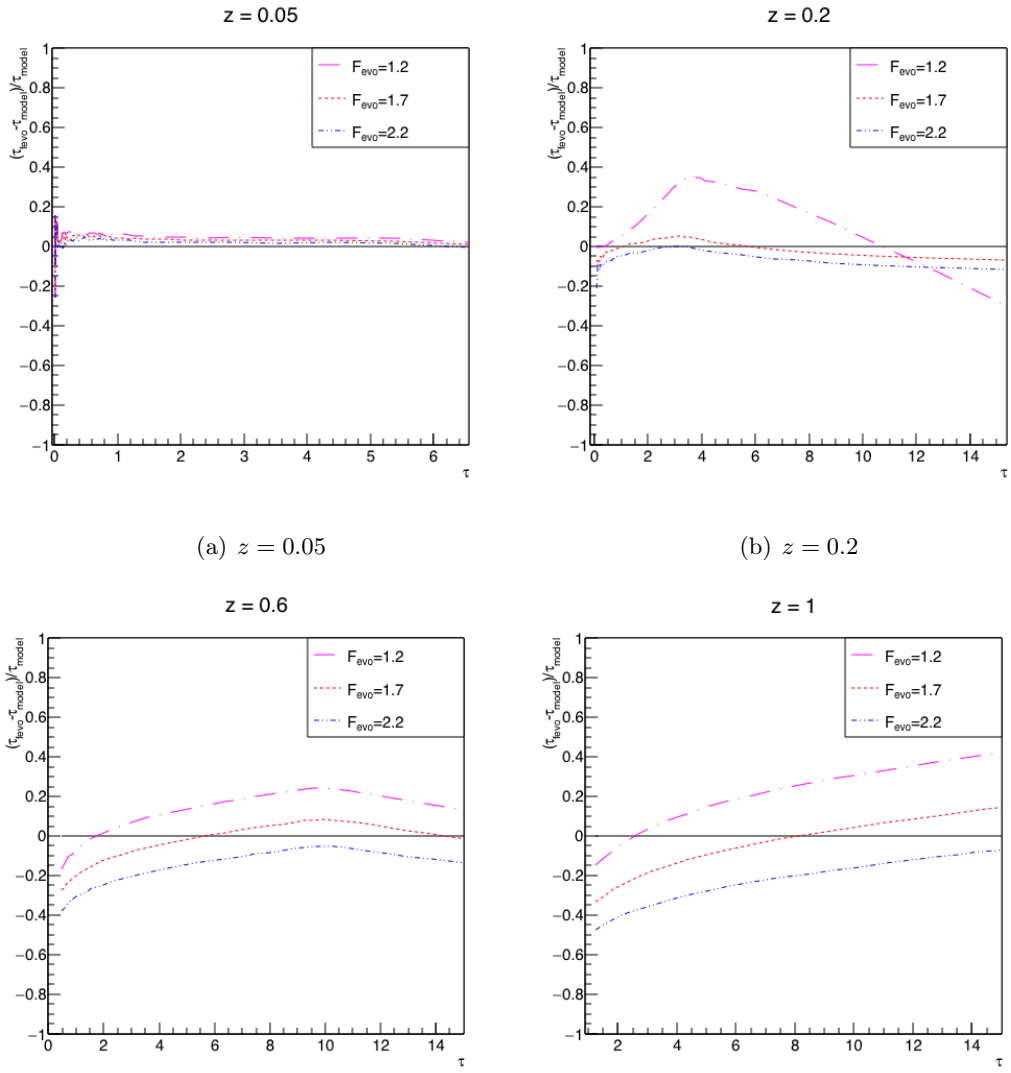

(a) $z = 0.05$

(b) $z = 0.2$

(c) $z = 0.6$

(d) $z = 1.0$

Figure C.3 $\Delta\tau/\tau$ vs. τ at several redshift values, as compared to values from Gilmore (2012) at $z = 0$.

Finally, each of the three test values of $F_{\rm evo}$ was used to de-absorb a power law spectrum absorbed with the EBL model of Gilmore, 2012. The test spectrum was placed at redshifts of 0.05, 0.2, and 0.6 for both absorption and de-absorption. The results are shown in Figure C.4.

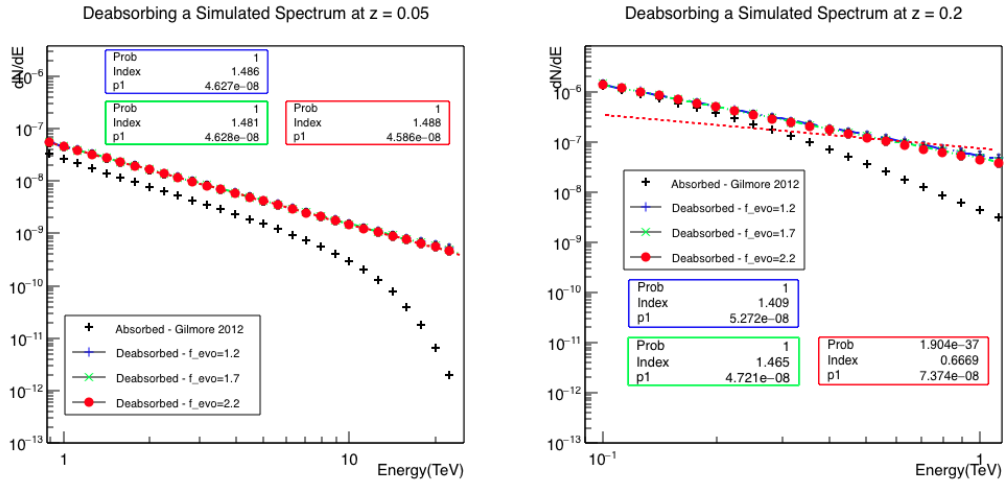

(a) $z = 0.05$ (b) $z = 0.2$

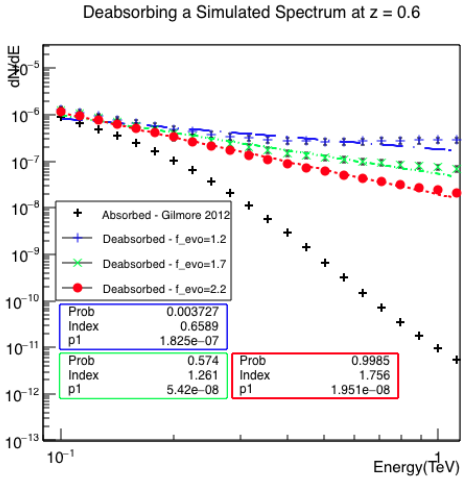

(c) $z = 0.6$

Figure C.4 Comparison of opacities at four redshift values for the models used in this work.

For this work, an evolutionary factor of 1.7 was chosen as the ideal factor out to $z = 1$, though there are indications that a larger evolutionary factor is more appropriate for the highest redshift sources beyond about $z = 0.6$. The differences that arise due to the choice of f_{evo}value for a given model is less than the differences between opacities in different EBL

models, as shown in Figure C.5. The uncertainty in the value of $f_{\text{evo}}$is also well within the range of other sources of statistical and systematic uncertainties.

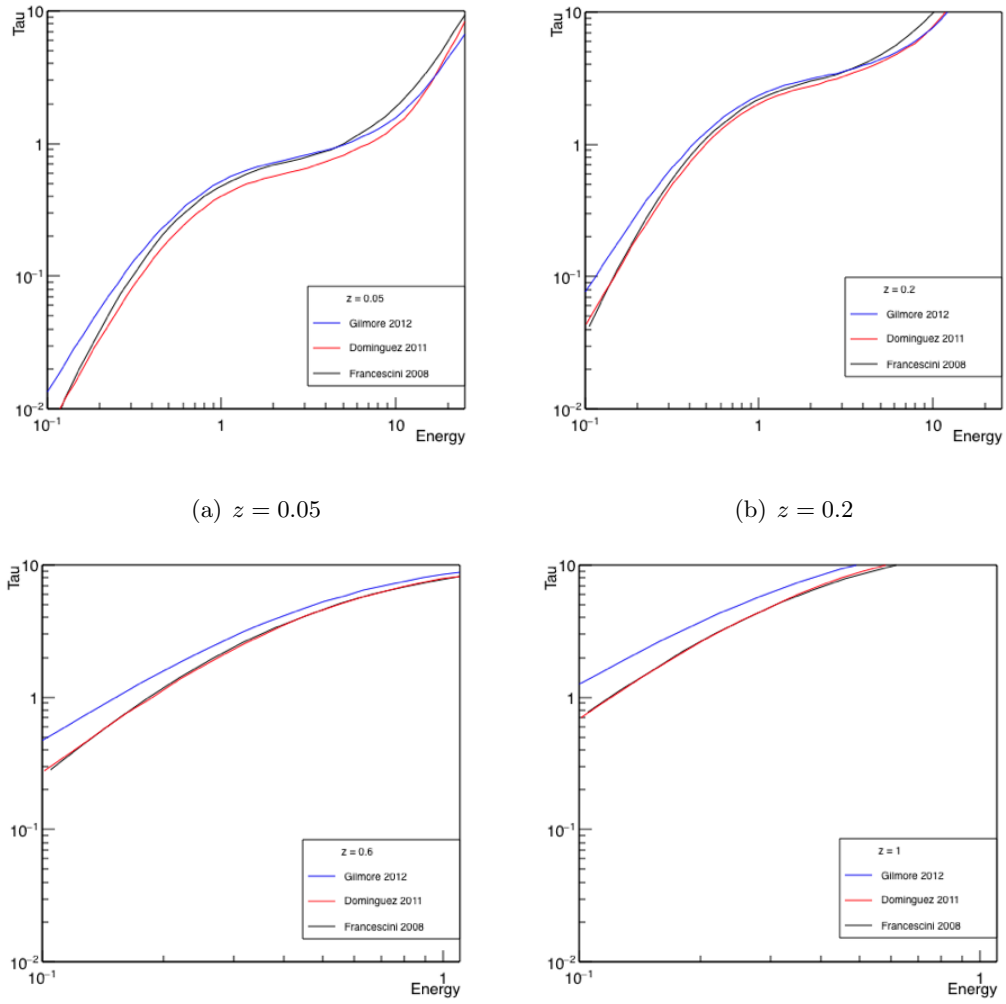

(a) $z = 0.05$ (b) $z = 0.2$

(c) $z = 0.6$ (d) $z = 1$

Figure C.5 Comparison of opacities at four redshift values for the models used in this work.

The models of Dominguez and Franceschini both consider direct measurements of integrated galaxy light to construct their EBL intensities. Therefore, both models achieve slightly lower opacity than the model of Gilmore in the second peak, as the model used from Gilmore constructs EBL density from forward evolution models that could include

additional dim and diffuse components. In the IR to optical range, Dominguez observes a higher intensity of EBL photons than the other two models. However, in this region zodiacal light is difficult to remove from direct observations. Therefore, a model reliant solely on direct observations has large error bars in this region.

Figure C.5 provides an estimate of the difference in opacity arising from different models, which is greater than the difference in opacity arising from different values of $f_{\rm evo}$ at low redshift values, and comparable to the differences from choice of $f_{\rm evo}$ at high redshift values.